

# Robust Bone Detection in Ultrasound Using Combined Strain Imaging and Envelope Signal Power Detection

by

Mohammad Arafat Hussain

B.Sc., Bangladesh University of Engineering and Technology, 2011

M.Sc., Bangladesh University of Engineering and Technology, 2013

A THESIS SUBMITTED IN PARTIAL FULFILLMENT OF  
THE REQUIREMENT FOR THE DEGREE OF

MASTER OF APPLIED SCIENCE

in

THE FACULTY OF GRADUATE AND POSTDOCTORAL STUDIES

(Biomedical Engineering)

THE UNIVERSITY OF BRITISH COLUMBIA

(Vancouver)

June 2015

© Mohammad Arafat Hussain, 2015

# Abstract

Using ultrasound for tool navigation in an orthopaedic surgery requires bone localization in ultrasound, a procedure which remains challenging despite encouraging advances in its practice. Current methods, e.g., the local image phase-based feature analysis, have shown promising results but continue to rely on delicate parameter selection processes and to be prone to error at confounding soft tissue interfaces of similar appearance to bone interfaces. In addition, the 3-dimensional phase-features-based automatic bone segmentation method is found to be time inefficient (at  $\sim 2$  minutes).

We have proposed a different approach to bone segmentation by combining ultrasound strain imaging and envelope power detection methods. After an estimation of the strain and envelope power maps, we subsequently fused these maps into a single combined map that corresponds robustly to the actual bone boundaries. This study has achieved a marked reduction in false positive bone responses at the soft tissue interfaces. We also incorporated the depth-dependent cumulative power of the envelope into the elastographic data as well as incorporated an echo de-correlation measurement-based weight to fuse the strain and envelope map. We also employed a data driven scheme to detect the presence of any bone discontinuity in the scanned ultrasound image and introduced a multi-variate non-parametric Gaussian mixture regression to be used over the maximum intensity points of the fused map. Finally, we developed a simple yet effective means to perform 3-dimensional bone surface extractions using a surface growing approach that is seeded from the 2-dimensional bone contours.

We employed mean absolute error calculations between the actual and estimated bone boundaries to show the extent of the false positives created; our methods showed an average improvement in the mean absolute error of 20% on both the 2- and 3-dimensional finite-element-models, and of 18% and 23%, respectively, on the 2- and 3-dimensional experimental phantom data, when compared with that of the local phase-based methods. Validation on the 2- and 3-dimensional clinical *in vivo* data also demonstrates, respectively, an average improvement in the mean absolute fitting error of 55% and an 18 times improvement in the computation time.

# Preface

## Contributions:

This research was conducted under the supervision of my Principal-supervisor Prof. Rafeef Abugharbieh, PhD and Co-supervisor Prof. Antony J. Hodgson, PhD in UBC's Biomedical Signal and Image Computing Laboratory (Director: Prof. Rafeef Abugharbieh, PhD). My role included developing the research question, hypotheses and methodological design, completing the ethics application, conducting the literature review, preparing the experimental setups, organizing technology requirements, recruiting participants, collecting and analyzing the data, and drafting this written document.

## Publications:

A version of the chapter 2 has been published. *Hussain, M.A., Hodgson, A.J., and Abugharbieh, R. "Robust Bone Detection in Ultrasound Using Combined Strain Imaging and Envelope Signal Power Detection", Medical Image Computing and Computer-Assisted Intervention (MICCAI), Cambridge-USA, September, Pages: 356–363, 2014.* I conducted all the testing and wrote the manuscript. My supervisors provided the valuable suggestions on the methodology, and reviewed and corrected the manuscript.

Some part of the chapter 3 has been accepted for publication. *Hussain, M.A., Pierre, G., Hodgson, A.J., and Abugharbieh, R. "Automatic Bone Segmentation in Ultrasound using Combined Ultrasound Strain Imaging and Envelope Signal Power", The 2015 Computer Assisted Orthopedic Surgery (CAOS) Annual Meeting, Vancouver, Canada, June 17–20, 2015.* I conducted all the testing and wrote the manuscript. My supervisors provided the valuable suggestions on the methodology, and reviewed and corrected the manuscript.

Finally, a combination of the chapters 4 and 5 will be submitted as a full journal article which is now under preparation.

**Ethics:**

This research study met the criteria for a *Minimal Risks Human Ethics* application, and thus an expedited review by the UBC Clinical Research Ethics Board (CREB) was conducted. UBC CREB number is H15-00154.

**Conflict of Interest:**

The researchers and members of the thesis committee report no conflict of interest.



# Table of Contents

<b>Abstract</b> . . . . .	<b>ii</b>
<b>Preface</b> . . . . .	<b>iii</b>
<b>Table of Contents</b> . . . . .	<b>v</b>
<b>List of Tables</b> . . . . .	<b>ix</b>
<b>List of Figures</b> . . . . .	<b>x</b>
<b>List of Abbreviations</b> . . . . .	<b>xx</b>
<b>Acknowledgements</b> . . . . .	<b>xxi</b>
<b>Dedication</b> . . . . .	<b>xxii</b>
<b>1 Introduction and Background</b> . . . . .	<b>1</b>
1.1 Motivation and Problem Statement . . . . .	1
1.2 Medical Imaging in Orthopedic Surgery . . . . .	3
1.2.1 Pre-operative Imaging . . . . .	4
1.2.2 Intra-operative Imaging . . . . .	9
1.3 The Basic Physics of Ultrasound Imaging . . . . .	11
1.3.1 Sound Properties . . . . .	12
1.3.2 The Generation and Reception of Ultrasound Pulses . . . . .	13
1.3.3 Ultrasound-tissue Interaction . . . . .	18
1.3.4 Ultrasound Beamforming . . . . .	20
1.3.5 Ultrasound B-mode Image Formation . . . . .	21
1.4 Challenges in Ultrasound Image Interpretation . . . . .	23

1.4.1	Speckle Noise . . . . .	24
1.4.2	Reverberation . . . . .	24
1.4.3	Attenuation/Shadowing . . . . .	26
1.4.4	Mirror Images . . . . .	26
1.4.5	Anisotropy . . . . .	26
1.5	Ultrasound-based CAOS Systems . . . . .	26
1.6	Current Ultrasound-based Bone Segmentation Methods . . . . .	29
1.6.1	B-mode Imaging-based Methods . . . . .	29
1.6.2	Strain-imaging-based Methods . . . . .	35
1.7	Thesis Objectives . . . . .	37
1.8	Thesis Organization . . . . .	37
<b>2</b>	<b>Bone Detection in Ultrasound Using Combined Strain-imaging and Envelope Power . . . . .</b>	<b>40</b>
2.1	Ultrasound Signal Model . . . . .	40
2.2	Modified Strain Map (MSM) . . . . .	41
2.2.1	Displacement Estimation . . . . .	41
2.2.2	Strain Estimation and Processing . . . . .	43
2.3	Modified Envelope Map (MEM) . . . . .	43
2.4	Fused Map Estimation . . . . .	44
2.5	Forming Bone Contour Using Regression . . . . .	45
2.6	Validation Setup . . . . .	45
2.6.1	Simulated Phantom . . . . .	45
2.6.2	Experimental Physical Phantom . . . . .	46
2.6.3	<i>In Vivo</i> Data . . . . .	47
2.7	Results . . . . .	47
2.7.1	FEM Results . . . . .	48
2.7.2	Experimental Phantom Results . . . . .	49
2.7.3	<i>In Vivo</i> Results . . . . .	51
2.8	Advantages and Limitations . . . . .	56
<b>3</b>	<b>Improved 2D Bone Contour Extraction Using Data-driven Parameters . . . . .</b>	<b>59</b>

3.1	Improved Modified Envelope Map (MEM) and Modified Strain Map (MSM) Estimation . . . . .	60
3.2	Data-driven Weight Estimation . . . . .	61
3.3	Bone Discontinuity Detection . . . . .	63
3.4	Gaussian Mixture Regression (GMR) . . . . .	64
3.5	Validation Setup . . . . .	66
3.5.1	Simulated Phantom . . . . .	66
3.5.2	Experimental Phantom . . . . .	67
3.5.3	<i>In Vivo</i> Data . . . . .	68
3.6	Results . . . . .	68
3.6.1	FEM Results . . . . .	69
3.6.2	Experimental Phantom Results . . . . .	71
3.6.3	<i>In Vivo</i> Results . . . . .	72
3.6.4	Quantitative Comparison . . . . .	79
3.7	Advantages and Limitations . . . . .	83
<b>4</b>	<b>Strain-initialized Bone Surface Detection in 3D Ultrasound . .</b>	<b>85</b>
4.1	Ultrasound Scanning Protocol . . . . .	85
4.2	3D Bone Surface Extraction Using Surface-growing . . . . .	86
4.3	Validation Setup . . . . .	87
4.3.1	Simulated Phantom . . . . .	87
4.3.2	Experimental Phantom . . . . .	88
4.3.3	<i>In Vivo</i> Data . . . . .	88
4.4	Results . . . . .	88
4.4.1	FEM Results . . . . .	90
4.4.2	Experimental Phantom Results . . . . .	90
4.4.3	<i>In Vivo</i> Results . . . . .	90
4.4.4	Quantitative Validation . . . . .	94
4.5	Advantages and Limitations . . . . .	96
<b>5</b>	<b>Conclusions . . . . .</b>	<b>97</b>
5.1	The Impact and Potential Clinical Application . . . . .	97
5.2	Thesis Contributions . . . . .	98
5.3	Remaining Challenges and Future Work . . . . .	99

Bibliography . . . . .	101
Appendix A Clinical Evaluation Protocol Form . . . . .	112
Appendix B Clinical Evaluation Patient Consent Form . . . . .	120

# List of Tables

1.1	Acoustic impedances of different body tissues and organs [1]. . . .	18
3.1	Mean absolute error (MAE) Analysis of the individual effects of using the depth-dependent cumulative power (at $\rho_{avg} \approx 0.90$ ), data-driven weight (at $\rho_{avg} \approx 0.75$ and $0.60$ ), and GMR on the <i>in vivo</i> data. . . . .	80
3.2	Mean absolute fitting error (mm) comparisons of the 2DSE and 2DOPS methods using the <i>in vivo</i> data. . . . .	80
3.3	F-Test for the variances in Fig. 3.14. . . . .	81
4.1	Computation time in second for a volume size of $364 \times 110 \times 50$ voxels.	95

# List of Figures

1.1	A bird eye view of the ultrasound guided surgical tool navigation system in a CAOS procedure. Major system parts are shown as super-blocks with numbered-dotted-boxes. . . . .	3
1.2	X-rays are part of the electromagnetic spectrum, with wavelengths shorter than visible light. Different applications use different parts of the X-ray spectrum [2]. . . . .	5
1.3	(a) An X-ray CT scanner [3], (b) an X-ray CT scanner with cover removed to show internal components. Legend- T: X-ray tube, D: X-ray detectors, X: X-ray beam, and R: Gantry rotation [4]. (c) A schematic image of a CT scanner with X-ray source and detectors shown in three position [5]. . . . .	6
1.4	A schematic diagram of multi-slice helical CT acquisition process [6].	7
1.5	(a) An illustration of a real MRI scanner [7], and (b) a cutaway schematic image of an MRI scanner [8]. . . . .	8
1.6	(a) A typical fluoroscopic image of the human pelvic region [9], (b) fluoroscopic burn from long exposure [10], and (c) a diagram showing the components of a fluoroscopic imaging chain [11]. . . .	9
1.7	(a) A modern medical ultrasound scanner [12], (b) a modern portable ultrasound scanner [13], and (c) a schematic diagram of the parts of an ultrasound scanner. . . . .	11
1.8	Sound frequency ranges for infrasound, audible (sound) and ultrasound waves and the corresponding mammals that can hear them [14]. . . . .	12
1.9	A comparison of the resolution and penetration of different ultrasound transducer frequencies [15]. . . . .	13

1.10	The (a) direct and (b) converse piezoelectric effect. Mechanical deformation and consequent oscillation caused by an electrical field applied to certain material can produce a sound of high frequency [16]. . . . .	14
1.11	(a) Different components of a convex type ultrasound probe, and (b) a graphical representation of the pulse transmission and reception of a piezoelectric crystal [17]. . . . .	15
1.12	Illustration of the (a) function of the backing material, (b) function of the acoustic matching layer, and (c) function of the acoustic lens [17]. . . . .	16
1.13	Electronic steering and focusing of ultrasound beam [18]. . . . .	17
1.14	Schematic representation of ultrasound pulse generation [19]. . . . .	17
1.15	Different types of ultrasound wave-tissue interactions [1]. . . . .	19
1.16	Reflection and refraction of the ultrasound beams [20]. . . . .	19
1.17	Ultrasound image acquisition process [21]. . . . .	21
1.18	Block diagram showing the B-mode image formation and pre-display processing. . . . .	21
1.19	Schematic image showing different tissue layers in a bony anatomy [22]. . . . .	24
1.20	(a) The reverberation artifact in a human ilium scan [23], (b) the shadowing artifact in a human shoulder scan [24], and (c) the Mirror image artefact. Persistent haematoma lesion anterior to the tibia also appears deep to the surface of the tibia [25]. . . . .	25

1.21	Illustration of the anisotropy artifacts in the ultrasound bone scanning. (a) A schematic diagram showing the causes of the anisotropy artifact. If the bone surface is parallel to the transducer face, then most of the echo power reflects back to the transducer (blue dotted-arrows), if the bone surface is partially ( $< 45^0$ ) inclined to the transducer face, then a partial echo power reflects back to the transducer (green dotted-arrows), and if the bone surface is almost perpendicular ( $> 45^0$ ) to the transducer face, then almost no echo power reflects back to the transducer (red dotted-arrows). (b) and (c) show two clinical example images [26] showing anisotropy artifacts. Blue, green and red arrows correspond to regions that reflects full, partial and almost no echo power from the bone surface to the transducer, respectively. . . . .	25
1.22	(a) Intra-operative 2D C-arm fluoroscopy, (b) 2D fluoroscopy scan showing the fractured distal radius and inserted K-wire, (c) 2D fluoroscopy scan showing the fractured distal radius and metal T-plate used during the surgery. The images are taken during a distal radius surgery at the Vancouver General Hospital (VGH), Vancouver, BC, Canada . . . . .	27
1.23	Typical isodose curves (in $\mu\text{Gy}/\text{min}$ ) for a mobile C-arm fluoroscopy system [27]. . . . .	28
1.24	Illustration of the 2D bone segmentation performance of the reflected power imaging-based method developed by Xu et al. [28] using the bone phantom and <i>in vivo</i> data. (a)-(d) are the B-mode images, and (e)-(h) are the reflected power images. . . . .	31
1.25	Illustration of the presence of false positives as well as the false bone discontinuity in the estimated phase symmetry images using the <i>in vivo</i> data. (a)-(d) are the B-mode images with expert delineated bone boundaries overlaid. (e)-(h) are the phase symmetry images correspond to images shown in (a)-(d), respectively. The false positive intensities are shown with yellow arrows while false bone discontinuities are shown with white arrows. . . . .	34



1.26	Illustration of the 2D bone segmentation performance of methods developed by Xu et al. [28] using the bone phantom and <i>in vivo</i> data. (a)-(d) are the B-mode images, and (e)-(h) are the strain images. . . . .	36
2.1	Illustration of the experimental phantom. (a) The phantom was created using a Sawbones radio-opaque hemi-pelvis, cut along red line. (b) The separated portion (shown with red arrow in (a)) of the pelvis is embedded in polyvinyl chloride (PVC) gel. . . . .	46
2.2	Illustration of bone boundary detection using the FEM phantom. (a) B-mode image, (b) ideal strain image, (c) strain image generated by the AM method, (d) envelop power map, (e) fused map, (f) maximum intensity points on the fused map, (g) estimated bone boundary by the APS method, (h) estimated bone boundary by the SEP method, (i) MAE analysis of the SEP and APS methods at different SNRs, and (j) weight analysis at 10dB SNR (weight at minimum error is shown with red arrow). . . . .	48
2.3	Illustration of the bone boundary detection using the experimental phantom. (a) B-mode image, (b) a CT projection along which US scanning is performed, (c) strain image, (d) maximum intensity points overlaid on the fused map, (e) estimated bone boundary by the APS method, (f) estimated bone boundary by the SEP method, and (g) MAE analysis of the SEP and APS methods at different SNRs. . . . .	50
2.4	Illustration of the bone boundary detection using the <i>in vivo</i> volunteer-I data set. (a) shows the scanned region on the volunteer (shown with red rectangle), (b) is the B-mode image (bone surface is indicated with red arrows), (c) is the strain image, (d) shows the maximum intensity points overlaid on the fused map, (e) shows the detected bone boundary by the APS method, and (f) shows the detected bone boundary by the SEP method. . . . .	52

2.5	Illustration of the bone boundary detection using the <i>in vivo</i> volunteer-II data set. (a) shows the scanned region on the volunteer (shown with red rectangle), (b) is the B-mode image (bone surface is indicated with red arrows), (c) is the strain image, (d) shows the maximum intensity points overlaid on the fused map, (e) shows the detected bone boundary by the APS method, and (f) shows the detected bone boundary by the SEP method. . . . .	53
2.6	Illustration of the bone boundary detection using the <i>in vivo</i> volunteer-III data set. (a) shows the scanned region on the volunteer (shown with red rectangle), (b) is the B-mode image (bone surface is indicated with red arrows), (c) is the strain image, (d) shows the maximum intensity points overlaid on the fused map, (e) shows the detected bone boundary by the APS method, and (f) shows the detected bone boundary by the SEP method. . . . .	54
2.7	Illustration of the bone boundary detection using the <i>in vivo</i> volunteer-IV data set. (a) shows the scanned region on the volunteer (shown with red rectangle), (b) is the B-mode image (bone surface is indicated with red arrows), (c) is the strain image, (d) shows the maximum intensity points overlaid on the fused map, (e) shows the detected bone boundary by the APS method, and (f) shows the detected bone boundary by the SEP method. . . . .	55
2.8	Illustration of the bone boundary detection using the <i>in vivo</i> volunteer-V data set. (a) shows the scanned region on the volunteer (shown with red rectangle), (b) is the B-mode image (bone surface is indicated with red arrows), (c) is the strain image, (d) shows the maximum intensity points overlaid on the fused map, (e) shows the detected bone boundary by the APS method, and (f) shows the detected bone boundary by the SEP method. . . . .	57

3.1	(a) Mean absolute error (MAE) analysis for different values of $\lambda$ at 10dB SNR (weight at minimum error is shown with red arrow), (b) Normalized cross-correlation coefficients with respect to applied strains for FEM-I phantom (see Section 3.5 for detail), and (c) Normalized cross-correlation coefficient dependent linear weight $\lambda$ .	63
3.2	The alignment cost for varying cluster numbers. . . . .	65
3.3	FEM simulation phantoms. (a) FEM-I: ideal elastogram of a homogeneous soft tissue of stiffness 10kPa. (b) FEM-II: normal distal radius bone and soft tissue region of stiffness 10GPa and 10kPa, respectively, and (c) corresponding ideal elastogram. (d) FEM-III: fractured distal radius bone and soft tissue region of stiffness 10GPa and 10kPa, respectively, and (e) corresponding ideal elastogram. . . . .	67
3.4	Illustration of 2D bone boundary detection using the FEM-I phantom. (a) B-mode image, (b) strain image generated by the proposed approach, (c) MEM <sub>1</sub> , (d) Gaussian mixtures representation over fused map, and estimated bone boundary by the (e) 2DSE and (f) 2DOPS methods (arrows show leakage). Bone boundary is shown after bottom up ray-casting for the 2DOPS method. . . .	69
3.5	Illustration of 2D bone boundary detection using the FEM-II phantom. (a) B-mode image, (b) strain image generated by the proposed approach, (c) MEM <sub>1</sub> , (d) Gaussian mixtures representation over fused map, and estimated bone boundary by the (e) 2DSE and (f) 2DOPS methods (arrow shows leakage). Bone boundary is shown after bottom up ray-casting for the 2DOPS method. . . .	70
3.6	Illustration of 2D bone boundary detection using the experimental phantom. (a) B-mode image, (b) strain image generated by the proposed approach, (c) MEM <sub>1</sub> , (d) Gaussian mixtures representation over fused map, (e) estimated bone boundary by the 2DSE method, and (f) estimated bone boundary by the 2DOPS method (bone boundary is shown after bottom up ray-casting). . . . .	71

3.7	Illustration of the proposed strain-imaging performance. (a)-(d) show the B-mode images where overlaid red-dotted boxes indicate the bone locations. (e)-(h) show the strain images generated by the traditional method adopted in [29] (red arrows indicate the true bone locations while yellow arrows indicate artifacts associated with soft tissue layers), and (i)-(l) show the strain images generated by the proposed method (red arrows indicate the true bone locations). . . . .	72
3.8	Illustration of 2D bone boundary detection using the <i>in vivo</i> volunteer-I data set. (a) shows bone region scanned on the volunteer (with red rectangle), (b) is the strain image generated by the proposed approach, (c) is the MEM <sub>1</sub> , and (d) is the fused map with the Gaussian mixtures overlaid. Finally, in (e), orthopaedic expert delineated bone boundary, and detected bone boundary by the 2DOPS and 2DSE methods are overlaid on the B-mode image (bone boundary produced by the 2DOPS method is shown after bottom up ray-casting). . . . .	73
3.9	Illustration of 2D bone boundary detection using the <i>in vivo</i> volunteer-II data set. (a) shows bone region scanned on the volunteer (with red rectangle), (b) is the strain image generated by the proposed approach, (c) is the MEM <sub>1</sub> , and (d) is the fused map with the Gaussian mixtures overlaid. Finally, in (e), orthopaedic expert delineated bone boundary, and detected bone boundary by the 2DOPS and 2DSE methods are overlaid on the B-mode image (bone boundary produced by the 2DOPS method are shown after bottom up ray-casting). . . . .	74

3.10	Illustration of 2D bone boundary detection using the <i>in vivo</i> volunteer-III data set. (a) shows bone region scanned on the volunteer (with red rectangle), (b) is the strain image generated by the proposed approach, (c) is the MEM <sub>1</sub> , and (d) is the fused map with the Gaussian mixtures overlaid. Finally, in (e), orthopaedic expert delineated bone boundary, and detected bone boundary by the 2DOPS and 2DSE methods are overlaid on the B-mode image (bone boundary produced by the 2DOPS method are shown after bottom up ray-casting).	76
3.11	Illustration of 2D bone boundary detection using the <i>in vivo</i> volunteer-IV data set. (a) shows bone region scanned on the volunteer (with red rectangle), (b) is the strain image generated by the proposed approach, (c) is the MEM <sub>1</sub> , and (d) is the fused map with the Gaussian mixtures overlaid. Finally, in (e), orthopaedic expert delineated bone boundary, and detected bone boundary by the 2DOPS and 2DSE methods are overlaid on the B-mode image (bone boundary produced by the 2DOPS method are shown after bottom up ray-casting).	77
3.12	Illustration of 2D bone boundary detection using the <i>in vivo</i> volunteer-V data set. (a) shows bone region scanned on the volunteer (with red rectangle), (b) is the strain image generated by the proposed approach, (c) is the MEM <sub>1</sub> , and (d) is the fused map with the Gaussian mixtures overlaid. Finally, in (e), orthopaedic expert delineated bone boundary, and detected bone boundary by the 2DOPS and 2DSE methods are overlaid on the B-mode image (bone boundary produced by the 2DOPS method are shown after bottom up ray-casting).	78
3.13	MAE (mm) comparisons of the 2DSE and 2DOPS methods at different SNR values using (a) the FEM-II, (b) FEM-III, and (c) experimental phantoms.	81

3.14	Distributions of the estimated bone boundary points by the 2DOPS and 2DSE methods are plotted with respect to the expert delineated bone contours for volunteers-I to -V. The ‘mean $\pm$ standard-deviation’ of each distribution is shown inside the corresponding plots. . . . .	82
3.15	Mean absolute fitting error (mm) comparisons of the bone contours produced by using the Gaussian mixture regression over the ray-casted points for the 2DOPS method and the contours produced by the original 2DOPS and proposed methods. . . . .	83
4.1	Illustration of the FEM results. (a) B-mode image, (b) estimated 3D phase symmetry image by the 3DOPS method, (c) bone surface after bottom up ray-casting in (b) (arrows show leakage), and (d) estimated bone surface by the proposed method. . . . .	89
4.2	Illustration of the experimental phantom results. (a) B-mode image, (b) estimated 3D phase symmetry image, (c) bone surface after bottom up ray-casting in (b) (arrows show leakage), and (d) estimated bone surface by the proposed method. . . . .	90
4.3	Illustration of the 3D bone surface detection using the <i>in vivo</i> volunteer-I data set. (a) shows bone region scanned on the volunteer (with red rectangle), (b) is the B-mode image, (c) shows the estimated 3D phase symmetry image by the 3DOPS method, (d) shows the bone surface after bottom up ray-casting in (c), and (e) shows the estimated bone surface by the 3DSE method. . . . .	91
4.4	Illustration of the 3D bone surface detection using the <i>in vivo</i> volunteer-I data set. (a) shows bone region scanned on the volunteer (with red rectangle), (b) is the B-mode image, (c) shows the estimated 3D phase symmetry image by the 3DOPS method, (d) shows the bone surface after bottom up ray-casting in (c), and (e) shows the estimated bone surface by the 3DSE method. . . . .	93

4.5	Illustration of the 3D bone surface detection using the <i>in vivo</i> volunteer-I data set. (a) shows bone region scanned on the volunteer (with red rectangle), (b) is the B-mode image, (c) shows the estimated 3D phase symmetry image by the 3DOPS method, (d) shows the bone surface after bottom up ray-casting in (c), and (e) shows the estimated bone surface by the 3DSE method. . . . .	94
4.6	MAE analysis of the 3DSE and 3DOPS methods at different SNRs using (a) the FEM and (b) experimental phantom data. . . . .	95
4.7	Diagrams showing the computation time breakdown for different components of the (a) 3DOPS and (b) 3DSE methods. . . . .	96

## List of Abbreviations

Abbreviation	Definition
US	Ultrasound
RF	Radio-frequency
U.S.	United States
CAOS	Computer Assisted Orthopedic Surgery
OR	Operating Room
1D	One Dimensional
2D	Two Dimensional
3D	Three Dimensional
FEM	Finite Element Model
MAE	Mean Absolute Error
CT	Computed Tomography
MRI	Magnetic Resonance Imaging
MIS	Minimally Invasive Surgery
VGH	Vancouver General Hospital
NSERC	Natural Sciences and Engineering Research Council of Canada
RMS	Root Mean Square
GMM	Gaussian Mixture Models
GMR	Gaussian Mixture Regression
NCC	Normalized Cross Correlation
ROI	Region of Interest
SNR	Signal-to-Noise Ratio
MSM	Modified Strain Map
MEM	Modified Envelope Map
FM	Fused Map
PVC	Polyvinyl Chloride
CHHM	Centre for Hip Health and Mobility
GPU	Graphics Processing Unit
CREB	Clinical Research Ethics Board



## Acknowledgements

After the Almighty, it is my great pleasure to express gratitude to the people who made this thesis possible. Foremost, I would like to express my deepest gratitude to my supervisors, Prof. Rafeef Abugharbieh, PhD, and Prof. Antony J. Hodgson, PhD, whose expertise, understanding and patience, added significantly to my graduate experience. This study could have never been done without my supervisors' motivation, guidance and inspiration. I would also like to thank Prof. Pierre Guy, MD, MBA, who sacrificed his valuable time to demonstrate me the real trauma surgeries in the operating room at the Vancouver general hospital (VGH), and also to delineate the bone surfaces on the B-mode images that ultimately are considered as the ground truth in our clinical data-based validation.

I also like to remember my mentor Prof. Md. Kamrul Hasan of Bangladesh University of Engineering and Technology (BUET), who supervised my B.Sc. and M.Sc. theses. He taught me how to work with the medical ultrasound imaging system that ultimately helped me cent percent while I worked on this project.

I would like to acknowledge the Natural Sciences and Engineering Research Council of Canada (NSERC) grants no.: 03-4685 and 03-4813 (UBC) that supported this project. I would like to thank the Centre for Hip Health and Mobility for providing the lab facilities and the Institute for Computing, Information and Cognitive Systems for program support.

I would also like to thank my parents, my wife, and my two and half years old daughter for their support. Moving to a different continent to pursue another graduate degree was a huge step for me, and their encouragement and support were invaluable to me as I progressed through this phase of my life. Without them, I would not be the person I am today. Specially, I feel greatly in debt to my wife who has been raising our child all alone while allowing me to be seven thousand miles apart. This huge sacrifice of her was a great inspiration for me.

Finally, I must say that working with brilliant researchers in the Biomedical Signal and Image Computing Laboratory (BiSICL) at the University of British Columbia was my great honor. They provided a friendly environment for me to learn and grow.

# Dedication

*To my family*

# Chapter 1

## Introduction and Background

### 1.1 Motivation and Problem Statement

Orthopedic surgery focuses on the diagnosis, treatment, rehabilitation and prevention of diseases of the bones, joints, ligament, muscles, tendons and nerves. In these surgeries, orthopedic surgeons deal with various musculoskeletal diseases and conditions, such as: (a) bone fractures and dislocations; (b) torn ligaments, sprains and strains; (c) tendon injuries, pulled muscles and bursitis; (d) ruptured disks, sciatica, lower back pain and scoliosis; (e) abnormalities of the fingers and toes and growth abnormalities; (f) surgical management of degenerative joint disease; (g) knock knees, bow legs, bunions and hammer toes; (h) arthritis and osteoporosis; (i) bone tumors, muscular dystrophy and cerebral palsy; and, (j) club feet and unequal leg length. In 2005, at least one of these musculoskeletal conditions was reported by 107.67 million adults in the United States (the U.S.), representing nearly one in two persons aged 18 and older [30]. These clinical conditions often require high risk surgery to improve the quality of the patients' lives after recovery. Moreover, the cost (direct and indirect) of these conditions is approximately \$849 billion annually in the U.S. alone [30].

Typically, during an orthopedic surgery, surgical tools and mechanical implants are primarily guided or visualized by X-ray-based fluoroscopy (discussed in detail in Section 1.2.2.1). Some surgeries (e.g., bone grafting, knee arthroplasty, pelvic fracture realignment) take, on average, over one and a half hours

during which the patient and the operating room (OR) staff are exposed to an approximately 11.2 minutes of fluoroscopic radiation [31]. This exposure time does not include the time required to re-position the fluoroscopic C-arm; therefore, operating the C-arm is one of the most time consuming steps of a fracture realignment surgery. Minimizing the use of fluoroscopy in these procedures would not only decrease the radiation exposure to the patients and staff but could also feasibly decrease the overall time required in an OR.

In order to decrease the radiation exposure, surgery time and overall orthopedic surgical cost, an emerging interest has recently been taking place towards the computer assisted orthopedic surgery (CAOS) procedure [32]. The term, CAOS, stands for the approaches that aim to improve the surgical field's visibility and increase the accuracy of the surgical procedures by employing a navigation system when carrying out surgical action. These goals are achieved by linking the bony anatomy being operated on with a virtual representation, such as an image data set [32]. Surgical navigation systems that use modern tracking technology are introduced and classified according to the chosen virtual representation of the surgical object, i.e, image-free and image-based (pre-operative and intra-operative) technology. Within the latter class in particular, computed tomography (CT)- and fluoroscopy-based systems have made their way successfully into the CAOS OR [32].

However, since CT scans and fluoroscopy are significant sources of radiation, as we discussed briefly above, there has been an emerging interest in safer, non-ionizing real-time imaging alternatives such as the ultrasound (US) [33]. Generally, an ultrasound guided surgical system has four major parts:

1. Pre-operative imaging (US, CT, etc.) and segmentation
2. Intra-operative ultrasound imaging and segmentation
3. Pre- and intra-operative segmented image registration
4. Tracking of the ultrasound probe and surgical tools for the surgical procedure

These major system parts are shown in Fig. 1.1 with numbered super blocks (dotted boxes). These numbers correspond to the aforementioned parts listed. In

this system, ‘bone segmentation in ultrasound images’ is one of the steps (shown in Fig. 1.1 with the smaller red block) which is the most crucial, challenging and error prone. Note that the ultrasound can be used as both the pre- and intra-operative imaging modality. If ultrasound is also used as the pre-operative imaging system, then our thesis work will also include the segmentation block of Super block ‘1’ in Fig. 1.1.

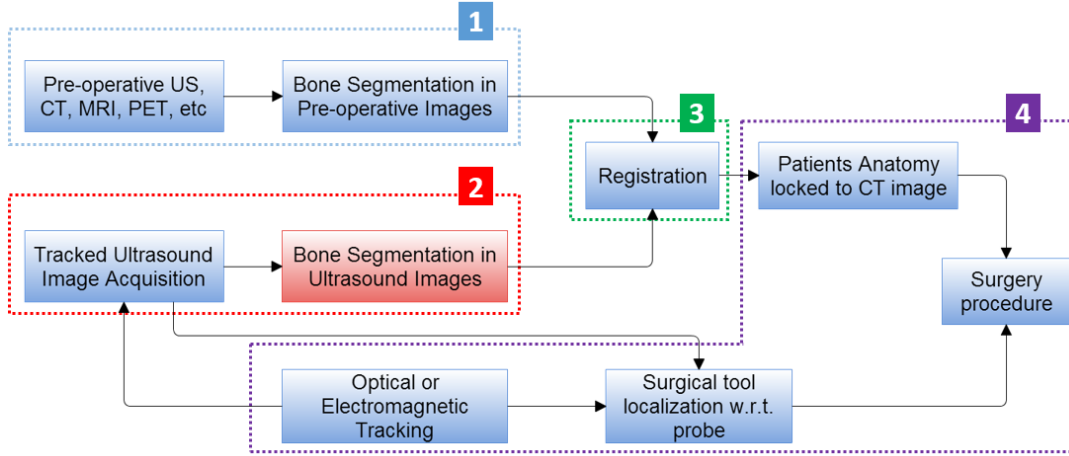


Figure 1.1: A bird eye view of the ultrasound guided surgical tool navigation system in a CAOS procedure. Major system parts are shown as super-blocks with numbered-dotted-boxes.

## 1.2 Medical Imaging in Orthopedic Surgery

In this section, we describe the medical imaging modalities currently being employed pre- and intra-operatively. Pre-operative imaging modalities are typically used to diagnose orthopedic clinical conditions and/or in planning surgery procedures, while intra-operative imaging modalities are used to assess fractured bone realignment performance, and to visualize and/or navigate surgical implants, tools, and other associated materials. For the sake of discussion, in this section, we are considering X-ray, X-ray CT, and magnetic resonance imaging (MRI) as the pre-operative imaging modalities, while fluoroscopy and medical ultrasound will be the intra-operative imaging modalities. However, these modalities are often used interchangeably or solo depending on the requirements and surgical

plans. For example, we have already discussed, in Section 1.1, the fact that the ultrasound imaging system can be used for both the pre- and intra-operative purposes.

## 1.2.1 Pre-operative Imaging

### 1.2.1.1 The X-ray

The most common and widely used medical imaging modality that is typically used for orthopedic diagnostic purposes is the X-ray. When a patient is admitted to a hospital with a suspected clinical orthopedic condition, standard X-ray images are first taken. X-radiation (composed of X-rays) is a type of electromagnetic radiation. Most X-rays have a wavelength ranging from 0.01 to 10nm, corresponding to frequencies in the range of from 30PHz to 30EHz ( $3 \times 10^{16}$ Hz to  $3 \times 10^{19}$ Hz), and energies in the range 100eV to 100keV. X-ray wavelengths are shorter than those of ultraviolet rays and typically longer than those of gamma rays. Different applications use different parts of the X-ray spectrum, as shown in Fig. 1.2. In many languages, X-radiation is referred to as Röntgen radiation, named after Wilhelm Röntgen, who won the Nobel Prize in Physics as its inventor in 1901 [34].

Use of X-ray-based imaging for diagnostic purposes is typically known as radiography. A radiograph is an X-ray image obtained by placing a part of the patient in front of an X-ray detector and then illuminating it with a short X-ray pulse. Bones contain a large amount of calcium, which, due to its relatively high atomic number, efficiently absorbs X-rays. This reduces the number of X-rays reaching the detector in the shadow from the bones, making them clearly visible on the radiograph. Radiographs are useful in the detection of pathology in the skeletal system as well as for detecting some disease processes in soft tissue. One notable example is the chest X-ray, which can be used to identify any orthopedic conditions.

X-ray photons carry sufficient energy to ionize atoms and disrupt molecular bonds. This makes the process a type of ionizing radiation, and thus harmful to living tissue. A very high radiation dose over a short period of time causes radiation sickness, while lower doses can provide an increased risk of radiation-

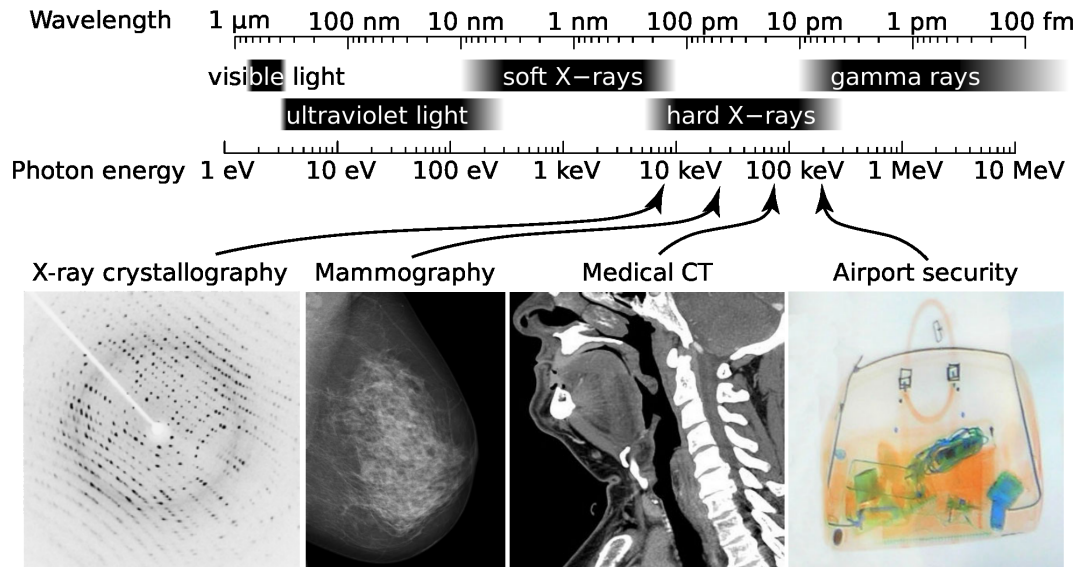


Figure 1.2: X-rays are part of the electromagnetic spectrum, with wavelengths shorter than visible light. Different applications use different parts of the X-ray spectrum [2].

induced cancer. In medical imaging this increased cancer risk is generally greatly outweighed by the benefits of the examination. The ionizing capability of X-rays can be utilized in cancer treatment to kill malignant cells through radiation therapy.

#### 1.2.1.2 Computed Tomography (CT) Scan

X-ray computed tomography is a technology that uses computer-processed X-rays to produce tomographic images of specific areas of a scanned object, allowing the user to noninvasively view the inside of the object. As the X-ray CT scan is the most common form of CT used in medicine and various other contexts, the term “computed tomography” alone is often used to refer to the X-ray CT scan. Digital geometry processing is used to generate a three-dimensional image of the inside of an object from a large series of two-dimensional radiographic images taken around a single axis of rotation [35]. Medical imaging is the most common application of CT. Its cross-sectional images are used for diagnostic and therapeutic purposes in various medical disciplines, especially in the orthopedics.

X-ray slice data is generated using an X-ray source that rotates around the

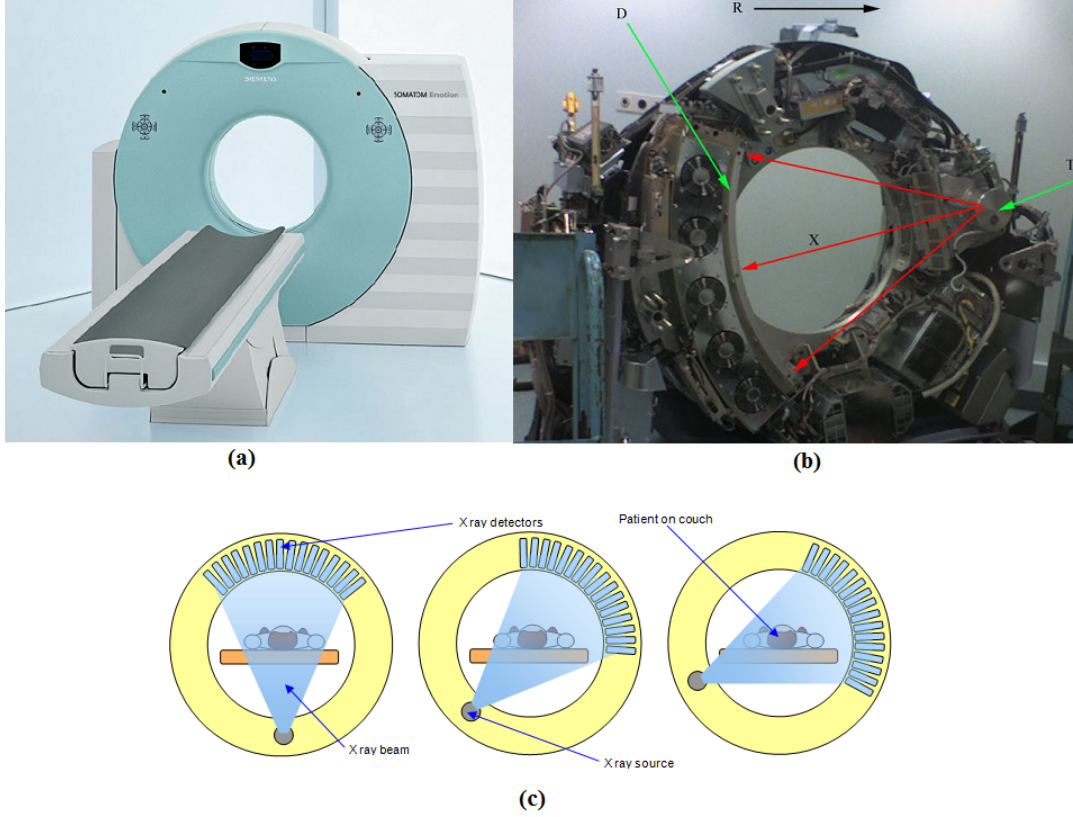


Figure 1.3: (a) An X-ray CT scanner [3], (b) an X-ray CT scanner with cover removed to show internal components. Legend- T: X-ray tube, D: X-ray detectors, X: X-ray beam, and R: Gantry rotation [4]. (c) A schematic image of a CT scanner with X-ray source and detectors shown in three position [5].

object; X-ray sensors are positioned on the opposite side of the circle from the X-ray source (shown in Fig. 1.3(b)). Initial machines would rotate the X-ray source and detectors around a stationary object as shown in Fig. 1.3(c). Following a complete rotation, the object would be moved along its axis, and the next rotation initialized. Newer machines permit a continuous rotation with the object to be imaged by sliding it slowly and smoothly through the X-ray ring. These are called helical or spiral CT machines. A subsequent development of the helical CT is the multi-slice (or multi-detector) CT; rather than employing a single row of detectors, the device uses multiple rows of detectors, simultaneously capturing multiple cross-sections. A schematic diagram of multi-slice helical CT acquisition



process is shown in Fig. 1.4.

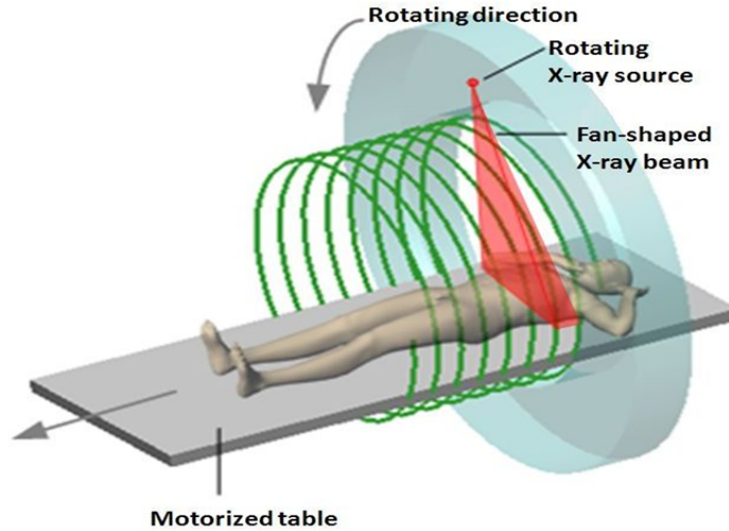


Figure 1.4: A schematic diagram of multi-slice helical CT acquisition process [6].

The CT is often used to image complex fractures, especially ones surrounding the joints, because of its ability to reconstruct the area of interest in multiple planes. Fractures, ligamentous injuries and dislocations can easily be recognized with a 0.2mm resolution [36]. However, CT imaging is a major source of radiation. A typical plain film X-ray involves a radiation dose of 0.01 to 0.15mGy, while a typical CT can involve doses of 10–20mGy for specific organs, and this can reach as high as 80mGy in certain specialized CT scans [37]. One gray (Gy) is equivalent to the absorption of one joule of radiation energy per one kilogram of matter. The radiation dose reported in the gray or mGy unit is proportional to the amount of energy that the irradiated body part is expected to absorb, and the degree of physical effect (such as the creation of DNA double strand breaks) on the cells' chemical bonds by X-ray radiation is proportional to that energy [37].

### 1.2.1.3 Magnetic Resonance Imaging (MRI)

Magnetic resonance imaging is a medical imaging technique used in radiology to investigate the anatomy and physiology of the body during both health and disease states. MRI scanners employ magnetic fields and radio waves to form im-

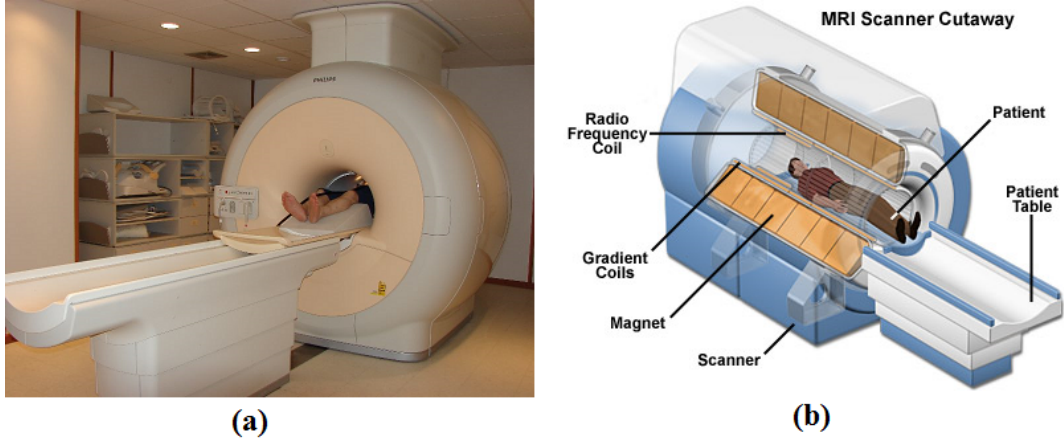


Figure 1.5: (a) An illustration of a real MRI scanner [7], and (b) a cutaway schematic image of an MRI scanner [8].

ages of the body. The technique is widely used in hospitals for medical diagnosis and, the staging of diseases and to perform follow-ups without causing exposure to ionizing radiation. In orthopedics, an MRI may be used to examine bones, joints, and such soft tissues as cartilage, muscles, and tendons for injuries, the presence of structural abnormalities or certain other conditions, such as tumors, inflammatory diseases, congenital abnormalities, osteonecrosis, bone marrow diseases, and herniation or the degeneration of discs of the spinal cord. The MRI may be used to assess the results of corrective orthopedic procedures. Joint deterioration resulting from arthritis may be monitored by using magnetic resonance imaging.

To perform a study, the patient is positioned within an MRI scanner which forms a strong magnetic field around the area to be imaged. In most medical applications, protons (hydrogen atoms) in tissues containing water molecules are used to create a signal that is processed to form an image of the body. First, energy from an oscillating magnetic field is temporarily applied to the patient at the appropriate resonance frequency. The excited hydrogen atoms emit a radio frequency signal which is measured by a receiving coil. The radio signal can be made to encode position information by varying the main magnetic field using gradient coils. As these coils are rapidly switched on and off, they create the characteristic repetitive noise of the MRI scan. The contrast between different

tissues is determined by the rate at which the excited atoms return to their equilibrium state. A real life MRI scanner is shown in Fig. 1.5(a), while a cutaway schematic image of an MRI scanner is shown with detailed legends in Fig. 1.5(b).

Although an MRI system is completely radiation free, due to the use in the device of a strong magnet, special precautions must be taken to perform MRI scans on patients processing certain implanted devices such as pacemakers or cochlear implants. The MRI technologist needs to obtain information regarding the implanted device, such as its make and model number, to determine if it is safe to perform an MRI. Patients with internal metal objects, such as surgical clips, plates, screws or wire mesh, might not be eligible for MRI examinations.

## 1.2.2 Intra-operative Imaging

### 1.2.2.1 Fluoroscopy

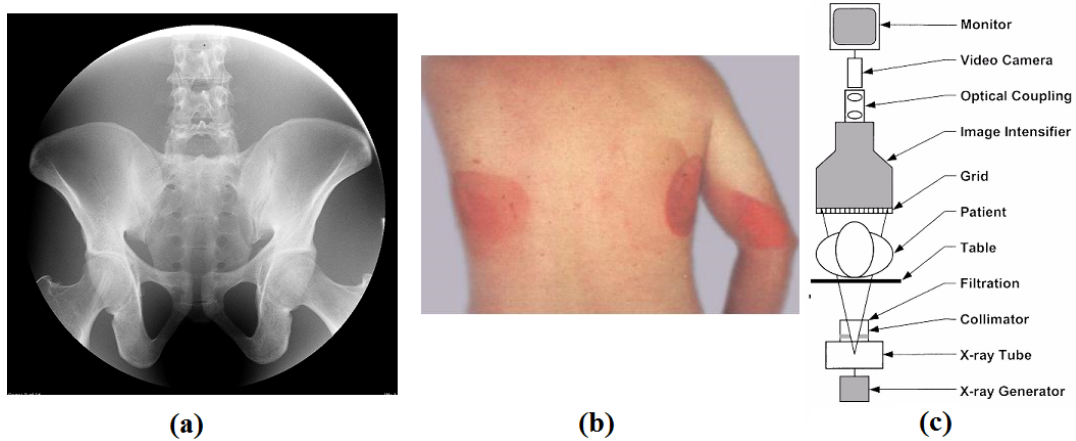


Figure 1.6: (a) A typical fluoroscopic image of the human pelvic region [9], (b) fluoroscopic burn from long exposure [10], and (c) a diagram showing the components of a fluoroscopic imaging chain [11].

Fluoroscopy is a method providing real-time X-ray imaging that is especially useful for guiding a variety of orthopedic diagnostic and interventional procedures. The ability of fluoroscopy to display motion is provided by a continuous series of images produced at a maximum rate of 25–30 complete images per sec-

ond. This is similar to the means by which conventional television or video transmits images. The acquired images are transmitted to a digital monitor such that the body part and its motion can be seen in detail. Fluoroscopy, as an imaging tool, enables physicians to observe numerous body systems, including the skeletal, digestive, urinary, respiratory, and reproductive systems. Fluoroscopy may be performed to evaluate the immediate condition of bones, muscles, and joints. A typical fluoroscopic image of the human pelvic region is shown in Fig. 1.6(a).

Fluoroscopy and radiography share some of the same imaging chain components, but difference between them exist. The primary difference is that the radiation exposure rate is much lower for fluoroscopy as compared with that of radiography. A fluoroscopy of an average-sized adult abdomen typically requires approximately 45mGy/min [11]. For an abdominal radiograph, the entrance skin exposure to the patient is approximately 3mGy with an exposure time of 200msec for an exposure rate of 900mGy/min, which is 20 times higher than the rate for a fluoroscopy. However, the total exposure for a radiograph is much lower than a typical fluoroscopic examination because the fluoroscopic exposure time is extended [11]. For 10 minutes of abdominal fluoroscopy, the total patient exposure is approximately 450mGy, as compared with 3mGy for a radiograph. Long fluoroscopic exposure causes skin and muscle burn; an example of this is shown in Fig. 1.6(b).

#### **1.2.2.2 Ultrasonography**

Ultrasound imaging also known as ultrasonography or simply sonography, uses high-frequency sound waves to view the internal regions of the body. It is the most economical and widely available medical imaging modality. Because ultrasound images are captured in real-time, they can also show the movements of the body's internal organs as well as the blood's passage through the blood vessels. Unlike X-ray imaging, no ionizing radiation exposure is associated with ultrasound imaging. Two modern medical ultrasound scanners are shown in Figs. 1.7(a) and (b). Typical diagnostic sonographic scanners operate in the frequency range of 1 to 18MHz, although frequencies of up to 50–100MHz have been used experimentally in a technique known as biomicroscopy in special regions of the body, including the eye's anterior chamber [38].

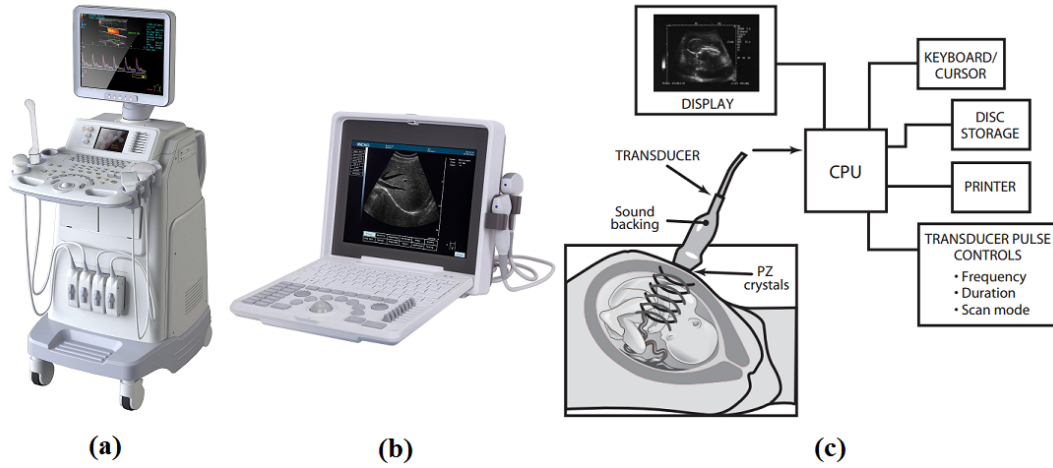


Figure 1.7: (a) A modern medical ultrasound scanner [12], (b) a modern portable ultrasound scanner [13], and (c) a schematic diagram of the parts of an ultrasound scanner.

A schematic diagram of the parts of an ultrasound scanner is shown in Fig. 1.7(c). In an ultrasound examination, a transducer both sends sound waves and receives their echoing waves. When the transducer is pressed against the skin, it directs small pulses of inaudible, high-frequency sound waves into the body. As the sound waves bounce off internal organs, fluids and tissues, the sensitive microphone in the transducer records tiny changes in the sound's pitch and direction. These signature waves are instantly measured and displayed by a computer, which in turn creates a real-time picture of the information found on the monitor. One or more frames of moving pictures are typically captured as still images. Small loops of moving “real time” images may also be saved.

Since this thesis work is based on the medical ultrasound, technical details of ultrasound data acquisition and its subsequent processing are described in Section 1.3.

### 1.3 The Basic Physics of Ultrasound Imaging

Ultrasound has been used to visualize the living body's internal recesses for over half a century. An Austrian neurologist, Dr. Karl Theo Dussik was the first to apply ultrasound as a medical diagnostic tool to image the brain [39]. At

present, ultrasound is one of the most widely used imaging technologies found in medicine. It is portable, free of radiation risk, and relatively inexpensive when compared with other imaging modalities, such as the MRI and CT scans. Furthermore, ultrasound images are tomographic, i.e., they offer a “cross-sectional” view of anatomical structures. Here, we describe some of the fundamental principles and physics underlying ultrasound technology.

### 1.3.1 Sound Properties

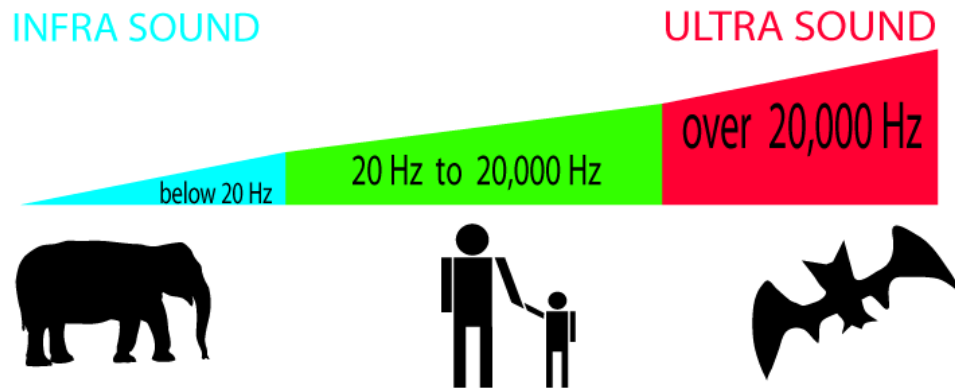


Figure 1.8: Sound frequency ranges for infrasound, audible (sound) and ultrasound waves and the corresponding mammals that can hear them [14].

Sound is a vibration that is transmitted through a medium (e.g., air) that can be detected by the human ear. Sound specifically refers to such information as the human ear is able to perceive, or “hear”. All vibrations, including sound, have a frequency. Frequency is a measure of the number of times something “vibrates” per second. The unit of frequency is Hertz (Hz), interpreted as “vibrations per second”. The human ear can hear frequencies of between about 20 to 20,000Hz. Therefore, “sound” refers to vibrations within this frequency range. Any vibration below 20Hz is called infrasound, while those beyond 20,000Hz are known as ultrasound (US). Frequency ranges for infrasound, sound and ultrasound waves are shown in Fig. 1.8. The US wavelengths and frequencies are inversely related, i.e., high frequency US has a short wavelength, and vice versa. Medical ultra-

sound devices use sound waves in the range of 1–20MHz. The proper selection of transducer frequency is an important criterium for providing optimal image resolution in diagnostic and procedural ultrasound. High-frequency ultrasound waves (of short wavelength) generate images of high axial resolution. Increasing the number of waves of compression and rarefaction for a given distance can help to more accurately discriminate between two separate structures along the axial plane of wave propagation. However, at a given distance, high-frequency waves are more attenuated than those of lower frequency; thus, they are mainly suitable for imaging superficial structures [40]. Conversely, low-frequency waves (of long wavelength) offer images which are of lower resolution but can penetrate to deeper structures due to their lower degree of attenuation. A comparison of the resolution and penetration of different ultrasound transducer frequencies is shown in Fig. 1.9.

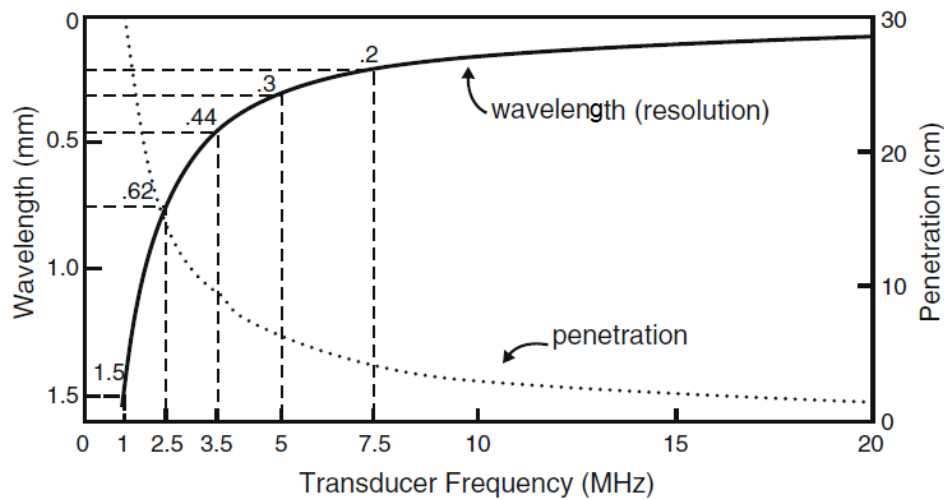


Figure 1.9: A comparison of the resolution and penetration of different ultrasound transducer frequencies [15].

### 1.3.2 The Generation and Reception of Ultrasound Pulses

Ultrasound transducers (or probes) contain multiple numbers of a special type of crystal known as piezoelectric crystals, which are interconnected electronically and vibrate in response to the potential applied across them. This phenomenon is

referred to as the piezoelectric effect. In 1880, the French physicists Pierre Curie, and his elder brother Jacques Curie, discovered the piezoelectric effect in certain crystals [15]. They also demonstrated the reverse piezoelectric effect, i.e., the application of electrical current to the quartz resulting in quartz vibrations [41]. Latter, Paul Langevin, a student of Pierre Curie, developed piezoelectric materials, which can generate and receive mechanical vibrations with high frequency, and are therefore ultrasonic. These vibrating mechanical sound waves create alternating areas of compression and rarefaction when propagated through body tissues.

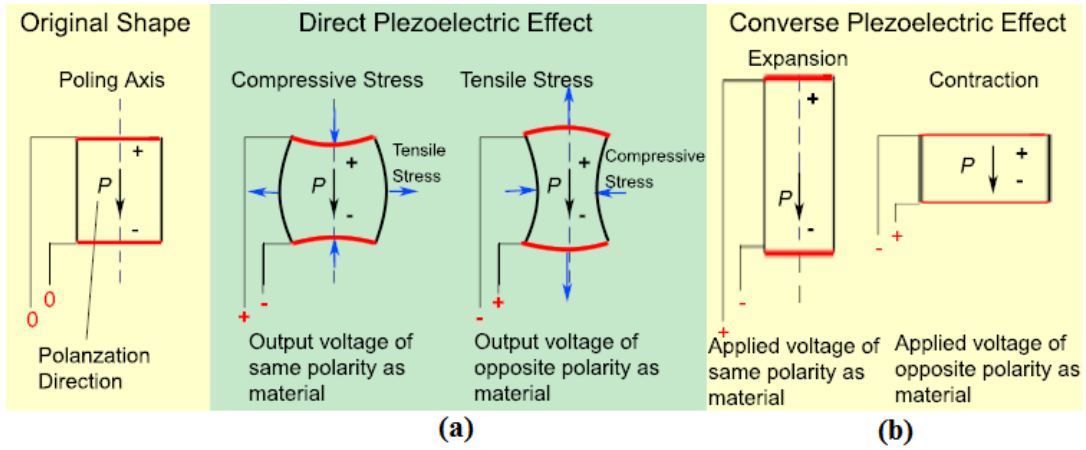
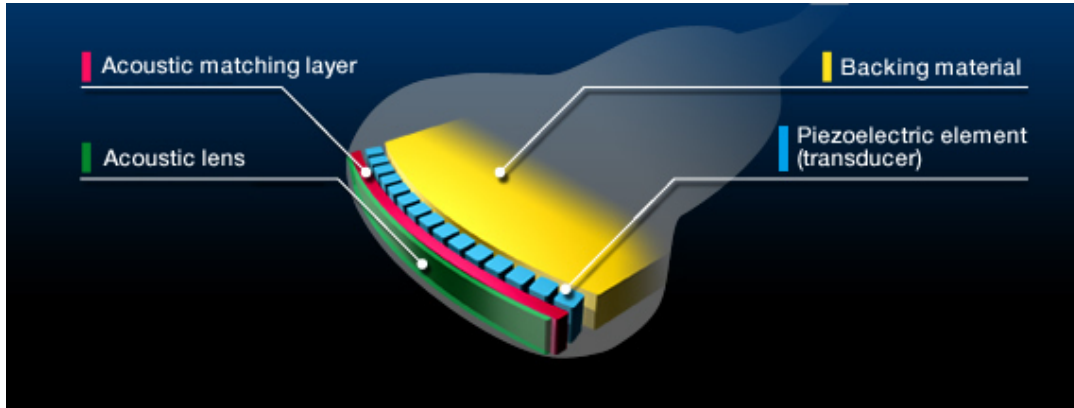


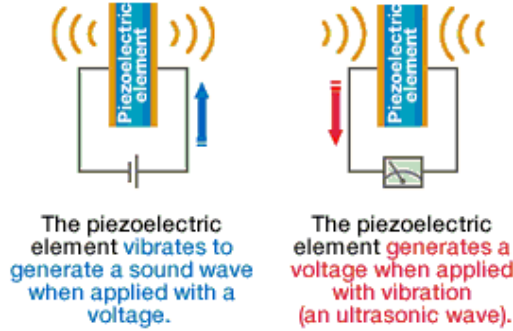
Figure 1.10: The (a) direct and (b) converse piezoelectric effect. Mechanical deformation and consequent oscillation caused by an electrical field applied to certain material can produce a sound of high frequency [16].

The piezoelectric effect (or, direct piezoelectric effect) is a phenomenon exhibited by the generation of an electric charge in response to a mechanical force (squeeze or stretch) applied on certain materials (see Fig. 1.10(a)). Conversely, mechanical deformation can be produced when an electric field is applied to such material, also known as the converse piezoelectric effect (see Fig. 1.10(b)). Both natural and human-made materials, including quartz crystals and ceramic materials, can demonstrate piezoelectric properties. By stacking piezoelectric elements into layers in a transducer (see Fig. 1.11(a)), the latter can convert electric energy into mechanical oscillations in pulse transmissions; these mechanical oscillations are then converted into electrical energy in echo reception (see





(a)



(b)

Figure 1.11: (a) Different components of a convex type ultrasound probe, and (b) a graphical representation of the pulse transmission and reception of a piezoelectric crystal [17].

Fig. 1.11(b)). The stacking of the piezoelectric elements are called transducer arrays or elements (shown as blue array components in Fig. 1.11(a)).

Some other essential components of the pulse generation system are the backing material, acoustic matching layer, and acoustic lens. The backing material is located behind the piezoelectric element to prevent excessive vibration (see Figs. 1.11(a) and 1.12(a)). It reduces the latter so that the element can generate ultrasonic waves with shorter pulse lengths, improving axial resolution in images. On the other hand, ultrasonic waves transmitted from the piezoelectric element are reflected off a target because there is a big difference in acoustic impedance between the piezoelectric element and the object. To avoid this phenomenon, an

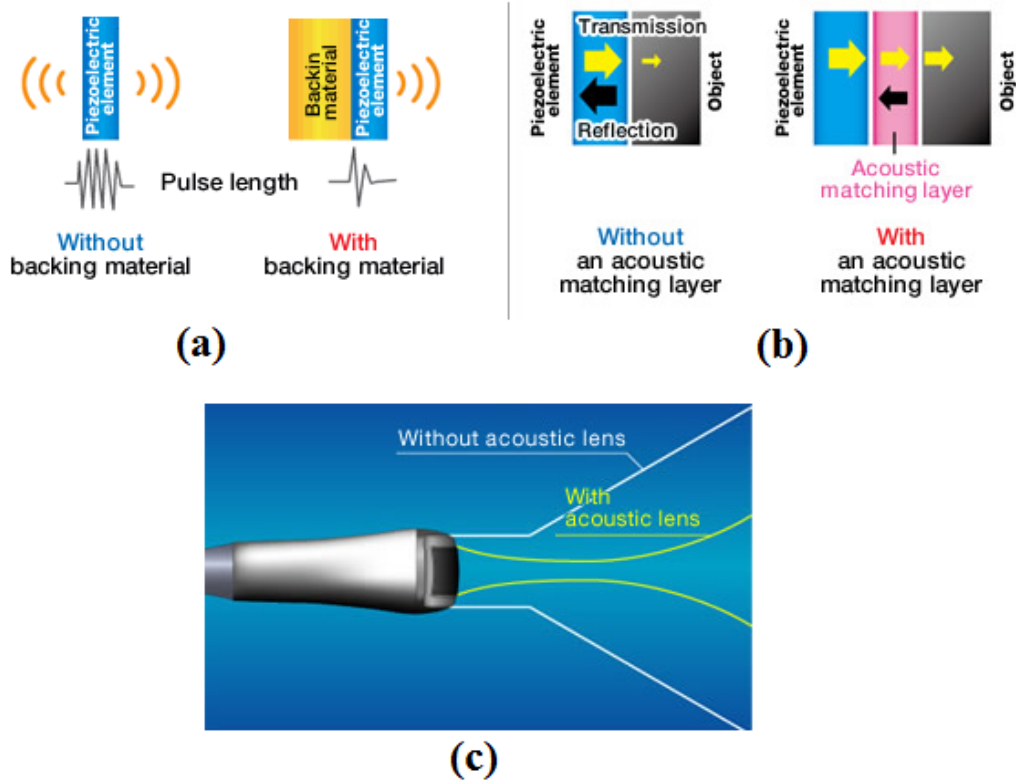


Figure 1.12: Illustration of the (a) function of the backing material, (b) function of the acoustic matching layer, and (c) function of the acoustic lens [17].

intermediate material called the acoustic matching layer is inserted between the two (see Figs. 1.11(a) and 1.12(b)) so that ultrasonic waves can efficiently enter the object. The acoustic lens is a rubber like material attached to the tip of the probe (shown in green in Fig. 1.11(a) and in grey in Fig. 1.12(c)). Ultrasonic waves transmitted from the probe would spread and travel like light. The acoustic lens prevents the ultrasonic waves from spreading and focuses them in the slice direction to improve the image resolution. Further focusing and steering of ultrasound beam can be done by using delays in the pulsing of elements (see Fig. 1.13). This type of arrangement is called a phased or steered array.

Ultrasound waves are generated in pulses (intermittent trains of pressure) that commonly consist of two or three sound cycles of the same frequency (see Fig. 1.14). The pulse repetition frequency (PRF) is the number of pulses emitted by

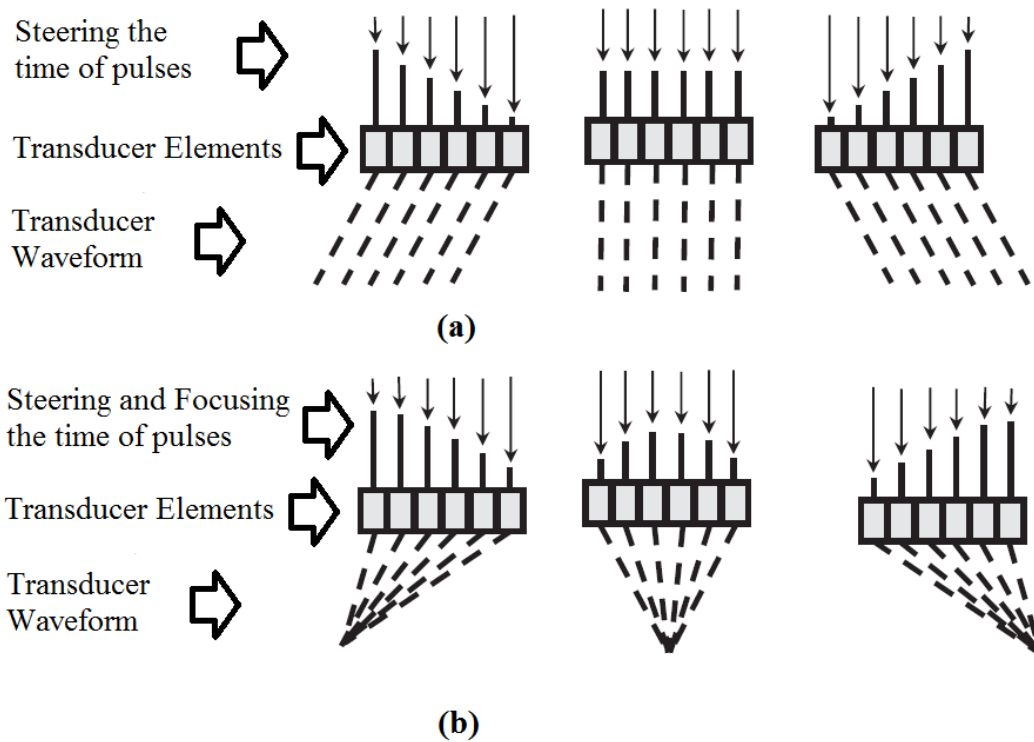


Figure 1.13: Electronic steering and focusing of ultrasound beam [18].

the transducer per unit of time. Ultrasound waves must be emitted in pulses with sufficient time between them to allow the signal to reach the target of interest and then be reflected back to the transducer as an echo before the next pulse is generated. The PRF for medical imaging devices ranges from 1 to 10kHz [19].

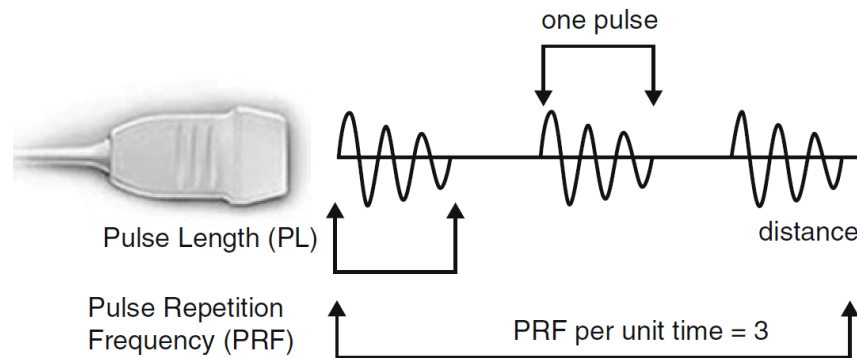


Figure 1.14: Schematic representation of ultrasound pulse generation [19].

Body Tissue	Acoustic Impedance ( $10^6 \text{Rayls}$ )
Air	0.0004
Lung	0.18
Fat	1.34
Liver	1.65
Blood	1.65
Kidney	1.63
Muscle	1.71
Bone	7.8

Table 1.1: Acoustic impedances of different body tissues and organs [1].

### 1.3.3 Ultrasound-tissue Interaction

As ultrasound waves travel through tissues, they are partly transmitted to deeper structures, partly reflected back to the transducer as echoes, partly scattered, and partly transformed into heat [40]. The echoes reflected back to the transducer produce the image. The amount of echo returned after interacting with a tissue particle is determined by a tissue property called acoustic impedance. This is the intrinsic physical property of a medium defined as the density of the medium times the velocity of the ultrasound wave propagation through the medium. Ultrasound wave propagation speed is the speed at which sound can travel through a medium and is typically 1540m/sec for soft tissue. The speed is determined solely by the medium’s characteristics, particularly those of density and stiffness [18]. Organs containing air (e.g., the lungs) have the lowest acoustic impedance, while dense organs (e.g., bone) have very high-acoustic impedance (see Table 1.1). The intensity of a reflected echo is proportional to the difference in acoustic impedance between the two mediums [19]. If two tissues have identical acoustic impedance, no echo is generated. Interfaces between soft tissues of similar acoustic impedance usually generate low-intensity echoes. Conversely, interfaces between soft tissue and bone generate very strong echoes due to a large acoustic impedance gradient [42].

When an incident pulse encounters a large and smooth interface of two different types of tissues possessing different degrees of acoustic impedance, the type

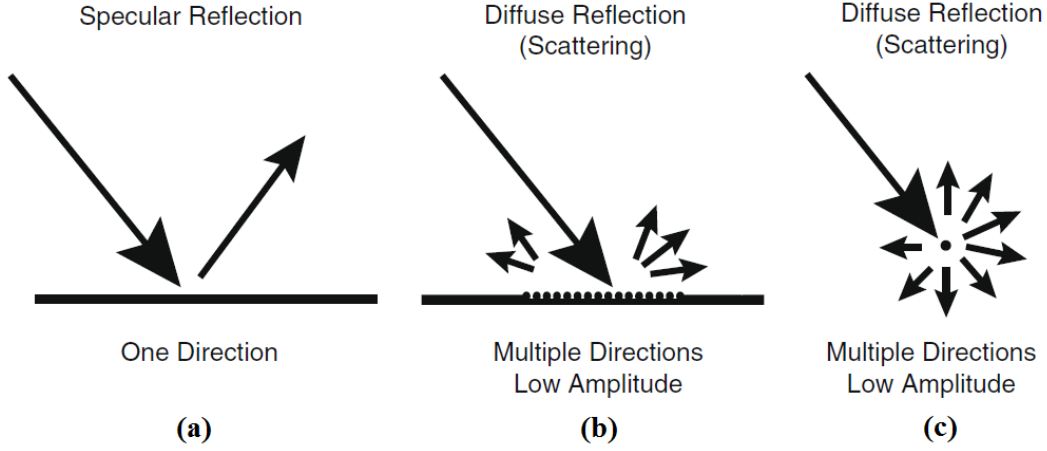


Figure 1.15: Different types of ultrasound wave-tissue interactions [1].

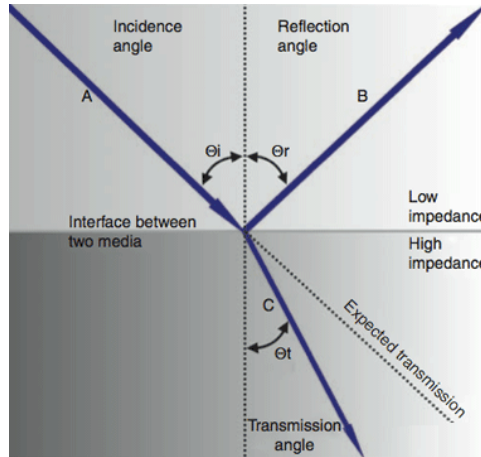


Figure 1.16: Reflection and refraction of the ultrasound beams [20].

of reflection from this interface is called “specular reflection”, and the echo intensity generated is proportional to the difference between their acoustic impedance values (see Fig. 1.15(a)). A soft tissue-needle interface at the point where a needle is inserted “in-plane” (where the needle and transducer faces are parallel) is a good example of specular reflection. If the incident ultrasound beam reaches the linear interface at  $90^\circ$ , almost all of the generated echo will travel back to the transducer. However, if the angle of incidence with the specular boundary is less than  $90^\circ$ , the echo will not return to the transducer, but rather be reflected at an angle equal to the angle of incidence (i.e.,  $\angle\Theta_i = \angle\Theta_r$  in Fig. 1.16). The

returning echo will potentially miss the transducer and not be detected [19].

If the ultrasound pulse encounters reflectors whose dimensions are smaller than the ultrasound wavelength, or when the pulse encounters a rough, irregular tissue interface, scattering occurs (see Figs. 1.15(b) and (c)). In this case, echoes reflected through a wide range of angles result in a reduction in echo intensity. However, some echoes return to the transducer regardless of the angle of the incident pulse. Most biologic tissues are filled with tiny scattering structures. The speckle signal that provides organs' visible texture is a result of scattered echoes produced within the volume of the incident ultrasound pulse [19].

As ultrasound pulses travel through tissue along their depth, their intensity is reduced or attenuated. This attenuation is the result of reflection and scattering, and also of friction-like losses [40]. These losses result from the induced oscillatory tissue motion produced by the pulse, which causes a conversion of energy from the original mechanical form into heat. This energy loss to localized heating is referred to as absorption and is the most important contributor to ultrasound attenuation [19]. Longer path length and higher frequency waves result in greater attenuation. Attenuation also varies among body tissues, with the highest degree for any given frequency found in bone, a lesser degree in muscle and solid organs, and the lowest in blood.

### 1.3.4 Ultrasound Beamforming

Ultrasound receiving beamforming or image formation is usually performed by sequential insonification of the medium using focused beams. Each focused beam allows the reconstruction of one image line (known as the scan-line or A-line). A typical 2D image is made of a good number of A-lines (e.g., 64~512). There are a number of advanced beamforming techniques available, including synthetic receive aperture, parallel beamforming, spatial compounding, adaptive beamforming technique [43]. However, a simple image acquisition process is illustrated in Fig. 1.17. Typically, a subset of the total transducer elements transmits the pulse and receives the reflected echoes; then a delay-and-sum operation is performed over the received pulse sequences and forms the beamformed A-line. This operation repeats by sliding the subset elements along the transducer arrays, with an

overlap from one end to other of the array.

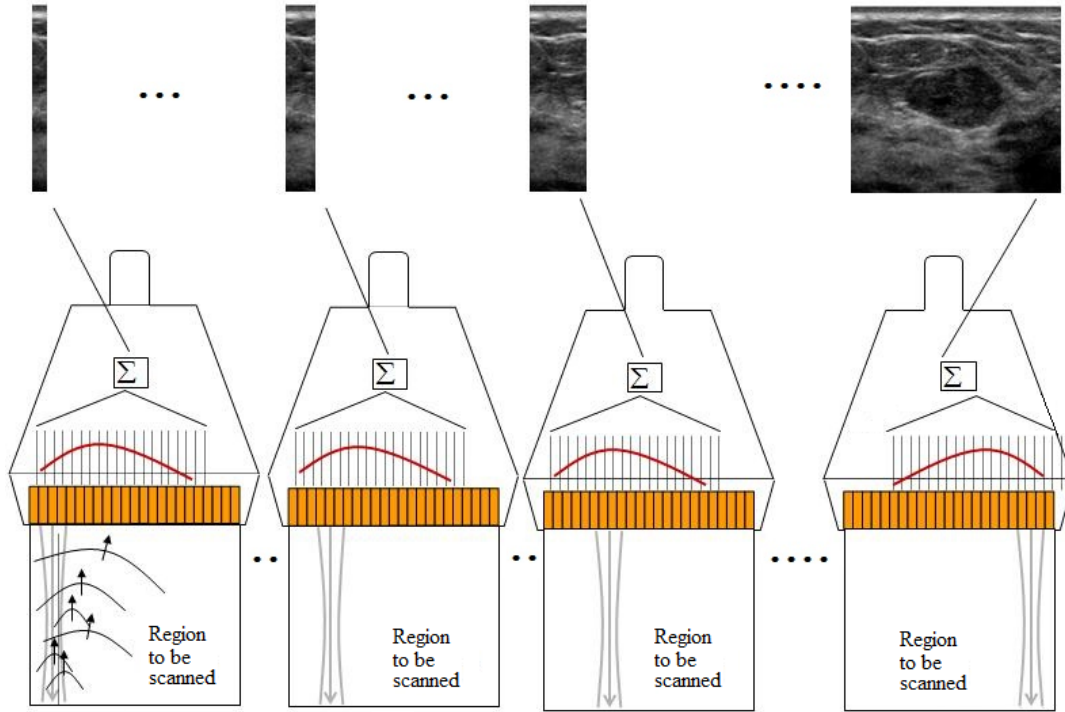


Figure 1.17: Ultrasound image acquisition process [21].

### 1.3.5 Ultrasound B-mode Image Formation

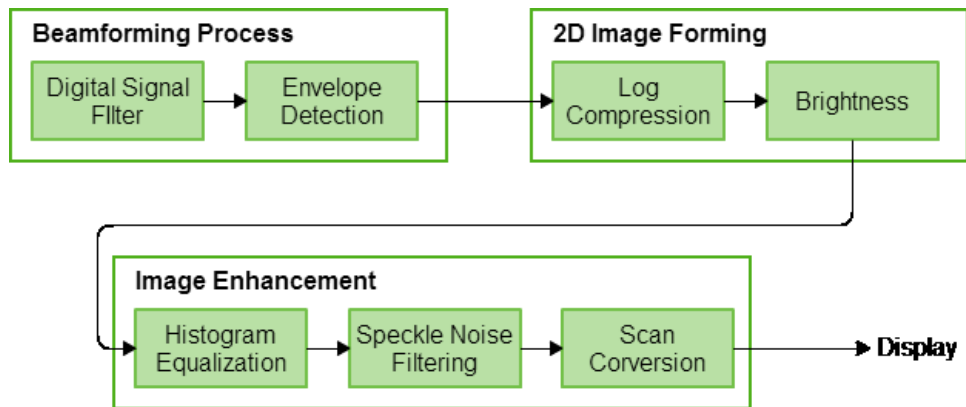


Figure 1.18: Block diagram showing the B-mode image formation and pre-display processing.

There are many different ways a ultrasound probe can make observations. These methods are called “modes”. Several modes ultrasound employs are utilized in medical imaging [44], including the A-, B-, C-, and M-modes, in addition to Doppler mode, pulse inversion mode, and harmonic mode. Since this thesis work covers B-mode imaging, we discuss only this mode here. In the B-mode (or, brightness mode) ultrasound, a linear array of transducers simultaneously scans a plane through the body that can be viewed on a screen as a two-dimensional image. More commonly known as 2D mode now. We show a block diagram that illustrates the basic B-mode image formation as well as pre-display image processing procedures in Fig. 1.18.

After beamforming the ultrasound radio-frequency (RF) signals are digitally filtered to remove the high-frequency noise resulting from the digital instruments. Then, the Hilbert transform is used [45] to detect the envelope from the RF signal. Since the envelope signal may contain very sporadic higher intensity points, it is subsequently log-compressed to decrease the dynamic range of the image. This in turn improves the visualization and quantification of the anatomical structures in the image [29]. It is further processed by histogram equalization and/or speckle reduction procedures. The B-mode ultrasound images usually have a grainy look, unique to ultrasound images. The grainy pattern arises from the multiple scattering of the waves originating in the scatterers in the tissue and their constructive-destructive interference. These grains are called “speckles” in the jargon of the field. To enhance the quality of the B-mode images, image processing algorithms are used to reduce the number of speckles. The last and very important stage of B-mode image formation is scan conversion. From a clinical perspective, it is very important that the geometry of the B-mode image show the exact geometry of the tissue being imaged. Since an image does not take into account the geometry of the transducer or the manner in which the RF data was acquired, the generated image, although containing information about the structure of the tissue in question, is not geometrically correct. Scan conversion is the process by which the data is mapped to the actual geometry of the tissue.



## 1.4 Challenges in Ultrasound Image Interpretation

The manual and automatic interpretation of an ultrasound image may be challenged by the number of artifacts present in image. Artifacts are errors in the images. They are normally caused by physical processes that affect the ultrasound beam and that in some way alter the basic assumptions the operator makes about the beam. To understand artifacts, we need to consider the basic assumptions that are made in producing an ultrasound image:

1. Sound waves travel in straight lines.
2. Reflections are transmitted from structures along the central axis of the beam.
3. The intensity of a reflection corresponds to the reflector's scattering strength.
4. Sound travels at a constant speed of 1540m/sec.
5. Sound travels directly to the reflector and back.

These assumptions do not always hold true. There are numerous cases involving exceptions to these assumptions. Although some of these artifacts may actually provide useful information or allow for novel interpretations, the majority are potential pitfalls that may result in confusion in the manual and automatic interpretation of the data. Since this thesis work focuses on bone imaging, we only discuss some major artifacts that are usually encountered in association with well-known speckle noise during ultrasound bone scanning. However, prior to that discussion, we show a schematic image showing different tissue layers in a bony anatomy in Fig. 1.19. Bone is the strongest reflector of US pulses among various tissue types through which US pulses usually propagate. A typical bone segmentation algorithm for US images targets to catch the US echo of higher intensity resulting from the periosteum-bone layer. Thus, a segmented bone surface actually represents the outer surface of the bone, right below the periosteum layer.

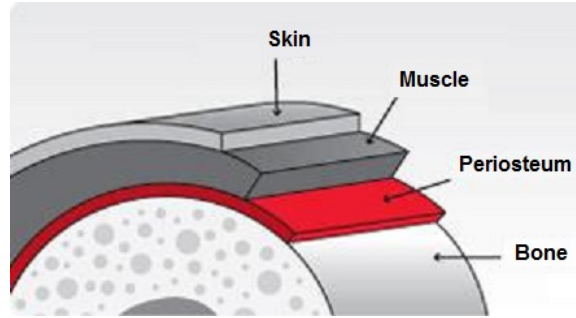


Figure 1.19: Schematic image showing different tissue layers in a bony anatomy [22].

### 1.4.1 Speckle Noise

Speckle is a granular “noise” that inherently exists in and degrades the quality of medical ultrasound images. The natural tissue surfaces are extremely rough on the wavelength scale. Images obtained from these surfaces by coherent imaging systems such as ultrasound suffer from a common phenomena called speckle. Speckle is primarily due to the interference of the returning wave at the transducer aperture. The origin of this noise is seen if we model our reflectivity function as an array of scatterers. Because of the finite resolution, at any given time, we are receiving from a distribution of scatterers within the resolution cell. These scattered signals add coherently; that is, they add constructively and destructively depending on the relative phases of each scattered waveform. Speckle noise results from these patterns of constructive and destructive interference, shown as bright and dark dots in the image. All the ultrasound images in Figs. 1.20(a)-(c) and 1.21(b), (c) contain common speckle noise with other specific types of artifacts.

### 1.4.2 Reverberation

Reverberation is an artifact that appears as multiple, equally spaced lines distributed along a scan-line. Reverberation is caused by the sound bouncing back and forth between tissue boundaries and then returning to the receiver. A B-mode image of a human ilium scan with associated reverberation artifacts is shown in Fig 1.20(a).

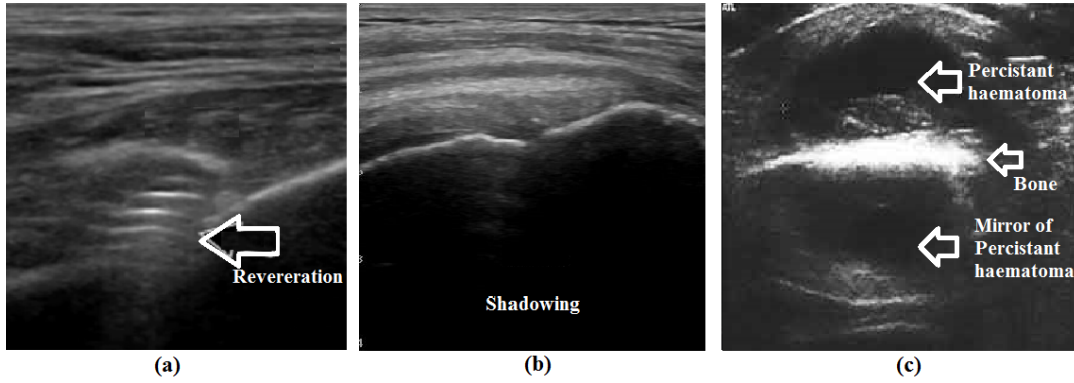


Figure 1.20: (a) The reverberation artifact in a human ilium scan [23], (b) the shadowing artifact in a human shoulder scan [24], and (c) the Mirror image artefact. Persistent haematoma lesion anterior to the tibia also appears deep to the surface of the tibia [25].

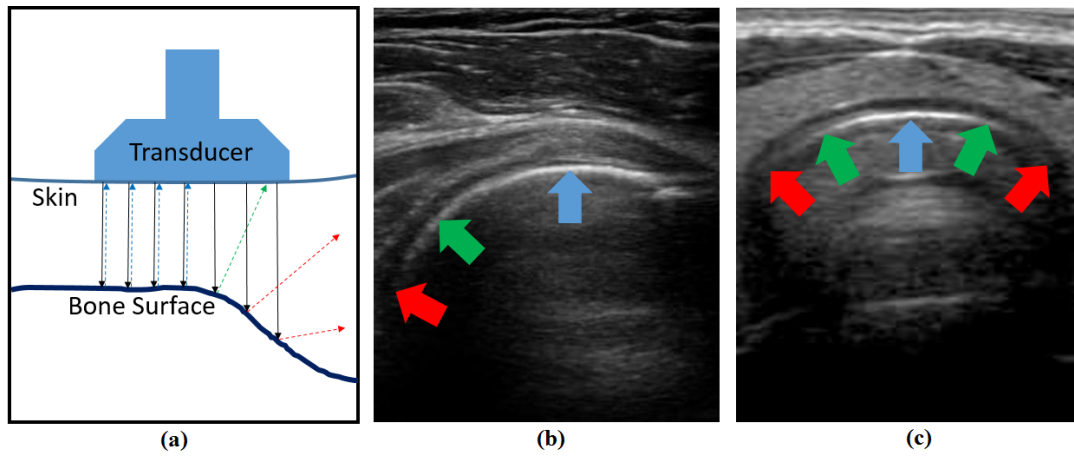


Figure 1.21: Illustration of the anisotropy artifacts in the ultrasound bone scanning. (a) A schematic diagram showing the causes of the anisotropy artifact. If the bone surface is parallel to the transducer face, then most of the echo power reflects back to the transducer (blue dotted-arrows), if the bone surface is partially ( $< 45^\circ$ ) inclined to the transducer face, then a partial echo power reflects back to the transducer (green dotted-arrows), and if the bone surface is almost perpendicular ( $> 45^\circ$ ) to the transducer face, then almost no echo power reflects back to the transducer (red dotted-arrows). (b) and (c) show two clinical example images [26] showing anisotropy artifacts. Blue, green and red arrows correspond to regions that reflects full, partial and almost no echo power from the bone surface to the transducer, respectively.

### 1.4.3 Attenuation/Shadowing

Tissues deeper than strongly attenuating objects, such as bone or calcification, appear darker since most of the beam power reflects back from the hard surface, resulting in a lower intensity of the reflected beam beneath the surface of the object. In the scan of the human shoulder in Fig. 1.20(b), the bottom side shows decreased beam intensity because of attenuation in the bone surface.

### 1.4.4 Mirror Images

Sound can bounce off a strong, smooth reflector such as a tendon. The surface acts as a mirror and reflects the pulse to another tissue interface. The ultrasound system believes the second interface is beyond the first surface, and this is where it appears on the scan. In Fig. 1.20(c), a B-mode image of a human tibia with a persistent haematoma lesion is shown with associated mirror artifacts.

### 1.4.5 Anisotropy

Anisotropy is a well-known property in medical ultrasound imaging describing a different resulting echogenicity of tissues, such as tendons, when the angle of the transducer is changed. Tendon fibers appear hyperechoic (bright) when the transducer face is parallel with the tendon, but can appear hypoechoic (darker) when the transducer face is close to perpendicular. This can be a source of interpretation error for inexperienced practitioners. Two clinical sample images, showing anisotropy artifacts, are shown in Figs. 1.21(b) and (c). Blue, green and red arrows correspond to regions that reflect full, partial and almost nonexistent echo power from the bone surface to the transducer, respectively.

## 1.5 Ultrasound-based CAOS Systems

Navigation systems in orthopaedic surgical procedures remain reliant on intra-operative fluoroscopy for the localizing of bone fragments and the guidance of surgical tools because of their relatively clear depiction of bone surfaces, fractures, implants and surgical tools [46]. However, with such 2D projection imag-

ing, surgeons typically encounter considerable difficulties in accurately localizing bone fragments in 3D space, and in assessing the adequacy and accuracy of reduced fractures. Some sample images employing 2D fluoroscopy are shown in Fig. 1.22. Surgical procedures in this case are thus highly dependent on the ex-

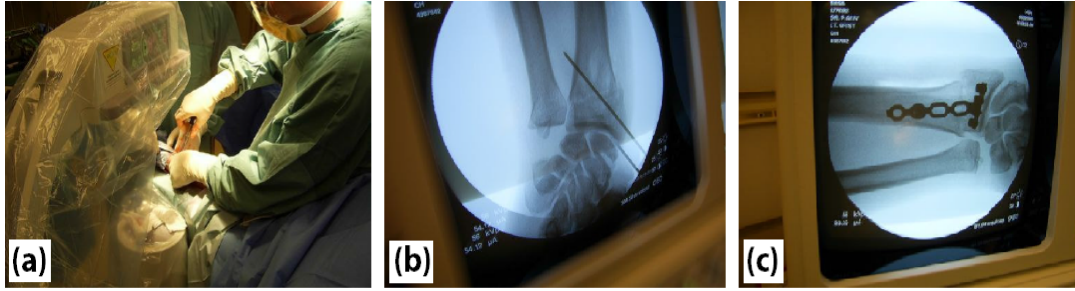


Figure 1.22: (a) Intra-operative 2D C-arm fluoroscopy, (b) 2D fluoroscopy scan showing the fractured distal radius and inserted K-wire, (c) 2D fluoroscopy scan showing the fractured distal radius and metal T-plate used during the surgery. The images are taken during a distal radius surgery at the Vancouver General Hospital (VGH), Vancouver, BC, Canada

perience of the surgeon and are prone to trial and error. Recently introduced 3D fluoroscopy [47, 48, 49] provides 3D information about the anatomical area but is nearly twice as expensive as conventional 2D fluoroscopy. Also, in extremely obese individuals, image quality can be suboptimal for navigation purposes. Furthermore the accuracy of 3D fluoroscopy depends on the rigid relationship between the reference arc and the navigated anatomy. Current radiopaque retractors must be removed before image acquisition. Replacing the retractor could affect the accuracy of the navigation system [50]. Nonetheless, a recent study [51] reports the 92% accuracy of 6,617 screws insertions in 1,105 patients in a fluoroscopy guided surgery procedure. However, fluoroscopy involves significant radiation exposure which is potentially harmful to both patients and surgical teams, with the latter enduring repeated exposure on a regular basis. We present an isodose curve showing the radiation pattern for a mobile C-arm fluoroscopy system in Fig. 1.23. Here we see that a significant amount of radiation exposure is present at around a 100cm distance from a fluoroscopic X-ray tube, within the range of which, surgical staff usually work.

Recently, ultrasound (US) has been proposed as a safer, more promising alternative [52, 53, 54, 55], and has been shown to be very effective in intra-operative

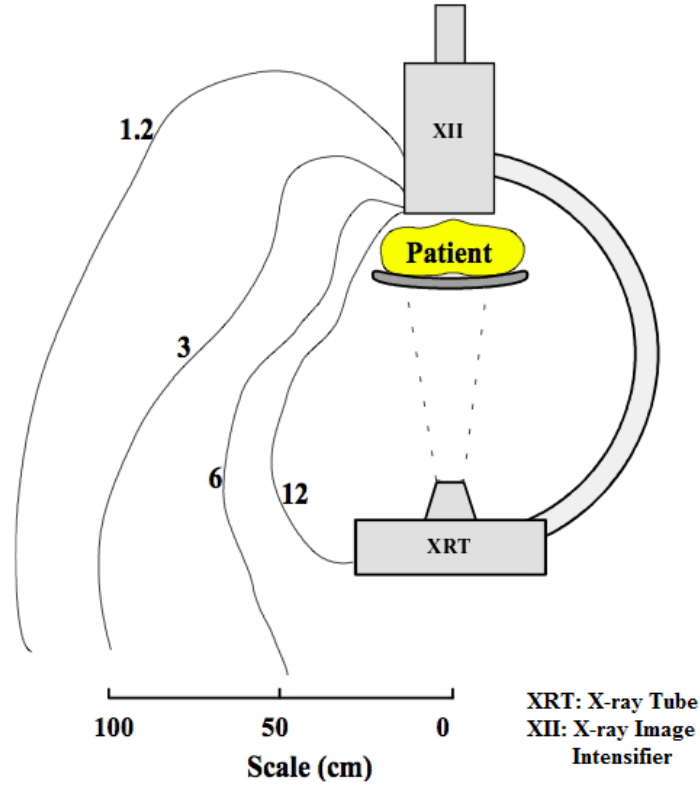


Figure 1.23: Typical isodose curves (in  $\mu\text{Gy}/\text{min}$ ) for a mobile C-arm fluoroscopy system [27].

navigation. However, US can be used in two ways:

1. Using US only intra-operatively for navigation procedures, or along with fluoroscopy, which reduces the use of the fluoroscopy, thus reducing the radiation exposure.
2. Using US pre-operatively in diagnosis and surgical planning, and intra-operatively for navigation alone, such that there is no radiation exposure.

To use US for surgical tool navigation procedures, intra-operative bone segmentation in US images needs to be (a) automatic, (b) accurate, and (c) fast. However, as we have already discussed in the previous section, US is notorious for being a very noisy modality that is comparatively difficult to interpret, as well as being more suitable for the imaging of soft tissue interfaces. Hence, the method cannot

so reliably interpret data from such hard tissue localities as bone surfaces. Recent works on using phase-based features for US bone segmentations [56,57,58,59] have been most promising to date but, nonetheless, remain somewhat conducive to false positives where soft tissue interfaces can generate phase-based responses that are extremely similar to those at bone surfaces and can thus be misclassified [29].

## 1.6 Current Ultrasound-based Bone Segmentation Methods

### 1.6.1 B-mode Imaging-based Methods

Throughout the last two decades, a number of manual, semi-automatic and automatic methods for bone segmentation in US have been developed based on B-mode image information. These methods can be sub-categorized as image intensity and local gradient-based, *a-priori*-bone-appearance-based, active-shape-based, and image-phase-feature-based methods. In this section, we provide a brief overview on some of these methods, their achievement, and limitations.

#### 1.6.1.1 Image Intensity-based Manual Methods

In the late 1990s and early 2000s, manual identification was the most common image intensity-based approach for identifying bone surface points from US data. Tonetti et al. [60] manually selected bone contour points from B-mode images in a percutaneous iliosacral-screwing surgery which achieved sufficient accuracy for the placement of screws in a clinical validation procedure. The degree of overall error resulting from the calibration, segmentation and registration was 2.57mm. Nevertheless, the manual segmentation was excessively time-consuming, resulting in an overall surgery time of  $\sim 50$ min. In a human cadaver study, Barratt et al. [61], manually segmented pelvis and femur bone surfaces from B-mode images and registered them to corresponding CT data sets, where they reported an average root mean square (RMS) target registration error of 1.6mm. Here also, the manual segmentation process was excessively time-consuming, resulting in

an overall surgery time of  $\sim 90$ min. Beek et al. [62, 63] also employed manual bone segmentation and, in one of their studies [63], used 5 manually selected seed pixels from the B-mode image of a scaphoid phantom bone to obtain a point cloud which was then used during the registration algorithm. The reported CT to US registration error was 0.54mm (max error: 0.68mm; standard deviation: 0.07mm). However, the authors noted their segmentation non-real-time as being  $\sim 3$ min. Therefore, despite manual segmentation approaches obtaining a sub-millimetric accuracy, a major limitation of these methods was the time required for manual segmentation.

#### 1.6.1.2 Image Intensity-based Automatic Methods

A number of groups attempted to automate the US image segmentation process for various applications [64]. Several traditional automatic methods used ultrasound image intensity and local gradient information for bone segmentation [65, 66, 67]. Kowal et al. [66] used depth weighted thresholding, followed by morphological operations and connected component labeling, in their bone segmentation framework. Validation on the porcine and bovine specimens revealed a mean accuracy of 0.42mm and a 0.8s average processing time. However, the authors of this article used very well-chosen US image sets that had more prominent bone intensities than those of the soft tissue regions. Thus, a simple B-mode image thresholding operation was able to extract the bone surface. However, the robustness of their method was not tested on challenging clinical image sets where reverberation and anisotropy artifacts are prominent. Daanen et al. [65] developed an automatic segmentation method for the delineation of bone in US images. Validation on clinical patient data shows a maximum mean error of 8.8 pixels and a minimum mean error of 4.545 pixels, with a pixel size of  $0.112\text{mm} \times 0.109\text{mm}$ . The time required to delineate one image was reported to be less than 4s, and a dataset of 69 images took them about 4 minutes to perform. However, it remains difficult to manage the sensitivity of intensity and gradient-based techniques to US artifacts, machine settings and algorithm parameters [33].

Few dynamic programming-based automatic bone segmentation methods are also reported in the literature [68, 69]. Still the bone detection accuracy is shown to be approximately 3mm with respect to the expert delineated bone surfaces. In



addition, these methods are also reported to be time inefficient, e.g., the method of [69] which is implemented in C++ requires  $\sim 5$ mins to extract 3D bone surfaces in a US volume of size  $200 \times 100 \times 100$  voxels.

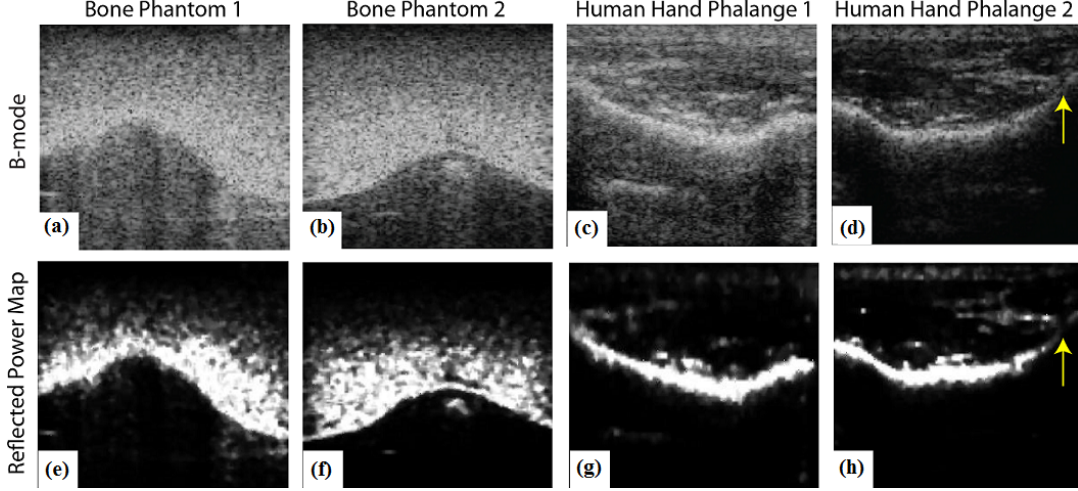


Figure 1.24: Illustration of the 2D bone segmentation performance of the reflected power imaging-based method developed by Xu et al. [28] using the bone phantom and *in vivo* data. (a)-(d) are the B-mode images, and (e)-(h) are the reflected power images.

Wen et al. [28] developed a reflected-power-imaging-based bone surface visualization approach for 2D ultrasound images. Their qualitative results on a physical bone phantom and human hand phalange are illustrated in Fig. 1.24. The reflected-power-imaging-based method depicts a band of region where the bone surface might be found but does not specify any contour for the actual bone (see Figs. 1.24(e)-(h)). Therefore, this method can be used to generate a probabilistic bone region but is not suitable for specific bone contour localization. In addition, since reflected power imaging depends on the image intensity, this approach is prone to signal dropout in places where bone intensity is not much more prominent than that of the soft tissue region. This scenario occurs where the bone surface is not perpendicular to the ultrasound beam's direction. A similar example is shown with yellow arrows in Figs. 1.24(d) and (h). Furthermore, Xu et al. [28] did not include any quantitative validation of their methods.

#### 1.6.1.3 *A-priori*-Bone-Appearance-based Methods

In order to render the problems of image intensity-based method more tractable, some researchers have attempted to incorporate a priori bone appearance information into their frameworks [65,68,70]. Note that we are considering probabilistic bone appearance- [70] and active-shape-based [71] methods as *a-priori*-bone-appearance-based methods. These methods mathematically model the bone surface region. Combining such models with intensity and gradient information gave promising results. Daneen et al. [65] reported a maximum mean bone localization error of 8.8 pixels (i.e., 0.8mm). However, fractured bone surfaces in orthopaedic surgery applications, as well as reduced bones secured with internal fixation devices, do not have continuously smooth surfaces and often significantly violate prior assumptions regarding bone shape. Methods [71,72] using the active shape models also make a priori assumptions of the targeted bone structures, which also fail for fractured bones. Building reasonable models of all possible fracture scenarios into the system is not practical. Furthermore, methods using the evolving contour (i.e., active shape) encounter difficulties near the fractured regions where they begin to “leak” into the soft tissue regions. In addition, intensity-based as well as active-shape-based bone segmentation methods were prone to a high level of speckle noise, reverberation, anisotropy, and signal dropout [59,73].

#### 1.6.1.4 Multi-modal Registration-based Methods

Some research groups developed alternate methods by combining segmentation techniques with the multi-modal registration of US to CT images [53,54,74,75]. Amin et al. [54] combined information from three perspectives: ultrasound bone intensity, shadowing beneath the bone surface, and a spatial prior obtained by processing a CT volume. Rather than explicitly segmenting the bone surface from the US image, these three sources of information were used to obtain an idea of regions which are likely to contain bone surfaces. During the registration process, the regions were refined to select data based on its consistency with the 3D shape of the bone. The overall accuracy of the system is directly related to the accuracy of the initial registration estimate which also depends on the experience of the surgeon and the quality of the image. However, they failed to

report any accuracy results, but, rather, reported a registration error of 1.94mm for average translations and of  $0.90^\circ$  for average rotations. Brendel et al. [74] first segmented 3D bone surfaces from a CT image. Then, a part of the bone surface, which should be visible in the CT image, was segmented from the US data. The segmented bone surface in the CT image was subsequently registered to the US image, which resulted in 0.5mm of surface fitting error. Ionescu et al. [75] employed a similar approach; the main difference was that they also segmented the US images using classical image segmentation techniques based mainly on linear filtering or mathematical morphology. This segmentation was then updated using US-CT registration and a reported registration error of 2mm for average translation and  $2^\circ$  for the average rotations.

#### 1.6.1.5 Image-phase-feature-based Methods

In the last decade, Hacıhaliloglu et al. [33,73,59,56,57,76,77] used a log-Gabor filtering based ridge detection approach to delineate bone in 2D and 3D US images, while reporting the achievement of sub-millimetric accuracy in bone localizations (with a mean absolute error  $<1\text{mm}$ ) on their *in vivo* data. These methods exploit the phase congruency features present in an ultrasound image. The underlying principle is that phase is constant and congruent across all the scales at the location of which the human visual system would be perceived locally as a one-dimensional feature such as an edge. It has been demonstrated [76] that phase information can provide more significant information within an image than amplitude information; therefore, the human brain can perceive more enhanced features in phase space. Phase congruency [78] permits feature detections independent of the actual feature type. However, these image-local-phase-feature-based bone segmentation methods use pre-determined (manually or data-driven) angular orientations of bone in the corresponding US images along which log-Gabor filtering is performed. Since soft tissue interfaces near the transducer face shows similar intensity profiles as well as the fact that they lie along similar angular orientations to those of the bone contour, log-Gabor filtering eventually produces confounding phase-symmetry profiles for both the bone and soft-tissue interfaces that sometimes cause confusion when deciding on the actual bone contour. The authors further attempted to address this issue by adopting bottom-up ray cast-

ing and image cropping, which, however, may not have been a reliable approach for use in a critical surgery environment. In addition, phase-based methods may also fail to extract bone boundaries in places where B-mode intensities are not prominent with respect to the background. These limitations are demonstrated in Fig. 1.25. We show the presence of such false positives (shown with yellow arrows) as well as the discontinuity in the bone boundaries (shown with white arrows) in Figs. 1.25(e)-(h).

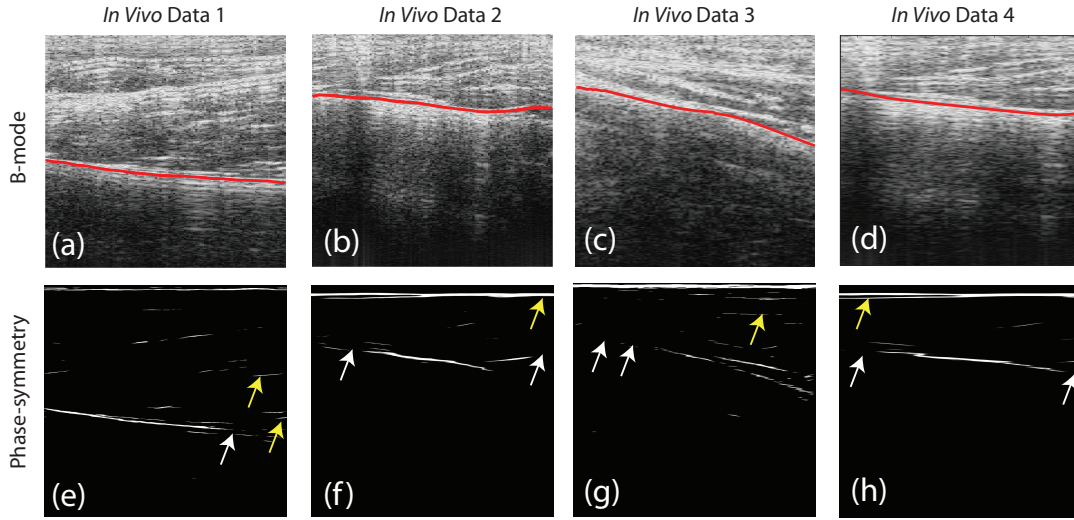


Figure 1.25: Illustration of the presence of false positives as well as the false bone discontinuity in the estimated phase symmetry images using the *in vivo* data. (a)-(d) are the B-mode images with expert delineated bone boundaries overlaid. (e)-(h) are the phase symmetry images correspond to images shown in (a)-(d), respectively. The false positive intensities are shown with yellow arrows while false bone discontinuities are shown with white arrows.

#### 1.6.1.6 Discussion

From this brief discussion on the B-mode imaging-based bone segmentation methods, we can conclude that, although the manual segmentation methods achieved better bone localization accuracy, they were too time-consuming to be widely utilized in the OR. On the other hand, image-intensity-based automatic methods are prone to displaying image artifacts (e.g., reverberation, anisotropy and signal dropout/shadowing), machine settings and algorithm parameters. Some automatic intensity-based methods, i.e., dynamic programming-based methods,

though, achieved moderate accuracy in bone localizations but at the cost of requiring very high computation time. *A-priori*-bone-appearance-based segmentation methods showed promise in bone localizations, but failed to predict the shape of the fractured bones. A few multi-modal registration-based methods for bone segmentation are also reported, but nonetheless depend on ultrasound image intensity information, which is prone to displaying image artifacts similar to those of the image-intensity-based methods. Image-phase-feature-based bone segmentation methods addressed the limitations of the previous methods and achieved sub-millimetric accuracy in bone localization. These methods are also based on the B-mode imaging. However, as we already have shown in Fig. 1.25, false positive bone responses are produced by these methods at the soft tissue interfaces which sometimes result in confusion in the equipment’s determining the actual bone contour. In addition, the automatic 3D-phase-feature-based method [59] is found to be time inefficient (at  $\sim 2$ mins), although a graphics-processing-unit (GPU)-based implementation of a version of this method, which requires manual selection of all the parameters, takes 0.8s for its execution [79]. Therefore, our thesis has focused on developing an effective method for performing bone segmentations (i.e., an elastography/strain imaging-based method) that would exploit the inherent bone localizing information which is not usually revealed in the typical B-mode images and, thus, is not susceptible to the development of image artifacts. In addition, this thesis focuses on developing real-time or near-real-time bone segmentation methods.

### 1.6.2 Strain-imaging-based Methods

Elastography (strain imaging) is an emerging medical diagnostic tool for capturing the mechanical properties (e.g. stiffness) of biological tissue [45, 80, 81, 82, 83]. Elastography has shown promise in the detection of breast and prostate tumours [45], liver cirrhosis [80], vascular plaques [83], and ligament-bone insertions [84]. Because bones are much stiffer than the surrounding tissue, strain imaging is a good candidate for bone surface visualization. However, the only method that investigated the potential of using elastography in 2D bone segmentation in US prior to us was that of Xu et al. [28], who investigated a strain-

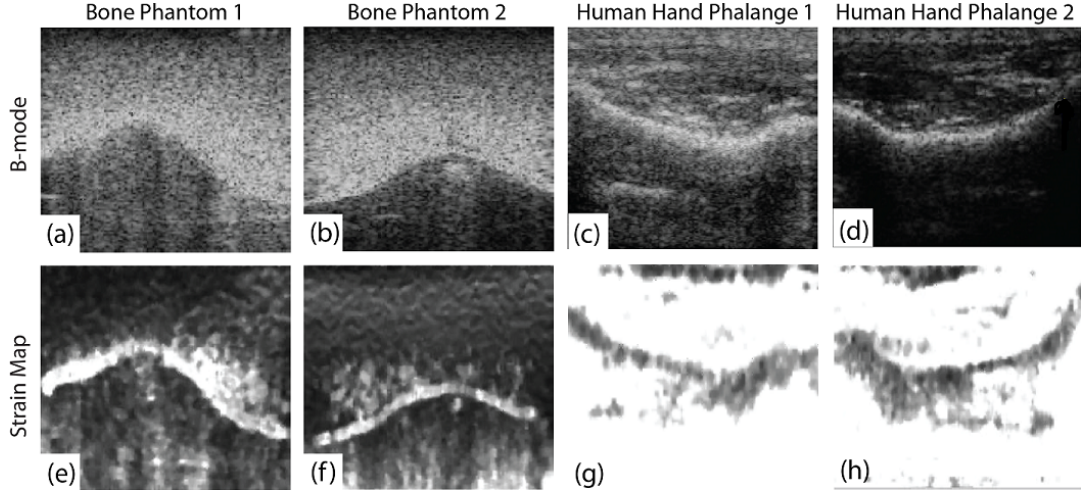


Figure 1.26: Illustration of the 2D bone segmentation performance of methods developed by Xu et al. [28] using the bone phantom and *in vivo* data. (a)-(d) are the B-mode images, and (e)-(h) are the strain images.

imaging-based technique in [28] for bone surface visualization in 2D ultrasound images. Their qualitative results on a physical bone phantom and human hand phalange are shown in Fig. 1.26. Their strain-imaging-based bone detection results revealed a low degree of contrast in human data between the hard bone and soft tissue regions (see Figs. 1.26(g) and (h)), although it exhibited some bone outlines of bones in the phantom images (see Figs. 1.26(e) and (f)). Based on the results of this method, a region can be predicted where the bone surface can be found but where no contour for the actual bone can be specified. The exact bone extraction process from these fuzzy strain images is not further mentioned in the article. A quantitative validation of this method is also not reported. Moreover, problems arose from signal windowing as window-based elastography methods (as used by Xu et al. [28]) have limitations associated with the size of the window segments. A significant amount of noise in the strain image can easily be introduced with the choice of smaller window sizes and/or large overlap between successive windows [83]. In addition, in the window-based methods, the estimated strain for a particular window is considered to correspond to the centre of the window. This might result in a bone localization error of  $\frac{1}{2} \times \text{window length}$  ( $>1\text{mm}$ ), which is larger than that of our target (sub-millimetric) accuracy.

## 1.7 Thesis Objectives

The context of this thesis work was ‘US guided navigation in CAOS’, which requires robust, accurate and rapid bone segmentation in US images. Although diverse, previously reported methods achieved satisfactory accuracy, they often failed to vigorously extract bone surfaces due to the presence of various types of image-intensity-based artifacts. Therefore, the objective of this thesis work was to develop more robust, accurate and automatic bone segmentation techniques for ultrasound images than found in the state-of-the-art methods. This research was intended to further advance the larger goal of developing a novel 3D ultrasound-based CAOS system. The goals of this thesis include the following:

- Developing new image processing methods for automatically extracting bone surfaces from 2D and 3D ultrasound images that are substantially more robust to false positives than current phase symmetry methods.
- Demonstrating comparable or better accuracy in bone localization on *in vivo* data than found in the state-of-the-art methods.
- Maintaining or reducing the computation time required for state-of-the-art methods.

We believe that the outcomes of this thesis work would (a) improve the performance of the ultrasound guided navigation procedure by providing better assessments and placements of the bone location, which might in turn decrease surgery time; (b) decrease the amount of radiation exposure to patients and/or staff during orthopedic surgeries; (c) promote minimally invasive surgery (MIS) by minimizing the extent of soft tissue incisions; and (d) decrease the cost and improve the quality of health care by replacing fluoroscopy at key points in orthopedic diagnoses and treatments.

## 1.8 Thesis Organization

This thesis is separated into three parts. In Chapter 2, we present our preliminary work [29], where we investigate the potential of combined US strain imaging and

envelope power signaling to delineate bone boundaries in US images. Our method uses real-time strain imaging [82] based on an analytic minimization of regularized cost functions to delineate bone from the tissue stiffness map and, consequently, we have achieved a marked reduction in false positive bone responses at the soft tissue interfaces. However, our method relies on assumptions based on empirical observations.

In Chapter 3, we present our subsequent study in which we mitigate the limitations of this preliminary work presented in Chapter 2 by introducing automatic parameter selection processes that replace all of the intuitive assumptions and thus, make the method more robust and self-tuning. We improve the method in [29] by incorporating the depth-dependent cumulative power of the envelope into the pre- and post-compression data, which we demonstrate as reducing the soft-tissue-related artifacts in the resulting strain images. We further improve the method by incorporating a data driven weight into the technique, estimated from the echo de-correlation measurements performed between the pre- and post-compression RF frames, and which controls the contribution of the strain image into the resulting fused map. We also use a local statistics-based bone discontinuity detection scheme. Finally, we introduce Gaussian mixture regression, a more flexible multivariate non-parametric regression model that better preserves the curvature features in the bone boundary than the linear regression model employed in our preliminary work.

Although our studies presented in Chapters 2 and 3 show great promise, they are limited only to 2D US images, while a near-real time 3D elastography technique using a 3D probe has been presented that can generate a 3D strain image [81]; this technique has not been validated on clinical *in vivo* data, and we have found it to be very sensitive to echo de-correlations while acquiring a post-compression US volume which limits its applicability. Therefore, in Chapter 4, we present our simple yet effective technique to a 3D bone surface extraction, using a surface-growing approach that is seeded from 2D bone contours estimated from combined ultrasound strain imaging and envelope power. The 2D seed bone contour grows into the 3D surface by minimizing a combined intensity similarity and a voxel proximity-based cost function.

The performance of these algorithms is evaluated using finite-element-model



(FEM) simulation phantoms and, experimental phantoms, as well as *in vivo* data, and compared with two state-of-the-art image-phase-features-based bone boundary estimation algorithms.

## Chapter 2

# Bone Detection in Ultrasound Using Combined Strain-imaging and Envelope Power

In this chapter, we discuss our preliminary approach of bone segmentation by combining US strain-imaging and envelope power detection at each RF sample. Our method uses real-time strain-imaging [82] based on an analytic minimization of regularized cost functions to delineate bone from the tissue stiffness map and thus, we achieved a marked reduction of the false positive bone responses at the soft tissue interfaces.

### 2.1 Ultrasound Signal Model

The one-dimensional (1D) time domain models of the back-scattered ultrasound RF signals before and after compression can be written as [83]

$$I_1(t) = s(t) * p(t) + \nu_1(t), \quad (2.1)$$

$$I_2(t) = s\left(\frac{t}{\epsilon} - t_0\right) * p(t) + \nu_2(t), \quad (2.2)$$

where  $I_1(t)$  and  $I_2(t)$  denote the pre- and post-compression RF echo signals, respectively,  $s(t)$  denotes the 1D US scattering function,  $p(t)$  denotes the point spread function,  $\epsilon$  denotes the compression factor caused by mechanical deforming

pressure to the medium,  $\nu_1(t)$  and  $\nu_2(t)$  are the uncorrelated random noise profiles and  $*$  sign is used to denote the convolution operation. The post-compression RF echo is assumed to be the scaled and shifted replica of the pre-compression RF echo in the absence of noise. According to [45], the strain  $\mathbf{S}$  is related to the compression factor  $1/\epsilon$  as  $\mathbf{S} = 1 - \epsilon$  where  $\epsilon \leq 1$  and  $\mathbf{S} \ll 1$ .

## 2.2 Modified Strain Map (MSM)

The analytic minimization (AM)-based strain estimation method has been described in detail in [82]. In this section, we provide a brief overview of this method.

### 2.2.1 Displacement Estimation

#### 2.2.1.1 Cost Formation

To estimate tissue displacement from the pre- and post-compression RF echo frames  $I_1$  and  $I_2$ , respectively, of size  $m \times n$  (considering in the discrete domain), the integer axial and lateral displacements of a seed scan-line are estimated using dynamic programming [85]. Using these estimates as a priori information, displacements for all other scan-lines are estimated in the sub-sample level using the regularized cost function as

$$\begin{aligned}
C_j(\Delta a_1, \dots, \Delta a_m, \Delta l_1, \dots, \Delta l_m) = & \sum_{i=1}^m \{ [I_1(i, j) - I_2(i + a_i + \Delta a_i, j + l_i + \Delta l_i)]^2 \\
& + \alpha(a_i + \Delta a_i - a_{i-1} + \Delta a_{i-1})^2 + \beta_a(l_i + \Delta l_i - l_{i-1} + \Delta l_{i-1})^2 \\
& + \beta'_l(l_i + \Delta l_i - l_{i,j-1})^2 \}, \tag{2.3}
\end{aligned}$$

where  $\alpha$ ,  $\beta_a$  and  $\beta'_l$  are the tuneable parameters,  $a_i$  and  $\Delta a_i$  are the integer and sub-sample axial displacements, respectively, and  $l_i$  and  $\Delta l_i$  are the integer and sub-sample lateral displacements, respectively, of the  $i$ th sample in the  $j$ th scan-line. Now the post-compression data term in Eqn. (2.3) can be written in the 2D Taylor expansion around  $(i + a_i, j + l_i)$  as

$$\begin{aligned}
& I_2(i + a_i + \Delta a_i, j + l_i + \Delta l_i) \\
& \approx I_2(i + a_i, j + l_i) + \Delta a_i I'_{2,a} + \Delta l_i I'_{2,l}, \tag{2.4}
\end{aligned}$$

where  $I'_{2,a}$  and  $I'_{2,l}$  are the derivatives of the  $I_2$  in the axial and lateral directions, respectively.

### 2.2.1.2 Cost Optimization

Now the optimal solution for  $(\Delta a_i, \Delta l_i)$  can be estimated from Eqns. (2.3) and (2.4) by setting  $(\partial C_j)/(\partial \Delta a_i) = 0$  and  $(\partial C_j)/(\partial \Delta l_i) = 0$  for  $i = 1 \dots m$ . If  $\Delta \mathbf{d} = [\Delta a_1 \Delta l_1 \Delta a_2 \Delta l_2 \dots \Delta a_m \Delta l_m]^T$  and initial estimates  $\mathbf{d} = [a_1 l_1 a_2 l_2 \dots a_m l_m]^T$ , then after partial differentiating Eqn. (2.3) and equalize it to zero, it can be written as

$$(\mathcal{I}_2'^2 + \mathcal{D}_1 + \mathcal{D}_2)\Delta \mathbf{d} = \mathcal{I}_2' \mathbf{e} - \mathcal{D}_1 \mathbf{d}, \quad (2.5)$$

$$\mathcal{D}_1 = \begin{bmatrix} \alpha & 0 & -\alpha & 0 & 0 & 0 & \dots & 0 \\ 0 & \beta_a & 0 & -\beta_a & 0 & 0 & \dots & 0 \\ -\alpha & 0 & 2\alpha & 0 & -\alpha & 0 & \dots & 0 \\ \vdots & \vdots & \vdots & \vdots & \vdots & \vdots & \vdots & \vdots \\ 0 & 0 & 0 & \dots & 0 & -\beta_a & 0 & \beta_a \end{bmatrix}$$

where  $\mathcal{D}_2 = \text{diag}(0, \beta_l', 0, \beta_l', \dots, 0, \beta_l')$  is a diagonal matrix of size  $2m \times 2m$ ,  $\mathbf{e} = [e_1 e_1 \dots e_m e_m]^T$ ,  $e_i = I_1(i, j) - I_2(i + a_i, j + l_i)$ ,  $\mathcal{I}_2'^2 = \text{diag}(\mathcal{J}'^2(1) \dots \mathcal{J}'^2(m))$  is a symmetric diagonal matrix of size  $2m \times 2m$  with

$$\mathcal{J}'^2(i) = \begin{bmatrix} I_{2,a}'^2 & I_{2,a}' I_{2,l}' \\ I_{2,a}' I_{2,l}' & I_{2,l}'^2 \end{bmatrix}$$

### 2.2.1.3 Practical Assumptions Incorporation

To cope with the practical scenarios, some assumptions are made in Eqn. (2.5):

1. The first assumption incorporates depth-dependent US attenuation,
2. The second assumption ensures very small lateral displacements (i.e. difference between consecutive lateral displacements is up to 4 scan-lines),
3. And the third assumption ensures zero displacement at the transducer face.

Moreover, for robust displacement estimates, iteratively reweighted least squares (IRLS) is used. Consequently, Eqn. (2.5) is modified along with facilitating inverse gradient estimation as

$$(\mathcal{W}\mathcal{I}_1'^2 + \mathbf{Z}\mathcal{D}_1 + \mathbf{Z}\mathcal{D}_2)\Delta\mathbf{d} = \mathcal{W}\mathcal{I}_1'\mathbf{e} - \mathbf{Z}\mathcal{D}_1\mathbf{d} + \mathbf{s}, \quad (2.6)$$

where  $\mathcal{W} = \text{diag}(0, w(r_1), w(r_1) \dots w(r_m), w(r_m))$ ,  $w(r_i) = \frac{1}{1+(r_i/T)^2}$  is the IRLS Cauchy weight,  $r_i = I_1(i, j) - [I_2(i + d_i, j + a_i) + \Delta d_i I'_{2,a} + \Delta a_i I'_{2,l}]$ ,  $T$  is a tunable threshold,  $\mathbf{s}$  is the bias vector to ensure small lateral displacements,  $\mathbf{Z} = \text{diag}(\zeta_1, \zeta_1, \dots, \zeta_m, \zeta_m)$ , and  $\zeta_i = [\exp(\frac{1540 \times 10^2 a_t f_o \log(10)}{20 f_s \times 10^6})]^{-i}$ . Here,  $a_t$  denotes the frequency dependent attenuation coefficient and is 0.6dB/cm/MHz for the soft tissue [40], and  $f_o$  and  $f_s$  are the transducer operating and sampling frequencies (in MHz), respectively. Finally, Eqn. (2.6) is solved to calculate a regularized displacement map  $\Delta\mathbf{d}$ .

### 2.2.2 Strain Estimation and Processing

A Kalman filter-based method is adopted to estimate the final strain  $\mathbf{S}$  from the estimated displacement map [82]. We use this estimated strain map  $\mathbf{S}$  as a primary indicator to know the bone boundary location and expect to see lower strain values along the bone boundary. For robust bone boundary estimation, we combine the modified strain map with the envelope power map. Therefore, to produce a strain map with a dynamic range roughly equivalent to that of the envelope power map, we estimate the MSM as

$$\text{MSM} = \frac{\hat{\mathbf{S}}}{\max[\hat{\mathbf{S}}]}, \quad (2.7)$$

where  $\hat{\mathbf{S}} = |(-\mathbf{S}) + | \text{median}(-\mathbf{S}) ||$  and  $\text{median}$  is the median operator.

## 2.3 Modified Envelope Map (MEM)

The performance of strain-imaging is prone to echo de-correlation [83]. In a clinical settings, a radiologist, inexperienced in elastography may find it hard to produce a good strain image to visualize bone. Therefore, we intend to fuse

bone appearance information from another reliable source, i.e., envelope of the RF data, into the strain image-based information. An envelope map can be generated from a single RF frame and hence it is free of echo de-correlation-based artifacts. Moreover, an envelope map has better dynamic range in terms of its intensity contents than a log-compressed envelope (i.e., B-mode) map [68]. This higher dynamic range helps better distinguishing between the intensities correspond to the bone and soft tissue regions. We further increase the dynamic range of a typical envelope map by estimating its power. However, as the strain is mapped with respect to the pre-compression RF frame, we use the same pre-compression RF frame to generate the modified envelope map (MEM) so that it can be spatially matched to the MSM. The envelope of a RF scan-line at column  $j$  is calculated as  $\mathbf{E}_j(i) = |H[I_{1,j}(i)]|$  [45], where  $H$  denotes the *Hilbert transform*. This transformation converts a periodic signal into its analytic form that contains amplitude and phase information separately. In easy words, we can get a demodulated signal (envelope) from its carrier (raw RF) after this transformation. Finally, we estimate the MEM as

$$\text{MEM} = \frac{\mathbf{E}^2}{\max[\mathbf{E}^2]}. \quad (2.8)$$

## 2.4 Fused Map Estimation

Our next step involves fusing the MSM and MEM into a single fused map (FM). We estimate FM to complement bone information from two different sources and types of information. Strain image is based on the tissue stiffness information while envelope contains the echo intensity-based information. As we already discussed that the performance of the strain-imaging is prone to echo de-correlation, envelope power map complements with the higher echo intensity information resulting from bone surface. On the other hand, we already discussed in Chapter 2 that intensity-based bone segmentation methods have limitations resulting from high levels of speckle noise, reverberation and signal drop out, therefore, strain image complements with the higher stiffness information resulting from the bone region. The FM is estimated as

$$\text{FM} = \lambda \times \text{MSM} + (1 - \lambda) \times \text{MEM}, \quad (2.9)$$

where  $\lambda$  is the weight. To choose a suitable value of  $\lambda$ , we analyse the effect of this choice on the accuracy of the bone boundary localization in a FEM-based simulation (see Section 2.6.1) of a noisy environment (i.e., 10dB signal-to-noise ratio (SNR)). For this MAE analysis, we deliberately chose SNR to be lower than the typically encountered values (approximately 18~22dB) in RF data after beamforming [86] to simulate a worse case scenario. We observe that the mean MAE is minimized for  $\lambda = 0.5$  (see Fig. 2.2(j)). While this value for  $\lambda$  may not be optimal under all possible imaging situations, the results seem to be relatively insensitive to this choice, so we opted to set  $\lambda = 0.5$  for this study.

## 2.5 Forming Bone Contour Using Regression

In the fused map, the maximum intensity points are expected to correspond to the actual bone contour since the maximum intensity points in the MSM and MEM individually are likely to represent the bone surface. Therefore, after estimating the FM, we detect the maximum intensity point along each scan-line of the FM. Then we estimate the final bone boundary using a local linear-fit over the detected maximum intensity points. The linear fit window length is chosen to be 3mm. The choice of the fitting window length is important since a small window will not adequately smooth the estimated surface while a larger window could fail to adequately represent real curvature in the bone contour. We have empirically selected a value of 3mm, as this seemed to work well with our pilot data; however, in future work, it would be desirable to determine this value using a more principled approach, whether by incorporating a priori information based on knowledge of the scan target or derived directly from the image being processed.

## 2.6 Validation Setup

### 2.6.1 Simulated Phantom

We built a 40mm×40mm finite-element-model (FEM) phantom using the ANSYS analysis software (ANSYS, Inc., Canonsburg, PA) and then generated an

ultrasound simulation of the model using Field II [87]. Our phantom mimicked an US scan of the human distal radius bone with a total number of nodes of 55,180. The stiffness of the homogeneous soft tissue and bone region were set to 10kPa and 10GPa, respectively as previously reported in the literature [88]. Our phantom was compressed from the top using a larger-width planar compressor in free-hand fashion. An ultrasonic transducer of center frequency,  $f_0 = 5\text{MHz}$  and band-width = 50% was used to simulate the phantom scan from the top. The total number of scan lines was set to 128. We set an applied pressure level that corresponds to 1% average strain. In addition, we did not model out-of-plane motion.

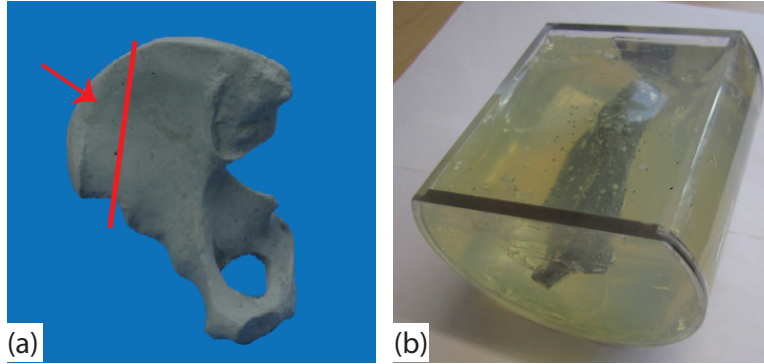


Figure 2.1: Illustration of the experimental phantom. (a) The phantom was created using a Sawbones radio-opaque hemi-pelvis, cut along red line. (b) The separated portion (shown with red arrow in (a)) of the pelvis is embedded in polyvinyl chloride (PVC) gel.

### 2.6.2 Experimental Physical Phantom

We constructed an experimental phantom using a radio-opaque Sawbones hemi-pelvis (Sawbones, Pacific Research Laboratories, Inc., Vashon Island, WA), model number 1297-22 (see Fig. 2.1). A portion of the pelvis was suspended in polyvinyl chloride (PVC) gel and placed in an acrylic tube. A high resolution peripheral quantitative computed tomography (CT) machine, model HR pQCT Xtreme CT (Scanco USA, Inc., Wayne, PA) was used to acquire a single  $482 \times 482 \times 402$  (lateral  $\times$  axial  $\times$  elevational) voxel volume. The resolution of the acquired volume was  $0.25\text{mm} \times 0.25\text{mm} \times 0.25\text{mm}$ . In addition, US was acquired using a SonixRP



(Ultrasonix Medical Corporation, Richmond, BC) scanner integrated with a L14-5W/60 probe operating at 10MHz in the Centre for Hip Health and Mobility, Vancouver, BC, Canada.

### 2.6.3 *In Vivo* Data

We acquired five sets of data from five volunteers (volunteer-I: 25-year old male; volunteer-II: 26-year old male; volunteer-III: 24-year old male, volunteer-IV: 25-year old male; volunteer-V: 33-year old male) after obtaining prior consent. All data were acquired with free-hand compression. US was acquired using a SonixRP (Ultrasonix Medical Corporation, Richmond, BC) scanner integrated with a L14-5W/60 probe operating at 10MHz in the Centre for Hip Health and Mobility, Vancouver, BC, Canada. The study was approved by the UBC clinical research ethics board.

## 2.7 Results

We provide comparative results of our proposed strain and envelope power based method (SEP) with the automatic adaptive parameterization in local phase feature-based bone segmentation in US (APS) [57] method using the FEM phantom, experimental phantom and *in vivo* data. The APS method selects parameters automatically for the Log-Gabor filters based on properties estimated directly from the specific US image that is being analyzed. We calculate mean absolute error (MAE) which is defined as

$$\text{MAE} = \frac{1}{N} \sum_{k=1}^N |A(k) - G(k)|, \quad (2.10)$$

where  $N$  is the approximated number of columns on which the bone boundary spans,  $A$  is the matrix containing the actual bone boundary points (ground truth), and  $G$  is the matrix containing the estimated bone boundary points. As ground truth, we use the estimated bone boundaries from the ideal elastogram and CT image for the FEM and experimental phantom, respectively. Note that to estimate MAE for the SEP method, we use the bone boundary points before applying the regression.

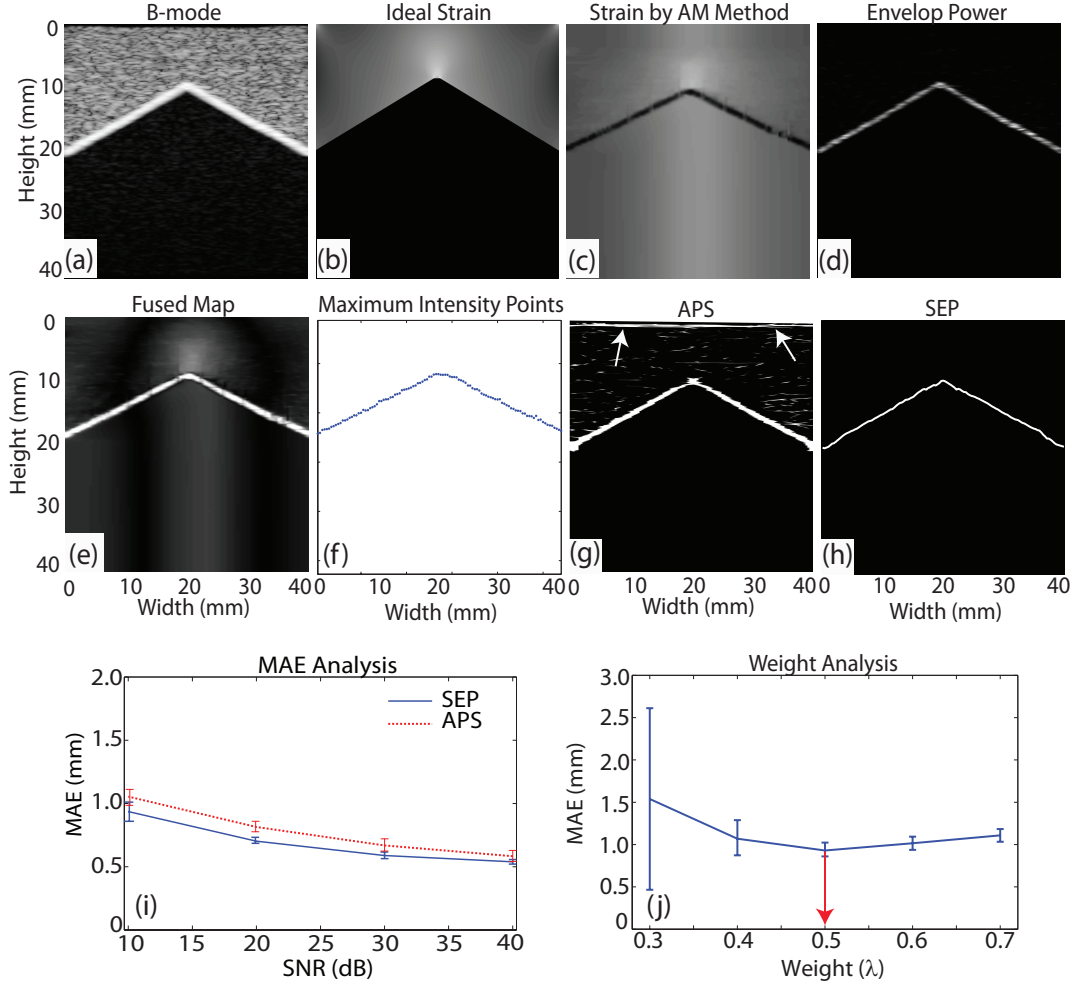


Figure 2.2: Illustration of bone boundary detection using the FEM phantom. (a) B-mode image, (b) ideal strain image, (c) strain image generated by the AM method, (d) envelop power map, (e) fused map, (f) maximum intensity points on the fused map, (g) estimated bone boundary by the APS method, (h) estimated bone boundary by the SEP method, (i) MAE analysis of the SEP and APS methods at different SNRs, and (j) weight analysis at 10dB SNR (weight at minimum error is shown with red arrow).

### 2.7.1 FEM Results

We provide comparative qualitative and quantitative results of the SEP and APS methods using the FEM data. In Figs. 2.2(a), (b), (c), (d) and (e), we show the B-mode, ideal strain, estimated strain  $\mathbf{S}$ , envelop power, and fused maps, respectively. In addition, in Fig. 2.2(f), we show the maximum intensity points on

the fused map. Note that we are dealing with anatomy that includes bone, hence, the RF intensities fall sharply (compared to soft tissue) beneath the bone surface. In such a situation, the regularization terms in the cost equation become larger than the signal part in the region beneath the bone surface and over-smoothing tends to occur [82]. In Figs. 2.2(g) and (h), we show the bone boundaries detected by the APS and SEP methods, respectively. The figures demonstrate that the APS method produces several false positive bone responses (indicated by white arrows) due to the presence of ridge-like features in the B-mode image. In contrast, the bone boundary produced by the SEP method (Fig. 2.2(h)) is apparently free of such artifacts.

We also compare the quantitative performance of the SEP and APS methods in terms of MAE in Fig. 2.2(i) with four different signal-to-noise ratio (SNR) simulations (40, 30, 20, and 10dB) with 100 realizations each. We employed mean absolute error calculations between the actual and estimated bone boundaries to show the extent of the false positives created by the comparing methods. As can be seen in this figure, up to 20dB SNR, the APS method produces greater mean MAE than that of the SEP method, though the mean MAE of both the methods are almost flat and standard deviations are close to zero. In addition, the mean MAE of the APS method at 10dB SNR is higher though the standard deviation of the SEP method in this case somewhat higher. Therefore, we can say that the SEP method shows better performance in terms of reduced false positive bone responses than that of the APS method.

## 2.7.2 Experimental Phantom Results

Figure 2.3 demonstrates the qualitative and quantitative performance comparison of the SEP and APS methods using the experimental phantom. In Fig. 2.3(a), we show the B-mode image. Figure 2.3(b) shows the CT projection slice along which the US scanning is performed and fiducials in Fig. 2.3(a) corresponds to fiducials in Fig. 2.3(b) (shown with yellow arrows) in the same order. The estimated strain image is shown in Fig. 2.3(c). We show the detected bone boundaries by the APS and SEP methods in Figs. 2.3(e) and (f), respectively. We can see from Fig. 2.3(e) that the bone boundary image estimated by the APS method produces

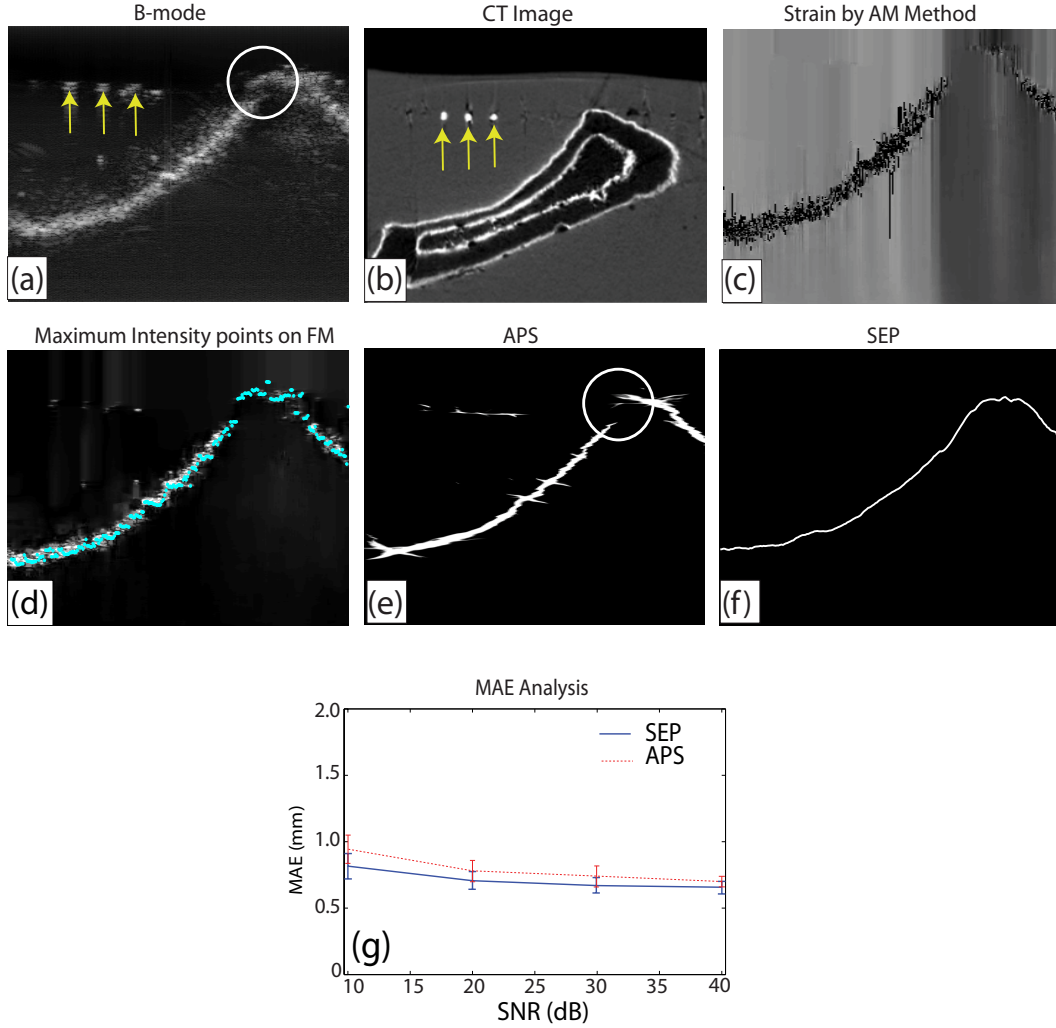


Figure 2.3: Illustration of the bone boundary detection using the experimental phantom. (a) B-mode image, (b) a CT projection along which US scanning is performed, (c) strain image, (d) maximum intensity points overlaid on the fused map, (e) estimated bone boundary by the APS method, (f) estimated bone boundary by the SEP method, and (g) MAE analysis of the SEP and APS methods at different SNRs.

false positive responses in soft tissue regions and fails to estimate bone boundary where US back-scatter response is very weak (shown with white circles in Figs. 2.3(a) and (e)). In contrast, the bone boundary estimated by the SEP method has no discontinuity as well as produces no noticeable false positive response.

We also show the quantitative performance of both the methods in Fig. 2.3(g).

Here too, we use four different SNRs (40, 30, 20, and 10dB) with 100 realizations for each of them to analyze the MAE. Since the quality of the ultrasound machine-acquired RF data is dependent on user-defined parameters, the signals may have different signal to noise ratios in different situations. Therefore, we have used a range of SNRs to evaluate the robustness of our proposed SEP scheme. We can see from this figure that the mean MAE values of the SEP method are lower than that of the APS method at all SNRs though the standard deviations of the SEP method are slightly higher. Therefore, from here too, we can say that the SEP method shows better performance in terms of reduced false positive bone responses than that of the APS method.

### **2.7.3 *In Vivo* Results**

#### **2.7.3.1 Case 1**

Figure 2.4 demonstrates the qualitative performance comparison of the SEP and APS methods using the volunteer-I data set. The scanned region, B-mode image, and strain image are shown in Figs. 2.4(a), (b), and (c), respectively. The maximum intensity points overlaid on the fused map are shown in Fig. 2.4(d). The estimated bone boundaries by the APS and SEP methods are shown in Figs. 2.4(e) and (f), respectively. We see from Fig. 2.4(e) that the APS method produced false positive response for bone in the soft tissue interfaces (shown with white arrows). In contrast, the bone boundary estimated by the SEP method is free from any false positive related artifact and better match the shapes visible in the corresponding B-mode image (see Figs. 2.4(b) and (f)).

#### **2.7.3.2 Case 2**

We show the qualitative performance comparison of the SEP and APS methods using the volunteer-II data set in Fig. 2.5. The scanned region, B-mode image, and strain image are shown in Figs. 2.5(a), (b), and (c), respectively. The maximum intensity points overlaid on the fused map are shown in Fig. 2.5(d). The estimated bone boundaries by the APS and SEP methods are shown in Figs. 2.5(e) and (f), respectively. Note that for volunteer-II, only half of the total scan-lines are considered for both methods since almost half of the transducer

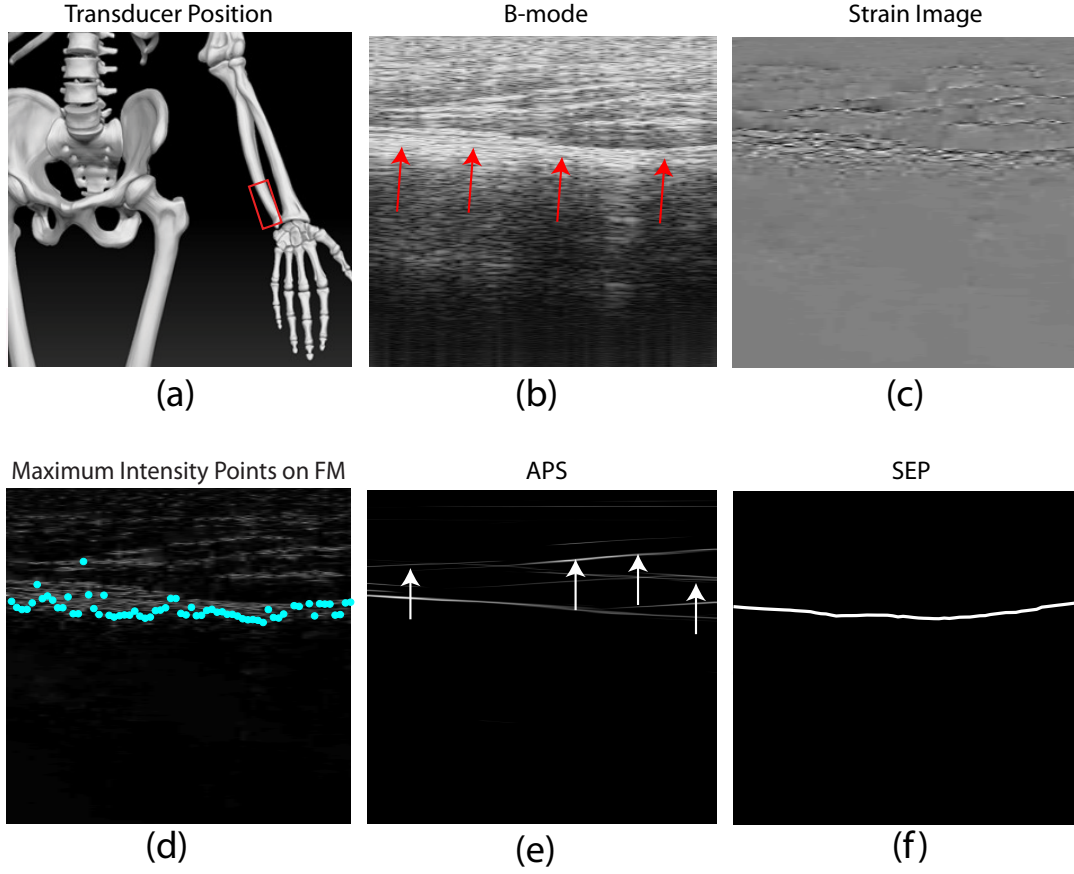


Figure 2.4: Illustration of the bone boundary detection using the *in vivo* volunteer-I data set. (a) shows the scanned region on the volunteer (shown with red rectangle), (b) is the B-mode image (bone surface is indicated with red arrows), (c) is the strain image, (d) shows the maximum intensity points overlaid on the fused map, (e) shows the detected bone boundary by the APS method, and (f) shows the detected bone boundary by the SEP method.

face laterally was in the air. As can be seen in Fig. 2.5(c) that the estimated strain image does not indicate the bone surface clearly, however, the bone intensity is quite higher than that of the soft tissue region (see Fig. 2.5(b)). So, the envelope power map is expected to complement with the bone indicating information. We see from Fig. 2.5(e) that the APS method failed to produce a continuous bone boundary. In addition, it produced false positive response for bone in the soft tissue interfaces (shown with white arrow). In contrast, the bone boundary estimated by the SEP method is free from any false positive related

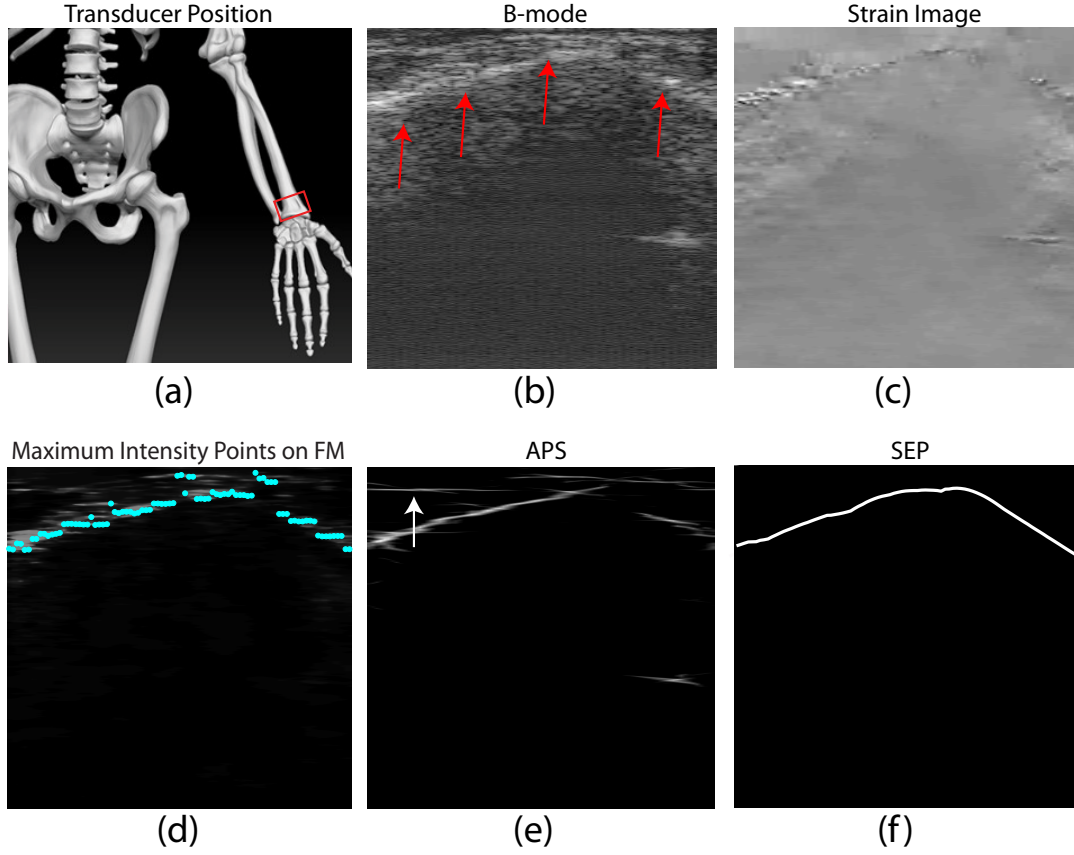


Figure 2.5: Illustration of the bone boundary detection using the *in vivo* volunteer-II data set. (a) shows the scanned region on the volunteer (shown with red rectangle), (b) is the B-mode image (bone surface is indicated with red arrows), (c) is the strain image, (d) shows the maximum intensity points overlaid on the fused map, (e) shows the detected bone boundary by the APS method, and (f) shows the detected bone boundary by the SEP method.

artifact and better match the shapes visible in the corresponding B-mode image (see Figs. 2.5(b) and (f)).

### 2.7.3.3 Case 3

Figure 2.6 demonstrates the qualitative performance comparison of the SEP and APS methods using the volunteer-III data set. The scanned region, B-mode image, and strain image are shown in Figs. 2.6(a), (b), and (c), respectively. The maximum intensity points overlaid on the fused map are shown in Fig. 2.6(d).

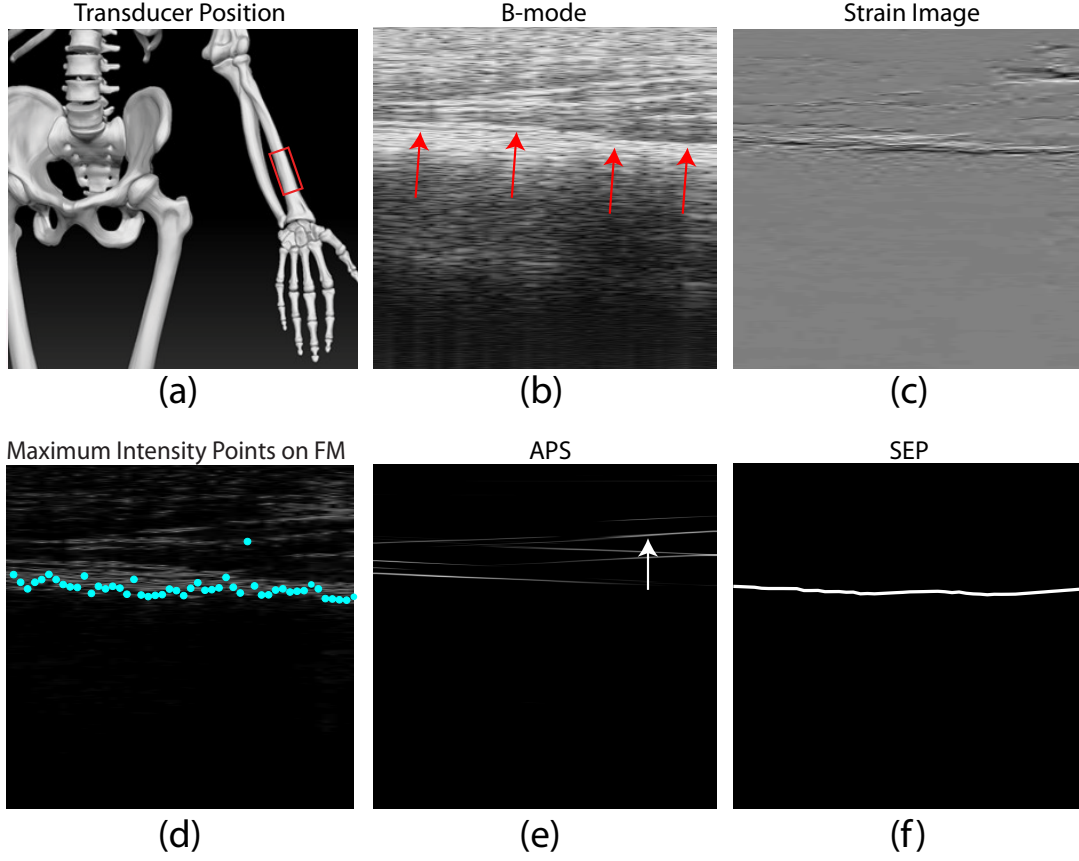


Figure 2.6: Illustration of the bone boundary detection using the *in vivo* volunteer-III data set. (a) shows the scanned region on the volunteer (shown with red rectangle), (b) is the B-mode image (bone surface is indicated with red arrows), (c) is the strain image, (d) shows the maximum intensity points overlaid on the fused map, (e) shows the detected bone boundary by the APS method, and (f) shows the detected bone boundary by the SEP method.

The estimated bone boundaries by the APS and SEP methods are shown in Figs. 2.6(e) and (f), respectively. We see from Fig. 2.6(e) that the APS method failed to produce a continuous bone boundary and also produced false positive responses at the soft tissue interfaces (shown with white arrow). In contrast, the bone boundary estimated by the SEP method better match the shapes visible in the corresponding B-mode image (see Figs. 2.6(b) and (f)). In addition, it does not produce any false positive artifact.



#### 2.7.3.4 Case 4

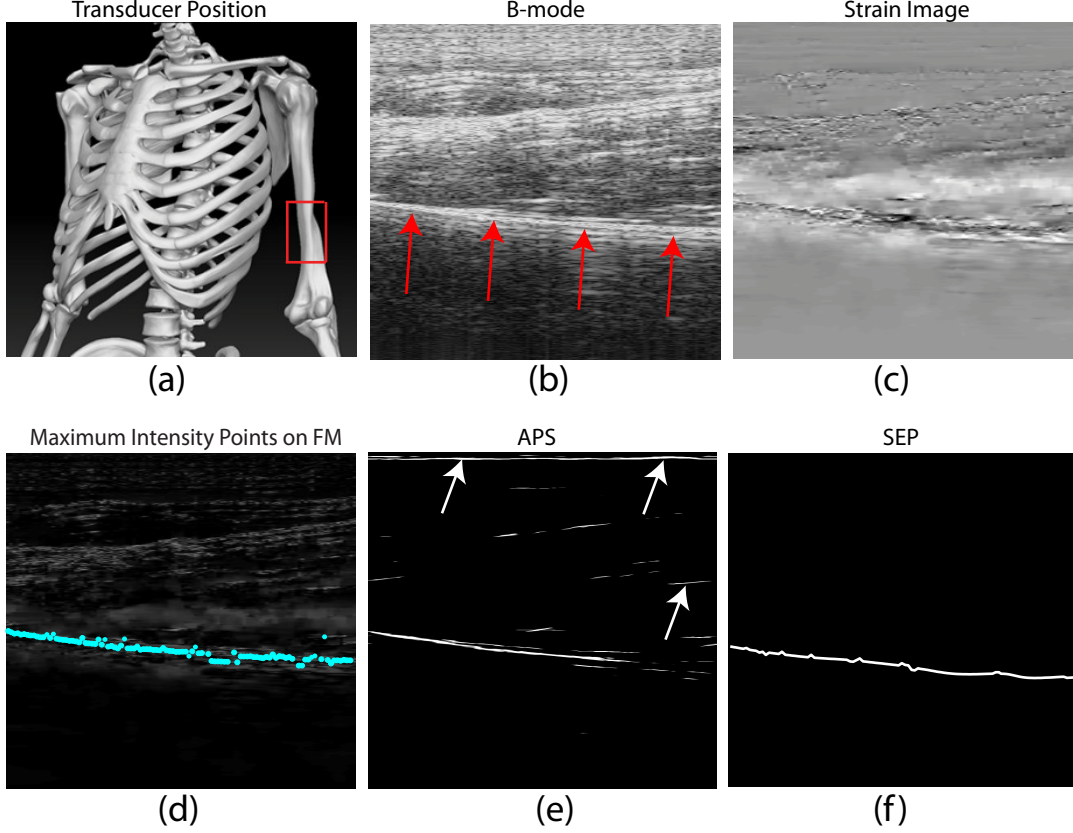


Figure 2.7: Illustration of the bone boundary detection using the *in vivo* volunteer-IV data set. (a) shows the scanned region on the volunteer (shown with red rectangle), (b) is the B-mode image (bone surface is indicated with red arrows), (c) is the strain image, (d) shows the maximum intensity points overlaid on the fused map, (e) shows the detected bone boundary by the APS method, and (f) shows the detected bone boundary by the SEP method.

We show the qualitative performance comparison of the SEP and APS methods using the volunteer-IV data set in Fig. 2.7. The scanned region, B-mode image, and strain image are shown in Figs. 2.7(a), (b), and (c), respectively. The maximum intensity points overlaid on the fused map are shown in Fig. 2.7(d). The estimated bone boundaries by the APS and SEP methods are shown in Figs. 2.7(e) and (f), respectively. Here, the estimated strain image satisfactorily indicates the bone surface (see Fig. 2.7(c)). In addition, the B-mode intensity for the bone surface is also quite prominent than that for the soft tissue region.

Therefore, the envelope power map is expected to complement with the bone indicating information. We see from Fig. 2.7(e) that the estimated bone boundary by the APS method is not continuous. In addition, it produced false positive response for bone in the soft tissue interfaces (shown with white arrows). In contrast, the bone boundary estimated by the SEP method is free from any false positive related artifact and better match the shapes visible in the corresponding B-mode image (see Figs. 2.7(b) and (f)).

### 2.7.3.5 Case 5

Finally, in Fig. 2.8, we demonstrate the qualitative performance comparison of the SEP and APS methods using the volunteer-V data set. The scanned region, B-mode image, and strain image are shown in Figs. 2.8(a), (b), and (c), respectively. The maximum intensity points overlaid on the fused map are shown in Fig. 2.8(d). The estimated bone boundaries by the APS and SEP methods are shown in Figs. 2.8(e) and (f), respectively. Here also, we see that the estimated bone boundary by the APS method is not continuous (see Fig. 2.8(e)). In addition, it produced false positive response for bone in the soft tissue interfaces (shown with white arrows). In contrast, similar to previous cases, the bone boundary estimated by the SEP method better match the shapes visible in the corresponding B-mode image (see Figs. 2.8(b) and (f)).

## 2.8 Advantages and Limitations

We discussed a novel method for robust bone boundary localization based on the fusion of strain-imaging and envelope signal power detection. We combined real-time strain-imaging based on analytic minimization of regularized cost functions with an envelope power map of the pre-compression RF frame. Our results demonstrated reduced bone localization error through better elastogram resolution, adoption of envelope power map of higher dynamic range, addressing the false positive bone response, and exploiting the smoothing feature of the AM method to better delineate the bone boundary in strain image. We demonstrated our improved performance on a wide range of validation data including a simulated FEM phantom, a physical experimental phantom, and *in vivo* data of the

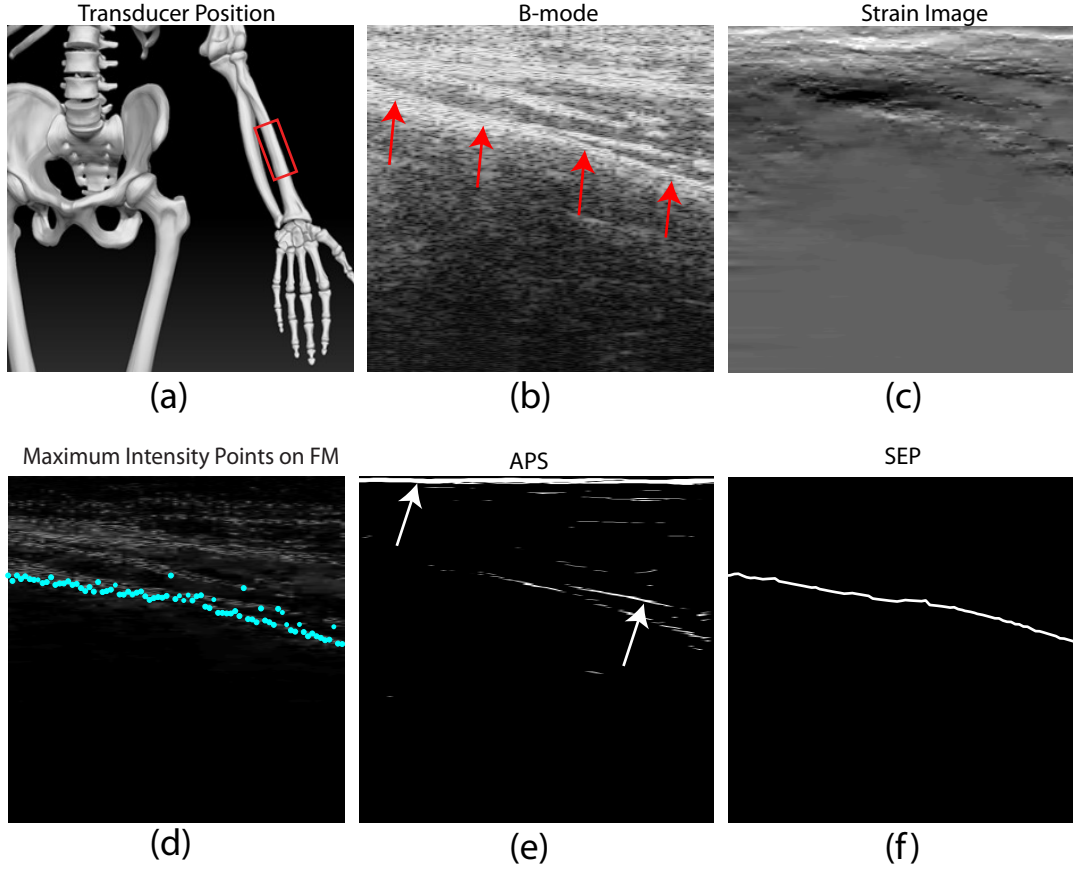


Figure 2.8: Illustration of the bone boundary detection using the *in vivo* volunteer-V data set. (a) shows the scanned region on the volunteer (shown with red rectangle), (b) is the B-mode image (bone surface is indicated with red arrows), (c) is the strain image, (d) shows the maximum intensity points overlaid on the fused map, (e) shows the detected bone boundary by the APS method, and (f) shows the detected bone boundary by the SEP method.

human with reported improvements of approximately 13% and 15% in terms of MAE in the FEM and experimental phantom tests, respectively, when compared with current state-of-the-art.

Although this study demonstrates great promise in 2D bone segmentation, however, the empirical selection of the value for  $\lambda$  may result in great challenges in dealing with the data from patients having clinical conditions. In addition, proper choice of the linear fitting window length is also critical. Therefore, a data-driven analysis and choice of these parameter values are of great importance. This

method also lacks a feature to identify any discontinuity in the bone boundary.

## Chapter 3

# Improved 2D Bone Contour Extraction Using Data-driven Parameters

In this chapter, we significantly improve our preliminary work described in the previous chapter and also mitigate the limitations associated with it by introducing automatic parameter selection processes that replace all of the intuitive assumptions and thus, make the method more robust and self-tuning. We improve our previous 2D strain-imaging-based bone segmentation approach discussed in Chapter 2 by incorporating a depth-dependent cumulative power of the envelope into the elastographic data as well as incorporating an echo de-correlation measure-based weight to fuse the strain and envelope map. We also use a data driven scheme to detect the presence of any bone discontinuity in the scanned US image and introduce a multivariate non-parametric Gaussian mixture regression that to be used over the maximum intensity points of the fused map.

### 3.1 Improved Modified Envelope Map (MEM) and Modified Strain Map (MSM) Estimation

We already discussed in Section 2.2 that we use a real-time strain-imaging [82] based on analytic minimization (AM) of regularized cost functions. However, as discussed in [82], an inherent limitation of that method is that over-smoothing of the strain image occurs in places where the RF echo is weaker, which results in increase in the share of the regularization term in the cost  $C_j$  defined as

$$C_j(\Delta a_1, \dots, \Delta a_m, \Delta l_1, \dots, \Delta l_m) = \sum_{i=1}^m \{ [I_1(i, j) - I_2(i + a_i + \Delta a_i, j + l_i + \Delta l_i)]^2 + \alpha(a_i + \Delta a_i - a_{i-1} + \Delta a_{i-1})^2 + \beta_a(l_i + \Delta l_i - l_{i-1} + \Delta l_{i-1})^2 + \beta'_l(l_i + \Delta l_i - l_{i,j-1})^2 \}, \quad (3.1)$$

where  $\alpha$ ,  $\beta_a$  and  $\beta'_l$  are the tuneable parameters,  $a_i$  and  $\Delta a_i$  are the integer and sub-sample axial displacements, respectively, and  $l_i$  and  $\Delta l_i$  are the integer and sub-sample lateral displacements, respectively, of the  $i$ th sample in the  $j$ th scan-line.

In our subsequent work, we exploit this limitation to improve the bone delineation accuracy further. Since the RF echo and its envelope is already weaker beneath the bone surface due to very high US beam reflection at the bone tissue interface, we further modify the envelope map by reducing the intensity associated with the soft tissue region (area between the bone and the transducer face) using the axially cumulative power and produce modified envelope maps, MEM<sub>1</sub> and MEM<sub>2</sub> from  $I_1$  and  $I_2$ , respectively, as

$$\text{MEM}_r(i, j) = \frac{E_r(i, j)^{P_r(i, j)}}{\max[E_r(i, j)^{P_r(i, j)}]}, \quad (3.2)$$

where  $r$  corresponds to 1 and 2 denoting the pre- and post-compression images, respectively,  $E_r$  is the envelope estimated using the Hilbert transform of  $I_r$  [45], and  $P_r(i, j) = \sum_{p_o=1}^i E_r^2(p_o, j)$ . Finally, we estimate strain (**S**) using MEM<sub>1</sub> and MEM<sub>2</sub> which results an over-smoothing in both the top and bottom regions of

the bone boundary. For robust bone boundary estimation, we combine  $\mathbf{S}$  with  $\text{MEM}_1$ . Therefore, in order to get an equivalent dynamic range of  $\mathbf{S}$  with that of the  $\text{MEM}_1$ , we estimate a modified strain map  $\text{MSM} = \hat{\mathbf{S}} / \max[\hat{\mathbf{S}}]$ , where

$$\hat{\mathbf{S}}(i, j) = \begin{cases} -\mathbf{S}(i, j); & \text{if } \mathbf{S}(i, j) < 0 \\ \mathbf{S}(i, j); & \text{otherwise} \end{cases} \quad (3.3)$$

## 3.2 Data-driven Weight Estimation

Here, we recap again from Section 2.4 on the estimation of the fused map using the MSM and  $\text{MEM}_1$  as

$$\text{FM} = \lambda \times \text{MSM} + (1 - \lambda) \times \text{MEM}_1, \quad (3.4)$$

where,  $\lambda$  controls the contribution of MSM into the fused map. In this section, we target to automate the process of choosing the value of  $\lambda$ .

To observe the effect of different values of  $\lambda$  on the bone boundary estimation accuracy, we use FEM-II simulation phantom (see Section 3.5 for detail). We use the actual and estimated bone boundaries of FEM-II to estimate mean absolute error (MAE) at different values of  $\lambda$  which is shown in Fig. 3.1(a). For this MAE analysis, we use pre- and post-compression RF frames having 10dB signal-to-noise ratio (SNR), where the SNR is deliberately chosen to be lower than the typically encountered values (approximately 18~22dB) in RF data after beamforming [86] to simulate a worse case scenario. We also use 1% strain data to ensure that the echo de-correlation is low enough. We see from Fig. 3.1(a) that the lowest MAE is at  $\lambda = 0.5$ . However, by the increase of echo de-correlation, estimated strain image becomes more noisy. Free hand elastography is prone to echo de-correlation and by the increase of applied pressure, echo de-correlation increases significantly that leads to noisy strain map [83]. To demonstrate this effect, we use FEM-I simulation phantom (see Section 3.5 for detail) and estimate the normalized cross-correlation (NCC) between pre- and post-compression RF frame of FEM-I at different applied strains (i.e., 1%-8% applied strains). The mean NCC peaks at different applied strains are plotted in Fig. 3.1(b). We can see from this figure that the peaks of the NCC coefficients deteriorate and thus, the quality of strain images deteriorate with the increase of applied strain.

We incorporate the echo de-correlation measure between the pre- and post-compression RF frames to automatically choose a suitable value for  $\lambda$ . To estimate the degree of echo de-correlation, we consider a smaller (i.e., 10mm $\times$ 10mm) region-of-interest (ROI) closer to the transducer face in the pre- and post-compression echo frames. We choose axial length of the ROI to be 10mm so that three 1D RF signal windows of length  $L = 5$ mm each with 50% axial overlap can be used to estimate cross-correlation coefficients. We also choose  $L$  to be 5mm since the cross-correlation between the pre- and post-compression RF windows of length 3~5mm (with transducer center frequency 5~10MHz) produces satisfactory lag to estimate tissue displacement [80]. We use lateral length of the ROI to be 10mm, however can be chosen up to the width of the RF frame. After defining the ROI, we stretch the post-compression signal windows in the ROI by a factor  $\alpha$ , i.e.,  $I_\alpha(i) = I_2(\alpha i)$ . By neglecting the noise term (i.e.,  $\nu_\alpha(i) = 0$  in Eqn. (2.2)), we define the NCC  $\rho_\alpha(k)$  ( $\leq 1$ ) as [83]

$$\rho_\alpha(k) = \frac{\sum_{i=1}^L I_1(i) \cdot I_\alpha(i+k)}{\sqrt{\sum_{i=1}^L \{I_1(i)\}^2 \sum_{i=1}^L \{I_\alpha(i)\}^2}}. \quad (3.5)$$

Equation (3.5) becomes maximum for  $\alpha = \epsilon$  with the assumption of  $p(\alpha t) \cong p(t)$ . After estimating  $\rho_\alpha(k)$  for all the scan-lines inside the ROI, the mean NCC peak is estimated as

$$\rho_{avg} = \frac{1}{M} \sum_{w=1}^M \max\{\rho_\alpha(k)\}_w, \quad (3.6)$$

where  $M$  is the total number of 1D signal windows inside the ROI. Note that to find individual peak among NCC coefficients of each window in the sub-sample level, we use cosine interpolation [83].

Now, based on the value of  $\rho_{avg}$ , we consider three cases: (i) if  $\rho_{avg}$  is equal or greater than 0.9, we can consider echo de-correlation between the pre- and post-compression echo frames is significantly low [89]. In that case,  $\lambda = 0.5$  works the best as evident from Fig. 3.1(a). (ii) If  $\rho_{avg}$  is less than 0.5, it is obvious that the degree of echo de-correlation is greater than the correlation. Then we choose  $\lambda = 0$  (i.e., no contribution from the noisy strain image). And (iii) if the value of  $\rho_{avg}$  varies between 0.5 and 0.9, we assume a linear relation of  $\lambda$  with  $\rho_{avg}$  and



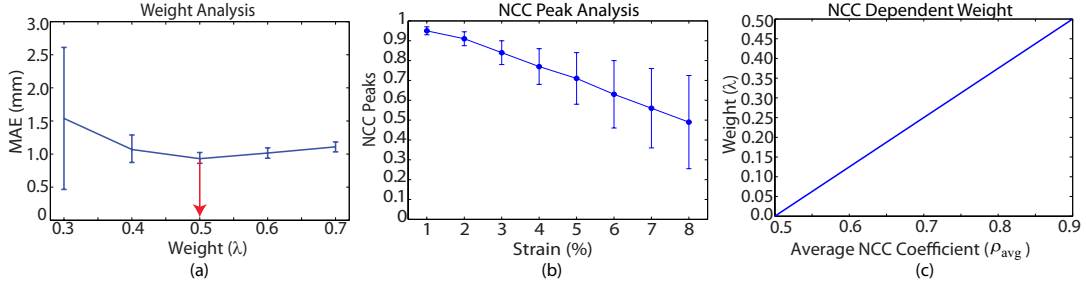


Figure 3.1: (a) Mean absolute error (MAE) analysis for different values of  $\lambda$  at 10dB SNR (weight at minimum error is shown with red arrow), (b) Normalized cross-correlation coefficients with respect to applied strains for FEM-I phantom (see Section 3.5 for detail), and (c) Normalized cross-correlation coefficient dependent linear weight  $\lambda$ .

thus choose the value for  $\lambda$  from a linear function of  $\rho_{avg}$  (see Fig. 3.1(c)) defined as

$$\lambda = \frac{5}{4}(\rho_{avg} - 0.5). \quad (3.7)$$

It might seem that the data-driven weight has a number of fix parameters, e.g., the upper and lower bound of the weight and  $\rho_{avg}$ . However, these parameters are chosen based on the state-of-the-art practice (i.e., the method in [89] runs in the commercial US scanners manufactured by the Ultrasonix medical corporation, Richmond, BC) and vigorous observations made on the bone localization accuracy using different types of data. In addition, our sole target is to control the contribution of a strain image into the fused map based on the fact that how good that strain image is. Therefore, we believe that our data-driven weight serves this purpose irrespective of data types, and its efficacy is quantitatively demonstrated in the results section (see Section 3.6.3).

However, after estimating the fused map, the location of maximum intensity point along each scan-line of the map is then used as the initial bone boundary  $\mathbf{Y}(=[y_1, y_2, \dots, y_n])$ , where  $y_j$  is the axial sample number at  $j$ th scan-line in the FM. We also use Grubbs test [90] to discard any outlier in  $\mathbf{Y}$ .

### 3.3 Bone Discontinuity Detection

To detect possible discontinuity in the bone surface, we estimate the lease-square-error-based gradient  $\nabla \mathbf{Y} = d\tilde{\mathbf{Y}}/d\mathbf{X}$  [91], where  $\mathbf{X}(=[x_1, x_2, \dots, x_n])$ ,  $\tilde{\mathbf{Y}}$  is the

bone boundary after regression, and  $x_j$  represents the location of  $y_j$  in the lateral direction. Although the selection of proper window length for regression is crucial, our primary target here is to find a comparably larger jump in the values of  $\nabla \mathbf{Y}$  in the location of bone discontinuity. Therefore, we use larger regression window of length 5mm so that the noisy estimates can be better minimized as well as a noticeable jump in the location of bone discontinuity is preserved in the values of  $\nabla \mathbf{Y}$ . Then we use the local statistics of  $\nabla \mathbf{Y}$  such that any point on  $\nabla \mathbf{Y}$  exceeds  $\mu + 3\sigma$  (where  $\mu$  and  $\sigma$  are the mean and standard deviation of  $\nabla \mathbf{Y}$ ) is flagged as a bone discontinuity. We choose  $\mu + 3\sigma$  to cover a confidence interval of 0.997 assuming that  $\nabla \mathbf{Y}$  is normally distributed. Each continuous portion of  $\mathbf{Y}$  is considered as a segment and after finding all the segments, we use Gaussian mixture regression over each of the segments separately.

### 3.4 Gaussian Mixture Regression (GMR)

In this work, we use GMR that overcomes the following drawbacks of linear regression which we used in our previous work [29]:

1. Choosing a suitable length for regression window is ambiguous since smaller windows cannot produce smoother bone boundary if  $\mathbf{Y}$  is noisy. On the other hand, comparatively larger regression window causes loss of local curvature information in  $\mathbf{Y}$ .
2. Parametric linear regression models are often too rigid to model general nonlinear patterns in data space and thus, a more flexible model of non-parametric regression is required [92].

Now let  $f_{X,Y}(x, y) = \sum_{k=1}^K \pi_k \phi(x, y; \mu_k, \Sigma_k)$  be the joint density function of the maximum intensity points identified in the FM.  $K$  is the total number of clusters present in  $Y$  as estimated from a spectral clustering analysis [93]. The spectral clustering approach is based on an eigenvalue analysis of the affinity matrix of the interrogated point clouds. Eigenvalues 1 or close to 1 typically indicate a natural estimate of the number of clusters to be used to model the data. However, if the groups are not clearly separated, once noise is introduced, the

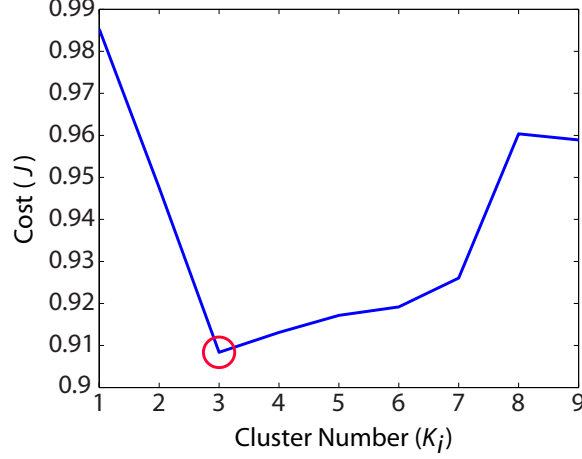


Figure 3.2: The alignment cost for varying cluster numbers.

values start to deviate from 1, thus the criterion of choice becomes tricky. Thus, authors in [93] adopted an approach which relies on the structure of the eigenvectors. This idea is based on the fact that each eigenvector column corresponding to an eigenvalue 1 will have only a single non-zero entry. In addition, the eigenvector columns corresponding to eigenvalues 1 form a canonical coordinate system in an ideal case. Thus, for a noisy data set, the algorithm in [93] forms a cost function with respect to different possible cluster numbers  $K_i$ , where for each  $K_i$ , the eigenvector columns are repeatedly rearranged such that the rearranged first  $K_i$  columns form a canonical coordinate system and contain only a single non-zero entry in each of first  $K_i$  columns. Let  $Z$  be the matrix of size  $n \times K_i$  obtained after rotating (rearranging) the eigenvector matrix, and  $M_p = \max_q Z_{pq}$ . Then the cost function is defined as [93]

$$J = \sum_{p=1}^n \sum_{q=1}^{K_i} \frac{Z_{pq}^2}{M_p^2}. \quad (3.8)$$

The cluster number  $K_i$  for which the cost  $J$  (Eqn. (3.8)) becomes minimum is taken as the final cluster number  $K$ . For example, we plot the cost values for different cluster number  $K_i$  using the *in vivo* volunteer-I data set (see Section 3.6.3) in Fig. 3.2. Here we see that the cost is minimum for  $K_i = 3$ .

However,  $\pi_k$ ,  $\mu_k = [\mu_{kX}; \mu_{kY}]$  and  $\Sigma_k = [\Sigma_{kX} \ \Sigma_{kXY}; \Sigma_{kYX} \ \Sigma_{kYY}]$  in the joint density function are the probability, mean and covariance matrix, respectively, of

the data points in the  $k$ th cluster and are estimated from an expectation maximization algorithm [94], and  $\phi(x, y; \mu_k, \Sigma_k)$  is the probability density function of points inside  $k$ th cluster defined as

$$\begin{aligned} \phi(x, y; \mu_k, \Sigma_k) \\ = \frac{1}{2\pi\sqrt{|\Sigma_k|}} \exp \left[ -\frac{1}{2}(D - \mu_k)^T \Sigma_k^{-1} (D - \mu_k) \right], \end{aligned} \quad (3.9)$$

where  $D = [\mathbf{X}; \mathbf{Y}]$ . Then, from  $f_{X,Y}(x, y)$ , our GMR equation can be derived which takes the form as [92]

$$b(x) = E[\mathbf{Y}|\mathbf{X} = x] = \sum_{k=1}^K w_k(x) d_k(x), \quad (3.10)$$

where  $d_k(x) = \mu_{kY} + \Sigma_{kYX} \Sigma_{kX}^{-1} (x - \mu_{kX})$ , and  $\mu_{kX}$  and  $\Sigma_{kX}$  are the mean and covariance matrix of the marginal density function ( $f_X$ ) of  $\mathbf{X}$ , in the  $k$ th data cluster. In addition,  $w_j(x)$  is the mixing weight defined as

$$w_k(x) = \frac{\pi_k \phi(x; \mu_{kX}, \Sigma_{kX})}{\sum_{k=1}^K \pi_k \phi(x; \mu_{kX}, \Sigma_{kX})}. \quad (3.11)$$

GMR covers a spectrum of regression models of varying flexibility, ranging from the multivariate nonparametric kernel regression ( $K = N; N > 1$ ) to the classical linear regression model ( $K = 1$ ) [92].

## 3.5 Validation Setup

### 3.5.1 Simulated Phantom

We built three 40mm×40mm (axial×lateral) FEM phantoms using the analysis software ANSYS (ANSYS, Inc., Canonsburg, PA) and the ultrasound simulation software Field II [87]. The first phantom was generated to show the echo de-correlation effect with the applied mechanical stress where total number of nodes were 54,405. Our second and third phantoms mimicked 2D US scans of a normal human distal radius bone (FEM-II) and a fractured human distal radius bone (FEM-III) with a total number of 55,180 nodes. The stiffness of the

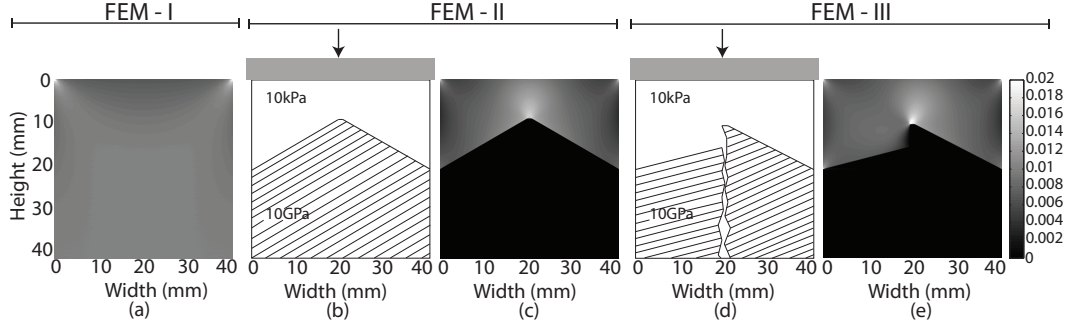


Figure 3.3: FEM simulation phantoms. (a) FEM-I: ideal elastogram of a homogeneous soft tissue of stiffness 10kPa. (b) FEM-II: normal distal radius bone and soft tissue region of stiffness 10GPa and 10kPa, respectively, and (c) corresponding ideal elastogram. (d) FEM-III: fractured distal radius bone and soft tissue region of stiffness 10GPa and 10kPa, respectively, and (e) corresponding ideal elastogram.

homogeneous soft tissue and bone regions were set to 10kPa and 10GPa, respectively, (see Fig. 3.3) as previously reported [88]. Our phantom was compressed in the lateral direction from the top using a planar compressor that was wider than the phantom. We set an applied pressure level that corresponds to 1% average strain. An ultrasonic transducer of center frequency,  $f_0 = 5\text{MHz}$  and band-width = 50% was used to simulate the phantom scan from the top. The total number of scan lines was set to 128. The resulting pixel size of the 2D data was  $0.015\text{mm} \times 0.3\text{mm}$ . Figures 3.3(a), (c) and (e) show the ideal elastograms of FEM-I, FEM-II and FEM-III, respectively, at 1% applied strain.

### 3.5.2 Experimental Phantom

We constructed an experimental phantom using a radio-opaque Sawbones hemipelvis (Sawbones, Pacific Research Laboratories, Inc., Vashon Island, WA), model number 1297-22. A portion of the pelvis was suspended in polyvinyl chloride (PVC) gel (see Fig. 2.1(a)) and placed in an acrylic tube (see Fig. 2.1(b)). A high resolution peripheral quantitative CT machine, model HR pQCT Xtreme CT (Scanco USA, Inc., Wayne, PA) was used to acquire a single  $482 \times 482 \times 402$  (lateral  $\times$  axial  $\times$  elevation) volume with a resolution of  $0.25\text{mm} \times 0.25\text{mm} \times 0.25\text{mm}$ . The US images were acquired using a SonixRP (Ultrasonix Medical Corporation, Richmond, BC) scanner in the Center for Hip Health and Mobility, Vancouver

Coastal Health Authority, Vancouver, BC, Canada. We used a L14-5W/60 linear array probe operating at 10MHz for collecting data for the 2D implementations.

### 3.5.3 *In Vivo* Data

We acquired five sets of data from five volunteers (volunteer-I: 25-year old male; volunteer-II: 33-year old male; volunteer-III: 26-year old male; volunteer-IV: 24-year old male; volunteer-V: 27-year old male) after obtaining prior consent. All data were acquired with free-hand compression. The US images were acquired using a SonixRP (Ultrasonix Medical Corporation, Richmond, BC) scanner in the Center for Hip Health and Mobility, Vancouver Coastal Health Authority, Vancouver, BC, Canada. Here also, we used a L14-5W/60 linear array probe operating at 10MHz. The study was approved by UBC clinical research ethics board.

## 3.6 Results

We provide comparative results of our proposed 2D strain and envelope power-based bone detection method (2DSE) with the previously reported adaptively parameterized local phase feature-based (2DOPS) [57] using the FEM phantoms, experimental phantom and *in vivo* data. The 2DOPS method selects parameters automatically for the Log-Gabor filters based on properties estimated directly from the specific US image that is being analyzed. We calculate mean absolute error (MAE) which is defined as

$$\text{MAE} = \frac{1}{P} \sum_{p=1}^P |A(p) - G(p)|, \quad (3.12)$$

where  $P$  represent the number of data points spanned by the bone boundary in the lateral directions,  $A$  is a matrix containing the ‘ground truth’ bone boundary points, and  $G$  is a matrix containing the estimated bone boundary points. As ground truth, we used the bone geometry defined for Field II simulation for the FEM, the estimated bone boundary from the computed tomography (CT) image for the experimental phantom, and expert delineation of bone boundaries on

B-mode images for the *in vivo* data. We use fiducial-based CT and US bone alignment before estimating the MAE for the experimental phantom. Note that we use bottom-up ray casting in the phase-symmetry images for the 2DOPS method to get  $G$  as suggested in [57]. Also note that we use the initial bone boundary estimates  $\mathbf{Y}$  to estimate the MAE for the 2DSE method for a fair comparison. Also note that since we use expert delineated bone contours as ground truth for the *in vivo* data, therefore, the estimated error using Eqn. 3.12 for the *in vivo* data is called mean absolute fitting error.

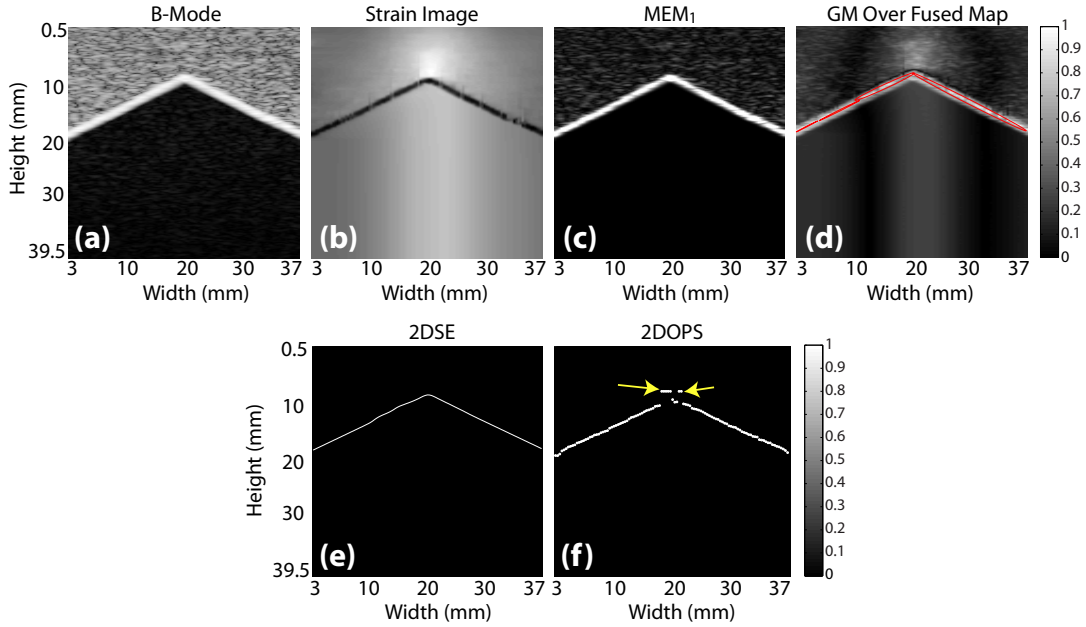


Figure 3.4: Illustration of 2D bone boundary detection using the FEM-I phantom. (a) B-mode image, (b) strain image generated by the proposed approach, (c)  $\text{MEM}_1$ , (d) Gaussian mixtures representation over fused map, and estimated bone boundary by the (e) 2DSE and (f) 2DOPS methods (arrows show leakage). Bone boundary is shown after bottom up ray-casting for the 2DOPS method.

### 3.6.1 FEM Results

We provide comparative qualitative results of the 2DSE and 2DOPS methods using the FEM data. In Figs. 3.4(a), (b), (c) and (d), we show the B-mode image, estimated strain image,  $\text{MEM}_1$ , and fused map, respectively, for FEM-

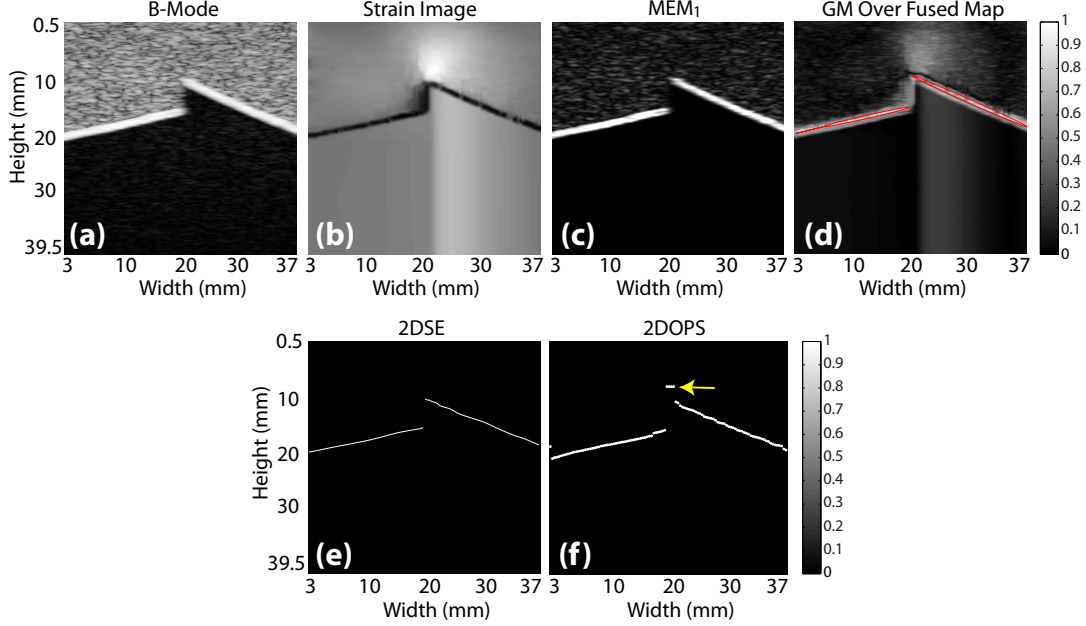


Figure 3.5: Illustration of 2D bone boundary detection using the FEM-II phantom. (a) B-mode image, (b) strain image generated by the proposed approach, (c)  $MEM_1$ , (d) Gaussian mixtures representation over fused map, and estimated bone boundary by the (e) 2DSE and (f) 2DOPS methods (arrow shows leakage). Bone boundary is shown after bottom up ray-casting for the 2DOPS method.

II. To show the efficacy of our proposed method in case of discontinuous bone boundary localization, we show results for FEM-III in Fig. 3.5. In Figs. 3.5(a), (b), (c) and (d), we show the B-mode, estimated strain  $\mathbf{S}$ ,  $MEM_1$ , and fused maps, respectively. In Figs. 3.4(e) and 3.5(e), we show the bone boundaries detected by the 2DSE method for the FEM-II and FEM-III, respectively. In addition, we show the bone boundaries detected by the 2DOPS method for the FEM-II and FEM-III in Figs. 3.4(f) and 3.5(f), respectively. Since the 2DOPS method depends on ray-casting to extract final bone boundary from the phase symmetry images, these methods become prone to “leaking” through weak areas in the phase symmetry profiles. As evident we see in Figs. 3.4(f) and 3.5(f) that the ray-casting leaks through weak spots in the phase symmetry profiles of the bone and catches intensities associated with the soft tissue layer (indicated by yellow arrows in Figs. 3.4(f) and 3.5(f)). In contrast, the bone boundaries



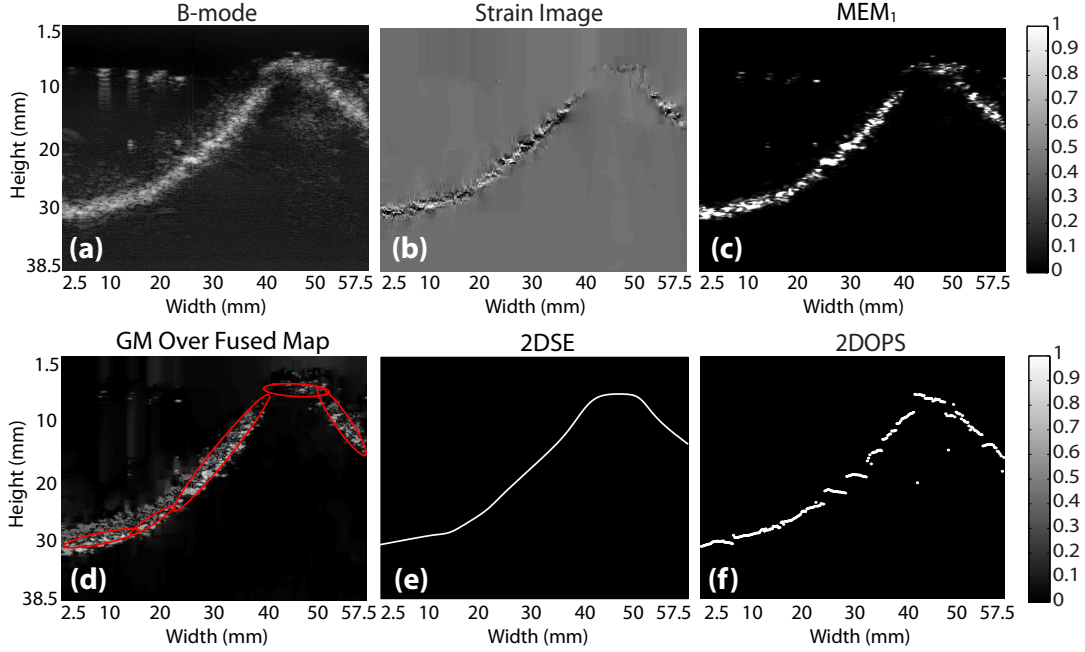


Figure 3.6: Illustration of 2D bone boundary detection using the experimental phantom. (a) B-mode image, (b) strain image generated by the proposed approach, (c)  $MEM_1$ , (d) Gaussian mixtures representation over fused map, (e) estimated bone boundary by the 2DSE method, and (f) estimated bone boundary by the 2DOPS method (bone boundary is shown after bottom up ray-casting).

produced by the 2DSE method (see Figs. 3.4(e) and 3.5(e)) appear to be free of such artefacts.

### 3.6.2 Experimental Phantom Results

Figure 3.6 demonstrates the qualitative performance comparison of the 2DSE and 2DOPS methods using the experimental phantom. In Figs. 3.6(a), (b), (c) and (d), we show the B-mode image, strain image,  $MEM_1$ , and fused map, respectively. We show the detected bone boundaries by the 2DSE and 2DOPS methods in Figs. 3.6(e) and (f), respectively. We can see from Fig. 3.6(f) that the bone boundary estimated by the 2DOPS method is discontinuous. In contrast, the bone boundary estimated by the 2DSE method is continuous and smooth (see Fig. 3.6(f)).

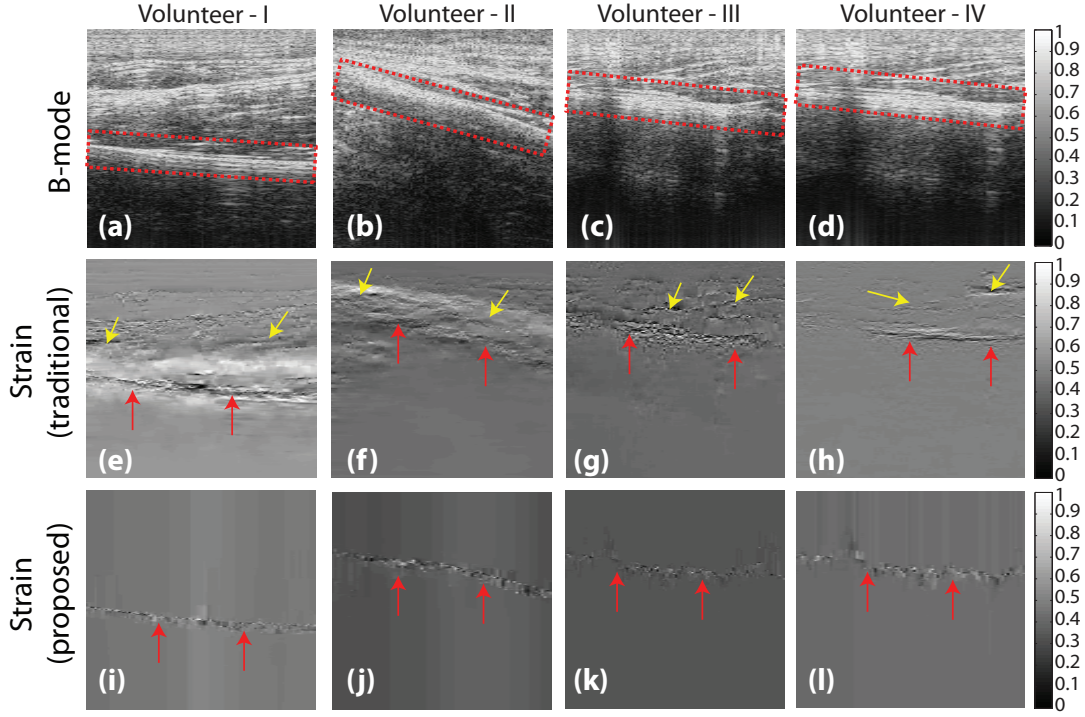


Figure 3.7: Illustration of the proposed strain-imaging performance. (a)-(d) show the B-mode images where overlaid red-dotted boxes indicate the bone locations. (e)-(h) show the strain images generated by the traditional method adopted in [29] (red arrows indicate the true bone locations while yellow arrows indicate artifacts associated with soft tissue layers), and (i)-(l) show the strain images generated by the proposed method (red arrows indicate the true bone locations).

### 3.6.3 *In Vivo* Results

In Fig. 3.7, we show the strain estimation performance of the proposed method and that used in [29]. We see from Figs. 3.7(e)-(h) that the method used in [29] produces confounding artifacts in the soft tissue layers (indicated with yellow arrows). In contrast, the strain images produced by our proposed method is free of such artifacts as evident in Figs. 3.7(i)-(l). Next we compare the bone boundary detection performance of the 2DSE and 2DOPS methods for the five *in vivo* volunteer data cases. An Orthopedic expert delineated the bone boundaries on the B-mode images which we consider as the ground truths for a comparative analysis of the 2DSE and 2DOPS methods.

### 3.6.3.1 Case 1

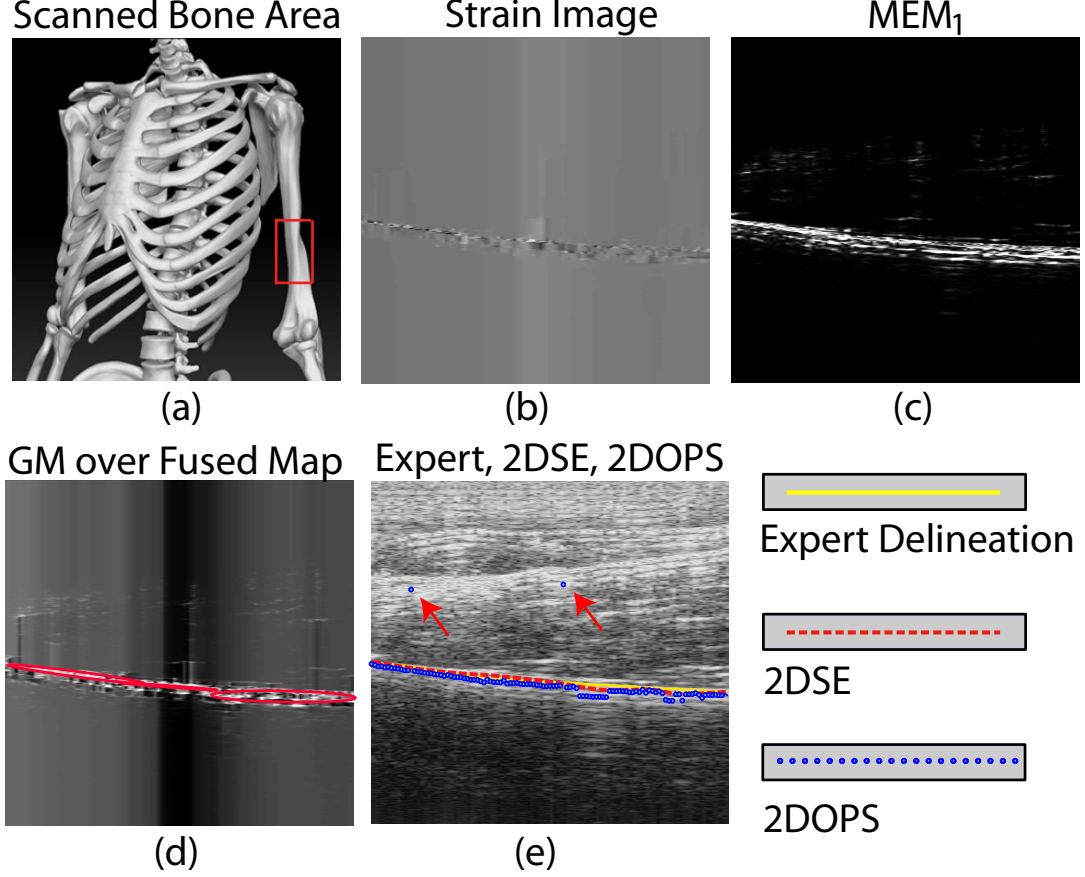


Figure 3.8: Illustration of 2D bone boundary detection using the *in vivo* volunteer-I data set. (a) shows bone region scanned on the volunteer (with red rectangle), (b) is the strain image generated by the proposed approach, (c) is the  $MEM_1$ , and (d) is the fused map with the Gaussian mixtures overlaid. Finally, in (e), orthopaedic expert delineated bone boundary, and detected bone boundary by the 2DOPS and 2DSE methods are overlaid on the B-mode image (bone boundary produced by the 2DOPS method is shown after bottom up ray-casting).

We show the qualitative performance comparison of the 2DSE and 2DOPS methods using the volunteer-I data set in Fig. 3.8. The scanned region, strain image, envelope power map, and the fused map are shown in Figs. 3.8(a), (b), (c), and (d), respectively. The expert delineated bone contour, and the estimated bone boundaries by the 2DSE and 2DOPS methods are overlaid on the B-mode image as shown in Fig. 3.8(e). We see from Fig. 3.8(e) that the bone boundary

produced by the 2DOPS method satisfactorily close to the expert delineated contour though there are some sporadic points (shown with red arrows) resulted from the false positive responses. However, the bone boundary estimated by the 2DSE method better matches the shape as marked by the expert in the B-mode images (see Figs. 3.8(e)). In addition, the 2DSE method does not produce false positives at soft tissue interfaces.

### 3.6.3.2 Case 2

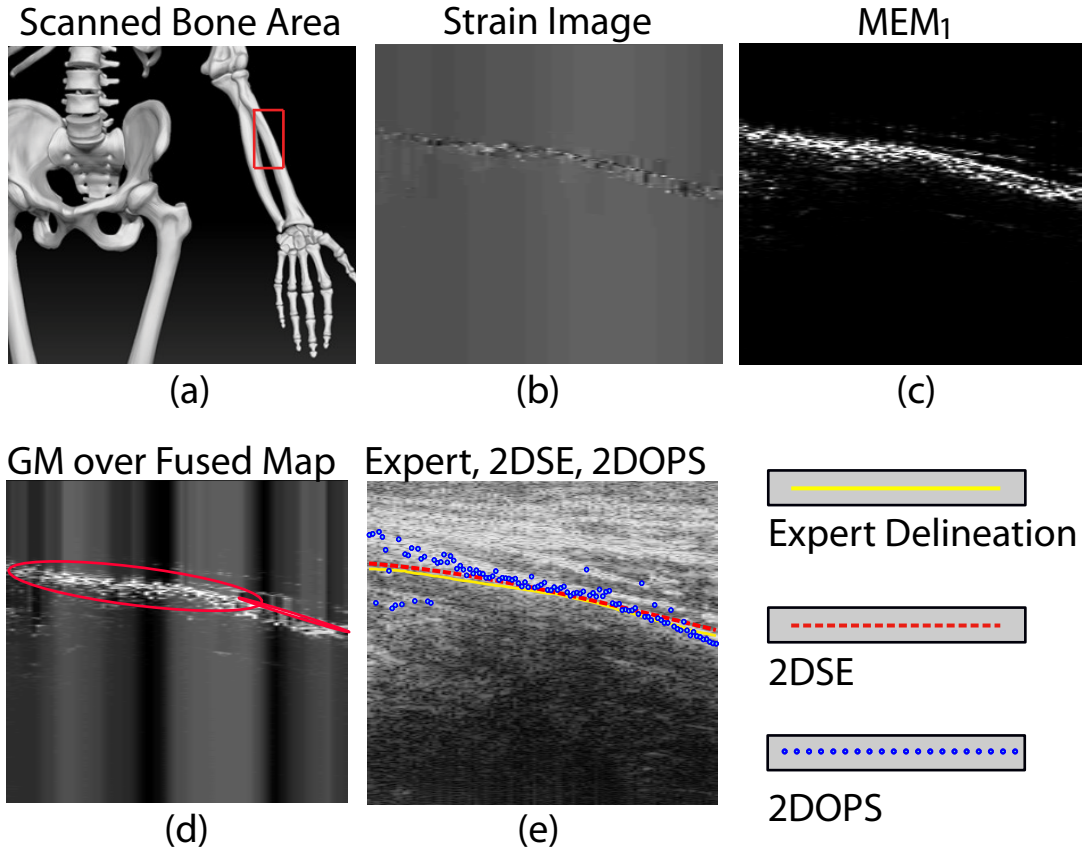


Figure 3.9: Illustration of 2D bone boundary detection using the *in vivo* volunteer-II data set. (a) shows bone region scanned on the volunteer (with red rectangle), (b) is the strain image generated by the proposed approach, (c) is the MEM<sub>1</sub>, and (d) is the fused map with the Gaussian mixtures overlaid. Finally, in (e), orthopaedic expert delineated bone boundary, and detected bone boundary by the 2DOPS and 2DSE methods are overlaid on the B-mode image (bone boundary produced by the 2DOPS method are shown after bottom up ray-casting).

Figure 3.9 demonstrates the qualitative bone localization performance comparison of the 2DSE and 2DOPS methods using the volunteer-II data set. The scanned region, strain image, envelope power map, and the fused map are shown in Figs. 3.9(a), (b), (c), and (d), respectively. The expert delineated bone contour, and the estimated bone boundaries by the 2DSE and 2DOPS methods are overlaid on the B-mode image as shown in Fig. 3.9(e). We see from Fig. 3.9(e) that the bone boundary produced by the 2DOPS method varies noticeably in some places. This variation results from the false positive bone responses. In contrast, the bone boundary estimated by the 2DSE method does not produce any false positive-based artifact and better matches the shape as marked by the expert in the B-mode images (see Fig. 3.9(e)).

### 3.6.3.3 Case 3

We show the qualitative performance comparison of the 2DSE and 2DOPS methods using the volunteer-III data set in Fig. 3.10. The scanned region, strain image, envelope power map, and the fused map are shown in Figs. 3.10(a), (b), (c), and (d), respectively. The expert delineated bone contour, and the estimated bone boundaries by the 2DSE and 2DOPS methods are overlaid on the B-mode image as shown in Fig. 3.10(e). We see from Fig. 3.10(e) that the bone boundary produced by the 2DOPS method varies sporadically in some places due to the false positive responses. In this case, our 2DSE method also performs poorly as it could not align the produced bone contour with the expert delineated contour on the right side of the image. However, in other places, the 2DSE method performs better and the produced bone contour matches the shape as marked by the expert in the B-mode images (see Figs. 3.10(e)).

### 3.6.3.4 Case 4

Figure 3.11 demonstrates the qualitative bone localization performance comparison of the 2DSE and 2DOPS methods using the volunteer-IV data set. The scanned region, strain image, envelope power map, and the fused map are shown in Figs. 3.11(a), (b), (c), and (d), respectively. The expert delineated bone contour, and the estimated bone boundaries by the 2DSE and 2DOPS methods are

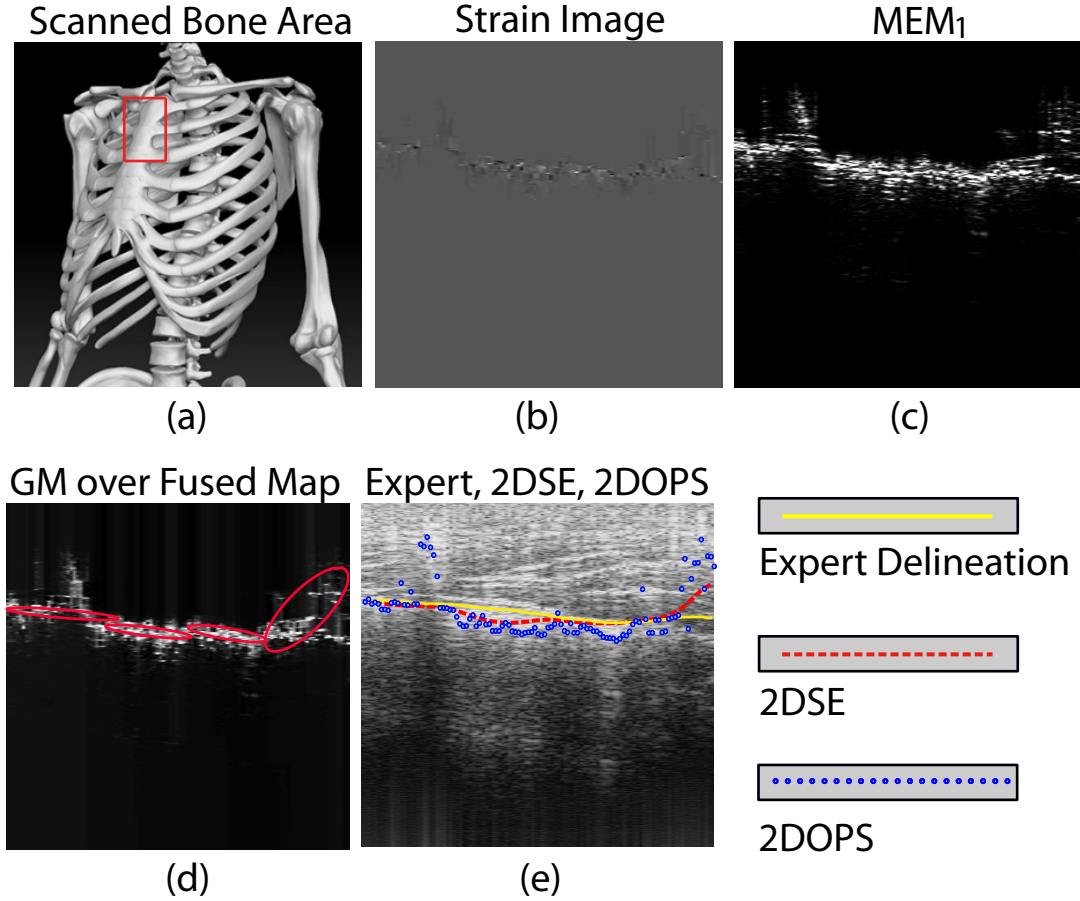


Figure 3.10: Illustration of 2D bone boundary detection using the *in vivo* volunteer-III data set. (a) shows bone region scanned on the volunteer (with red rectangle), (b) is the strain image generated by the proposed approach, (c) is the  $MEM_1$ , and (d) is the fused map with the Gaussian mixtures overlaid. Finally, in (e), orthopaedic expert delineated bone boundary, and detected bone boundary by the 2DOPS and 2DSE methods are overlaid on the B-mode image (bone boundary produced by the 2DOPS method are shown after bottom up ray-casting).

overlaid on the B-mode image as shown in Fig. 3.11(e). We see from Fig. 3.11(e) that the bone boundary produced by the 2DOPS method varies with respect to the expert delineated contour. In contrast, the bone boundary estimated by the 2DSE method better matches the expert delineated contour (see Figs. 3.11(e)). In addition, the 2DSE method does not produce false positives at soft tissue interfaces.

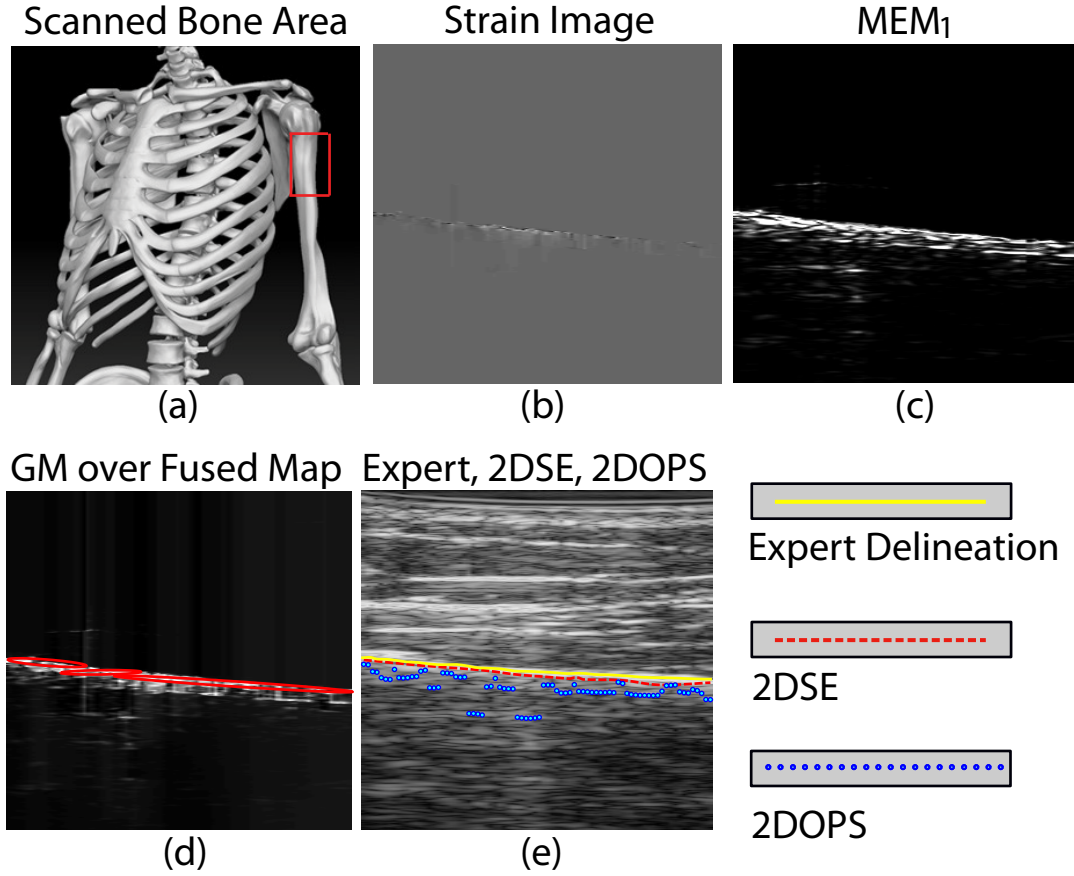


Figure 3.11: Illustration of 2D bone boundary detection using the *in vivo* volunteer-IV data set. (a) shows bone region scanned on the volunteer (with red rectangle), (b) is the strain image generated by the proposed approach, (c) is the MEM<sub>1</sub>, and (d) is the fused map with the Gaussian mixtures overlaid. Finally, in (e), orthopaedic expert delineated bone boundary, and detected bone boundary by the 2DOPS and 2DSE methods are overlaid on the B-mode image (bone boundary produced by the 2DOPS method are shown after bottom up ray-casting).

### 3.6.3.5 Case 5

Finally, we show the qualitative performance comparison of the 2DSE and 2DOPS methods using the volunteer-V data set in Fig. 3.12. The scanned region, strain image, envelope power map, and the fused map are shown in Figs. 3.12(a), (b), (c), and (d), respectively. The expert delineated bone contour, and the estimated bone boundaries by the 2DSE and 2DOPS methods are overlaid on the B-mode image as shown in Fig. 3.12(e). We see from Fig. 3.12(e) that the bone boundary



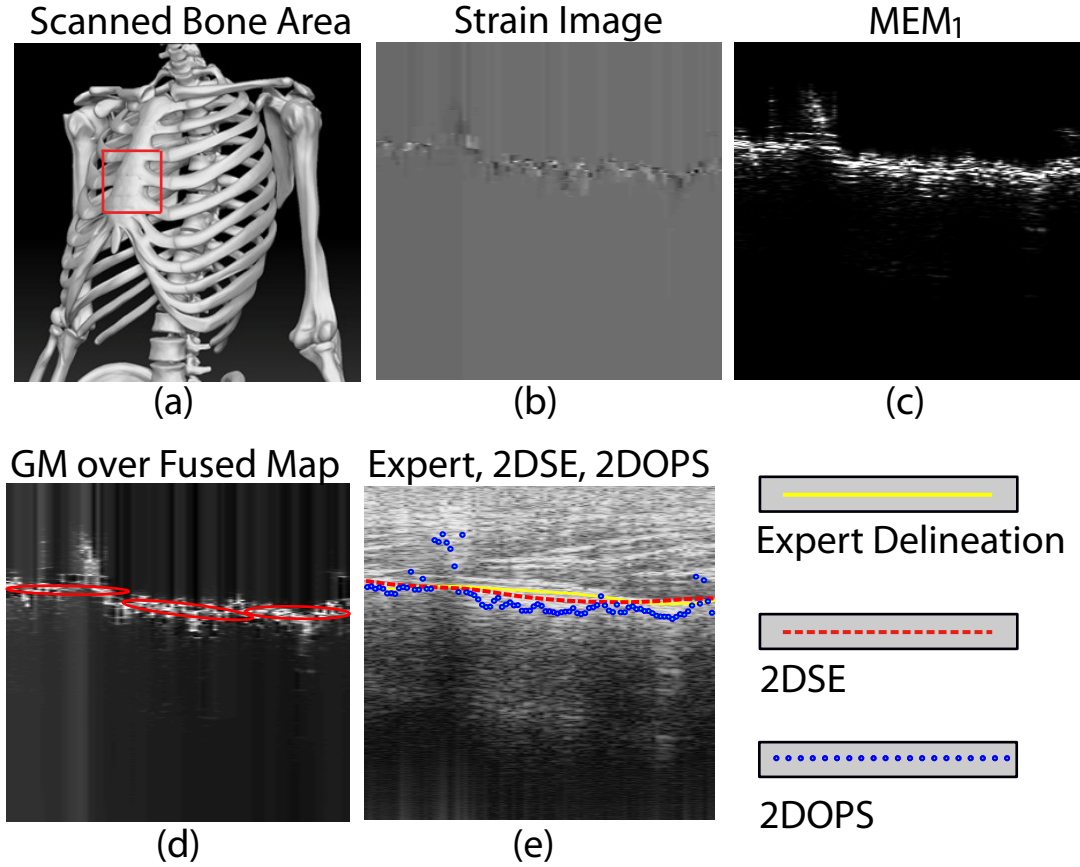


Figure 3.12: Illustration of 2D bone boundary detection using the *in vivo* volunteer-V data set. (a) shows bone region scanned on the volunteer (with red rectangle), (b) is the strain image generated by the proposed approach, (c) is the MEM<sub>1</sub>, and (d) is the fused map with the Gaussian mixtures overlaid. Finally, in (e), orthopaedic expert delineated bone boundary, and detected bone boundary by the 2DOPS and 2DSE methods are overlaid on the B-mode image (bone boundary produced by the 2DOPS method are shown after bottom up ray-casting).

produced by the 2DOPS method varies sporadically in some places due to the false positive responses. In contrary, the 2DSE method performs better and the produced bone contour matches very closely with the shape as marked by the expert in the B-mode images (see Figs. 3.12(e)).



### 3.6.4 Quantitative Comparison

At first we show the individual effect of using the depth-dependent cumulative power, data-driven weight and Gaussian mixture regression in terms of MAE using the *in vivo* data in Table 3.1. To show the effect of using the depth-dependent cumulative power, we choose data sets having satisfactory correlation (i.e.,  $\rho_{avg} \approx 0.90$ ), and used fixed weight (i.e.,  $\lambda = 0.5$ ) and simple linear regression for both the 2DSE and SEP methods (SEP method is described in Chapter 2). While we show the effect of using the data-driven weight, we do not use the depth-dependent cumulative power and use simple linear regression for both the 2DSE and SEP methods. In addition, we use fixed weight (i.e.,  $\lambda = 0.5$ ) for the SEP method. Finally, to show the effect of using the GMR, we use GMR and linear regression separately for the 2DSE method. From Table 3.1, we see that the use of the depth-dependent cumulative power improves the MAE performance by approximately 13% on an average, the use of the data-driven weight improves the MAE performance by approximately 20% on an average, and the use of the GMR improves the MAE performance by approximately 16% on an average.

We also compare the quantitative performance of the 2DSE and 2DOPS methods using the FEM-II, III, and experimental phantoms in terms of MAE in Fig. 3.13 with four different SNR simulations (40, 30, 20, and 10dB) with 100 realizations each. In real clinical settings, SNR of the RF data after beamforming is reported to be approximately 18~22dB [86]. Note that we manually exclude the leakage points in the bone boundaries produced by the 2DOPS method for estimating MAE. As can be seen in Figs. 3.13(a) and (b) for the FEM-II and III, respectively, that the 2DOPS method produces greater mean MAE than that of the 2DSE method although both the methods show a trend of increasing mean MAE with the decrease of SNR. We also see from Fig. 3.13(c) for the experimental phantom that the mean MAE values for the 2DSE method are lower than that of the 2DOPS method at all SNR values.

We also compare the quantitative performance of the 2DSE and 2DOPS methods using the *in vivo* data in terms of mean absolute fitting error in Table 3.2. Here also, we see that our 2DSE method improves the mean absolute fitting error performance by approximately 55% on an average than that of the 2DOPS method.

Table 3.1: Mean absolute error (MAE) Analysis of the individual effects of using the depth-dependent cumulative power (at  $\rho_{avg} \approx 0.90$ ), data-driven weight (at  $\rho_{avg} \approx 0.75$  and  $0.60$ ), and GMR on the *in vivo* data.

Volunteer	MAE at $\rho_{avg} \approx 0.90$ (mm)		MAE at $\rho_{avg} \approx 0.75$ (mm)		MAE at $\rho_{avg} \approx 0.60$ (mm)		MAE for Regression (mm)	
	2DSE	SEP	2DSE	SEP	2DSE	SEP	GMR	Linear
I	0.36	0.43	0.39	0.48	0.44	0.59	0.32	0.36
II	0.43	0.50	0.48	0.59	0.53	0.72	0.35	0.43
III	0.58	0.66	0.64	0.71	0.65	0.82	0.50	0.58
IV	0.39	0.45	0.45	0.53	0.50	0.65	0.29	0.39
V	0.36	0.40	0.40	0.48	0.43	0.58	0.32	0.36

Table 3.2: Mean absolute fitting error (mm) comparisons of the 2DSE and 2DOPS methods using the *in vivo* data.

Volunteer	2DSE (mm)	2DOPS (mm)
I	0.32	0.65
II	0.35	0.92
III	0.50	0.85
IV	0.29	0.80
V	0.32	0.71

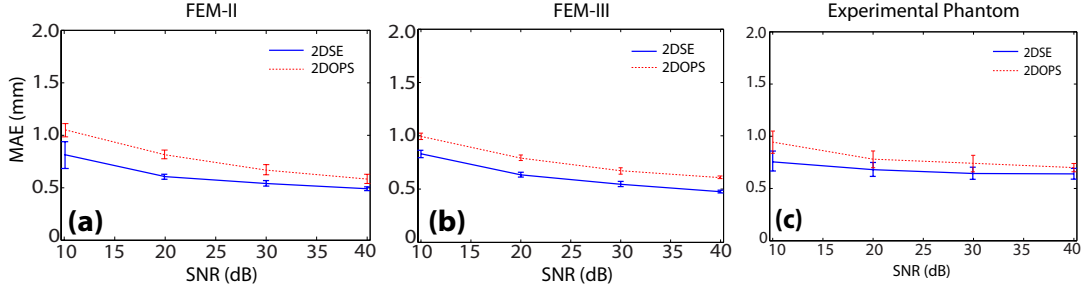


Figure 3.13: MAE (mm) comparisons of the 2DSE and 2DOPS methods at different SNR values using (a) the FEM-II, (b) FEM-III, and (c) experimental phantoms.

Table 3.3: F-Test for the variances in Fig. 3.14.

	2DOPS	2DSE
Mean	5.118	0.896
Variance	8.36967	0.72568
Observations	5	5
Degrees of Freedom	4	4
F	11.5336	
P ( $F \leq f$ ) one-tail	0.01808	
F Critical one-tail	6.38823	

In addition to the mean absolute fitting error, we also show in Fig 3.14 the normalized distributions of the estimated bone boundary points by the 2DOPS and 2DSE methods with respect to the expert delineated bone contours using the *in vivo* volunteer data sets. Although the mean absolute fitting errors for both the methods are below 1mm (Table 3.2), the spread of the signed distances produced by the 2DSE method appears to be lower than those for the 2DOPS method as evident from the standard deviation values of the distributions. To further support this claim, we perform an F-test on the standard deviations of the distributions produced by the 2DOPS and 2DSE methods as shown in Table 3.3. We see in this table that  $F > F$  Critical one-tail, which rejects the null hypothesis: variances for the 2DOPS and 2DSE methods are equal. Thus, the variance for the 2DOPS method is greater than that of the 2DSE method.

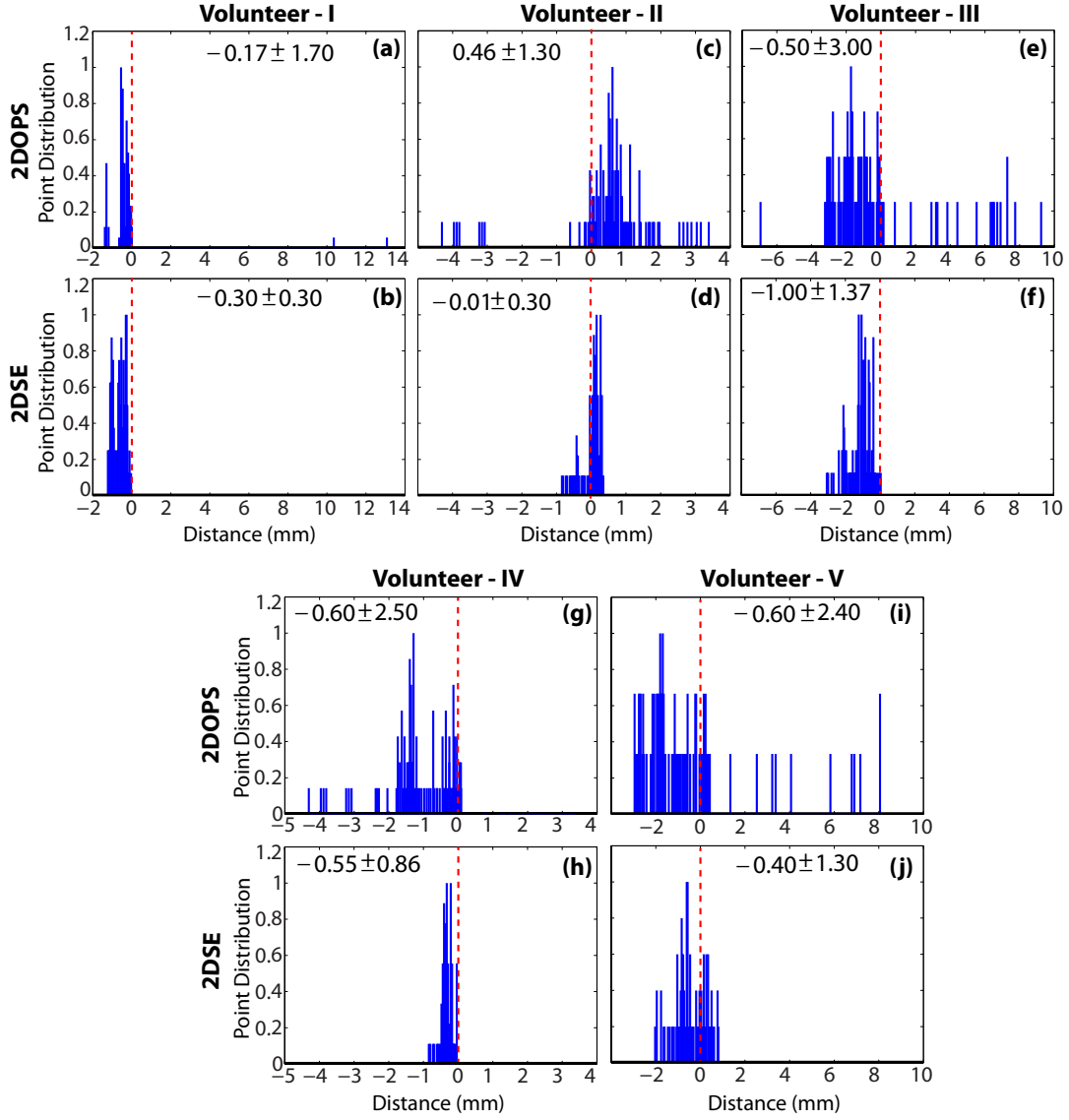


Figure 3.14: Distributions of the estimated bone boundary points by the 2DOPS and 2DSE methods are plotted with respect to the expert delineated bone contours for volunteers-I to -V. The ‘mean  $\pm$  standard-deviation’ of each distribution is shown inside the corresponding plots.

Note that we use Gaussian mixture regression over the maximum intensity points in the fused map, while the bone boundaries produced by the 2DOPS method are found by bottom-up ray casting. To evaluate whether we have introduced a bias by comparing the result following regression with the 2DSE method

with the ray-cast points found in 2DOPS, we also calculated the mean absolute errors for the bone contours produced by applying Gaussian mixture regression to the ray-cast points from the 2DOPS method. Fig. 3.15 shows that the MAE produced by 2DSE is still approximately 28% lower than that produced by GMR applied to the ray-cast points found in the 2DOPS method.

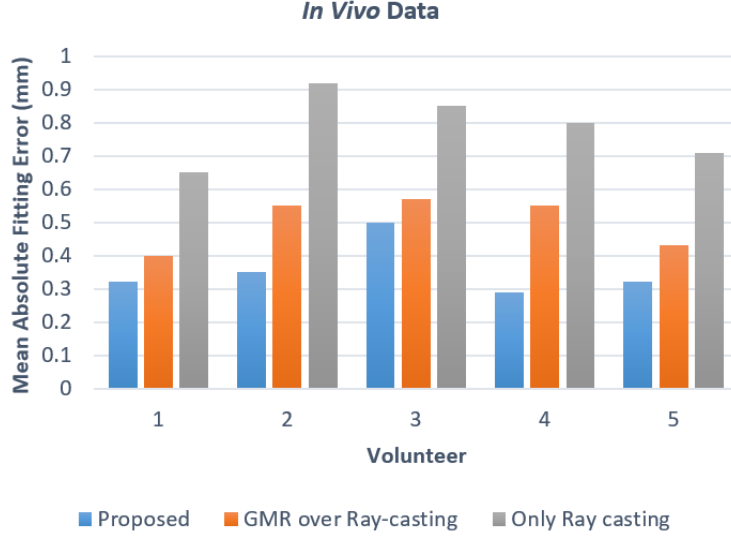


Figure 3.15: Mean absolute fitting error (mm) comparisons of the bone contours produced by using the Gaussian mixture regression over the ray-casted points for the 2DOPS method and the contours produced by the original 2DOPS and proposed methods.

### 3.7 Advantages and Limitations

In this chapter, we improved our previous 2D bone segmentation approach (described in Chapter 2) by incorporating (i) a depth-dependent cumulative power of the envelope into the elastographic data, (ii) an automatic weight estimated from the echo de-correlation measure between the pre- and post-compression RF frames to fuse the strain and envelope power map, (iii) a local statistics-based bone discontinuity detection scheme, and (iv) a non-parametric Gaussian mixture regression to produce smoother yet curvature preserved 2D bone contour. We demonstrated our improved performance on a wide range of validation data including three sets of FEM data, an experimental phantom, and *in vivo* human

data. We achieved an improvements of approximately 19%-20% in the FEM, and 18% in the experimental phantom in terms of MAE when compared with current phase-feature-based state-of-the-art [57]. In addition, we achieved an improvements of approximately 55% in terms of mean absolute fitting error using the *in vivo* data when compared with current phase-feature-based state-of-the-art [57].

Although this study automates the bone segmentation approach that we developed based on combined ultrasound strain-imaging and envelope signal power, however, this approach is limited to 2D images only. 2D methods do not take advantage of correlations between adjacent images (i.e., along the axis perpendicular to the scan plane direction) and are therefore subject to spatial compounding errors as well as errors due to beam thickness effects [56]. Therefore, our next focus is on developing a 3D bone segmentation approach by extending our 2D method. A near-real time 3D elastography technique using 3D probe has been presented by Treece et al. [81] that can generate a 3D strain image, however, this technique has not been validated on clinical *in vivo* data and we found it to be very sensitive to echo de-correlation while acquiring post-compression US volume which limits its applicability.

## Chapter 4

# Strain-initialized Bone Surface Detection in 3D Ultrasound

In this chapter, we discuss our 3D bone surface extraction method using a surface-growing approach that is seeded from the 2D bone contours estimated from combined ultrasound strain-imaging and envelope power which we already described in Chapter 3.

### 4.1 Ultrasound Scanning Protocol

Our scanning protocol has two steps: (1) acquiring 2D pre- and post- compression RF frames,  $I_1$  and  $I_2$ , respectively, (of size  $m \times n$ ) where the US beam direction is perpendicular to the bone surface, and (2) acquiring 3D US RF data (consist  $z$  number of frames) as the transducer sweeps over the target. To implement this protocol, we use a 4D linear array transducer that initially collects a number of 2D US RF frames (axial $\times$ lateral) with free-hand compression while the transducer array is positioned in the middle of its sweep (i.e., in the probe's central plane). Once we are satisfied with the quality of the elastography data, we start acquiring the 3D US data by switching the transducer to the sweeping mode without removing it from the skin surface. The transducer sweeps in the elevation direction. In this step, the user can decrease the field-of-view angle along the elevation direction if scanning a bone with a narrow cross-section (e.g.,

humerus, radius, ulna, etc.).

## 4.2 3D Bone Surface Extraction Using Surface-growing

We modify the 3D B-mode ( $\mathbf{B}$ ) image prior to surface-growing in order to highlight the bone intensities more compared to that of soft tissue region. We estimate the axially cumulative sum of intensities for each voxel as  $P(i, j, k) = \sum_{p_o=1}^i \mathbf{B}(p_o, j, k)^2$ , where  $k$  denote the voxel index in the elevation direction. Using  $P(i, j, k)$ , we estimate the modified B-mode volume as

$$\hat{\mathbf{B}}(i, j, k) = \frac{\mathbf{B}(i, j, k)^{P(i, j, k)}}{\max[\mathbf{B}(i, j, k)^{P(i, j, k)}]}. \quad (4.1)$$

We assume that the 2D seed points  $b_o(i_o, j_o, k_o)$  corresponds to voxels at  $(i_o, j_o, z/2)$ , where  $k_o \approx z/2$ . Then the bone surface expands frame-wise along the elevation direction by minimizing the cost function defined as

$$C(i, j_o, k_o \pm 1) = \sum_{j_v=j_o-L_y}^{j_o+L_y} [E_i(i, j_o, k_o \pm 1) + \kappa E_s(i, j_o, k_o \pm 1)] \times e^{-|j_o-j_v|}, \quad (4.2)$$

where  $E_i$  and  $E_s$  are the energy functions associated with the new candidate voxel,  $\kappa$  is the mixing weight, and  $L_y$  is the lateral voxel number upon which the exponential weight spans to regularize  $C$  in the  $y$  direction. Energy  $E_i$  ensures that the new surface voxel at  $(j_o, k_o \pm 1)$  carries the highest intensity value among the voxels in the interrogated scan-line, and is defined as

$$E_i(i, j_o, k_o \pm 1) = \frac{1 - [\hat{\mathbf{B}}(i, j_o, k_o \pm 1) - \mu_t]^2 - [\hat{\mathbf{B}}(i, j_o, k_o \pm 1) - \mu_b]^2}{\max[1 - [\hat{\mathbf{B}}(i, j_o, k_o \pm 1) - \mu_t]^2 - [\hat{\mathbf{B}}(i, j_o, k_o \pm 1) - \mu_b]^2]}, \quad (4.3)$$

where

$$\mu_t = \frac{1}{i_t - 1} \sum_{a=1}^{i_t-1} \hat{\mathbf{B}}(a, j_o, k_o \pm 1), \quad (4.4)$$



$$\mu_b = \frac{1}{m - i_b} \sum_{a=i_b+1}^m \hat{\mathbf{B}}(a, j_o, k_o \pm 1), \quad (4.5)$$

$[i_t, i_b]$  is the axial search range for a new surface candidate centered at  $i_o$ . In addition, the energy function  $E_s$  ensures a smooth transition between the seed and new candidate voxel, and is defined as

$$E_s(i, j_o, k_o \pm 1) = \frac{(|i_o - i|/|i_o - i_t|)^2}{\max[ (|i_o - i|/|i_o - i_t|)^2 ]}. \quad (4.6)$$

Finally, we estimate the location of a new bone surface voxel from Eq. (4.2) for the frame at  $k_o \pm 1$  as

$$i_o |_{k_o \pm 1} = \arg \min_i \{C(i, j_o, k_o \pm 1)\}. \quad (4.7)$$

We update  $i_o |_{k_o \pm f}$  as the new seed voxel, proceed to the next frame at  $k_o \pm (f+1)$ , where  $f = 1, 2, 3..$ , and continue growing until  $\min[C]$  rises to a value that makes it unlikely that the next voxel still represents bone. In our analyses, we set this threshold empirically at a value of 0.8; we plan to revisit this choice in future.

## 4.3 Validation Setup

### 4.3.1 Simulated Phantom

We built a 40mm×40mm×20mm (axial×lateral×elevation) FEM phantom using the analysis software ANSYS (ANSYS, Inc., Canonsburg, PA) and the ultrasound simulation software Field II [87]. The phantom mimicked a 3D US scan of the human distal radius bone with a total number of 2,207,200 nodes. The stiffness of the homogeneous soft tissue and bone regions were set to 10kPa and 10GPa, respectively, as previously reported [88]. Our phantom was compressed in the lateral direction from the top using a planar compressor that was wider than the phantom. We set an applied pressure level that corresponds to 1% average strain. At first we acquired 2D elastographic data along lateral direction. Then we acquired 3D ultrasound data using a phased array transducer that swept both the sides of the 2D frame along the elevation direction. An ultrasonic transducer of center frequency,  $f_0 = 5\text{MHz}$  and band-width = 50% was used to simulate the

phantom scan from the top. The total number of scan lines was set to 128 and 64 in the lateral and elevation directions, respectively. The resulting voxel size of the 3D data was  $0.015\text{mm} \times 0.3\text{mm} \times 0.3\text{mm}$ . The B-mode image of the phantom is shown in Fig. 4.1(a).

### 4.3.2 Experimental Phantom

We constructed an experimental phantom using a radio-opaque Sawbones hemipelvis (Sawbones, Pacific Research Laboratories, Inc., Vashon Island, WA), model number 1297-22. A portion of the pelvis was suspended in polyvinyl chloride (PVC) gel (see Fig. 2.1(a)) and placed in an acrylic tube (see Fig. 2.1(b)). A high resolution peripheral quantitative CT machine, model HR pQCT Xtreme CT (Scanco USA, Inc., Wayne, PA) was used to acquire a single  $482 \times 482 \times 402$  (lateral  $\times$  axial  $\times$  elevation) volume with a resolution of  $0.25\text{mm} \times 0.25\text{mm} \times 0.25\text{mm}$ . The US images were acquired using a SonixRP (Ultrasonix Medical Corporation, Richmond, BC) scanner in the Center for Hip Health and Mobility, Vancouver Coastal Health Authority, Vancouver, BC, Canada. We used a 4DL14-5/38 linear 4D array probe operating at 5MHz for collecting data for the 3D implementations.

### 4.3.3 *In Vivo* Data

We acquired three sets of *in vivo* data from three volunteers (volunteer-I: 27-year old male; volunteer-II: 26-year old male; volunteer-III: 29-year old male) after obtaining prior consent. All data were acquired with free-hand compression. The US images were acquired using a SonixRP (Ultrasonix Medical Corporation, Richmond, BC) scanner in the Center for Hip Health and Mobility, Vancouver Coastal Health Authority, Vancouver, BC, Canada. We used a 4DL14-5/38 linear 4D array probe operating at 5MHz for collecting data for the 3D implementations, respectively. The study was approved by the UBC clinical research ethics board.

## 4.4 Results

We provide comparative results of our proposed 3D bone detection (3DSE) methods with the previously reported volume-specific parameter optimized 3D local

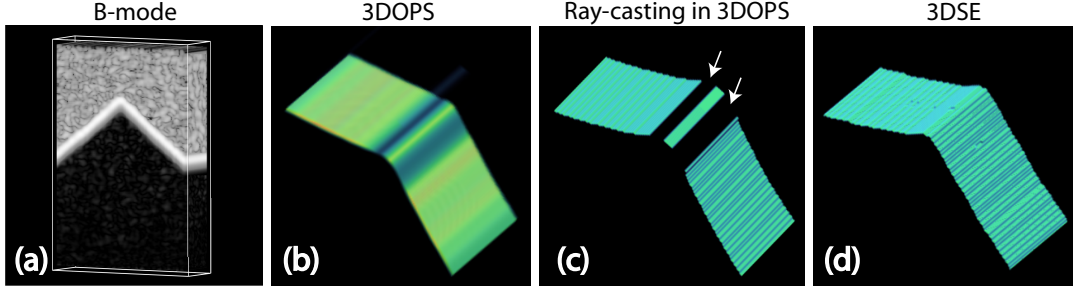


Figure 4.1: Illustration of the FEM results. (a) B-mode image, (b) estimated 3D phase symmetry image by the 3DOPS method, (c) bone surface after bottom up ray-casting in (b) (arrows show leakage), and (d) estimated bone surface by the proposed method.

phase feature-based bone segmentation (3DOPS) [59] method using the FEM phantoms, experimental phantom and *in vivo* data. The 3DOPS method selects parameters automatically for the Log-Gabor filters based on properties estimated directly from the specific US image that is being analyzed. We calculate mean absolute error (MAE) which is defined as

$$\text{MAE} = \frac{1}{P \times Q} \sum_{p=1}^P \sum_{q=1}^Q |A(p, q) - G(p, q)|, \quad (4.8)$$

where  $P$  and  $Q$  represent the number of data points spanned by the bone boundary in the lateral and elevation directions, respectively,  $A$  is a matrix containing the ‘ground truth’ bone boundary points, and  $G$  is a matrix containing the estimated bone boundary points. As ground truth, we used the bone geometry defined for Field II simulation for the FEM, the estimated bone boundary from the computed tomography (CT) image for the experimental phantom, and expert delineation of bone boundaries on B-mode images for the *in vivo* data. We use fiducial-based CT and US bone alignment before estimating the MAE for the experimental phantom. Note that we use bottom-up ray casting in the phase-symmetry images for the 2DOPS and 3DOPS methods to get  $G$  as suggested in [59]. In our surface-growing technique, we set parameters as  $i_o - i_t \approx 5\text{mm}$ ,  $L_y = 3$  and  $\kappa = 0.5$ .

#### 4.4.1 FEM Results

We provide comparative qualitative results of our proposed 3DSE and the 3DOPS methods using the FEM data in Fig. 4.1. Note that the 3DOPS method uses bottom up ray-casting in the 3D phase symmetry image to produce final bone surface; this can produce “leakage” through weak areas of the phase symmetry volumes. As an evident, we see that the ray-casting leaks through weak spots in the phase symmetry image (shown with white arrows in Fig. 4.1(c)). In contrast, the bone boundary produced by the proposed method (Fig. 4.1(d)) appears to be free of such artifacts.

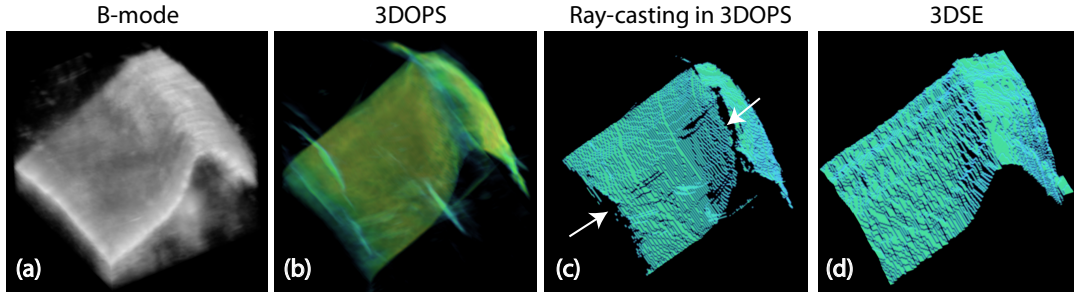


Figure 4.2: Illustration of the experimental phantom results. (a) B-mode image, (b) estimated 3D phase symmetry image, (c) bone surface after bottom up ray-casting in (b) (arrows show leakage), and (d) estimated bone surface by the proposed method.

#### 4.4.2 Experimental Phantom Results

Figure 4.2 demonstrates the performance comparison of the proposed 3DSE and 3DOPS methods using the experimental phantom. Here also we see that the ray-casting leaks through weak spots (indicated with white arrows in Fig. 4.1(c)) in the 3D phase symmetry image (see Fig. 4.1(b)). In contrast, the bone surface estimated by the proposed method has no discontinuity (see Fig. 4.1(d)).

#### 4.4.3 *In Vivo* Results

We show the bone surface detection performance of the proposed 3DSE and 3DOPS methods on three cases of volunteer *in vivo* data.

#### 4.4.3.1 Case 1

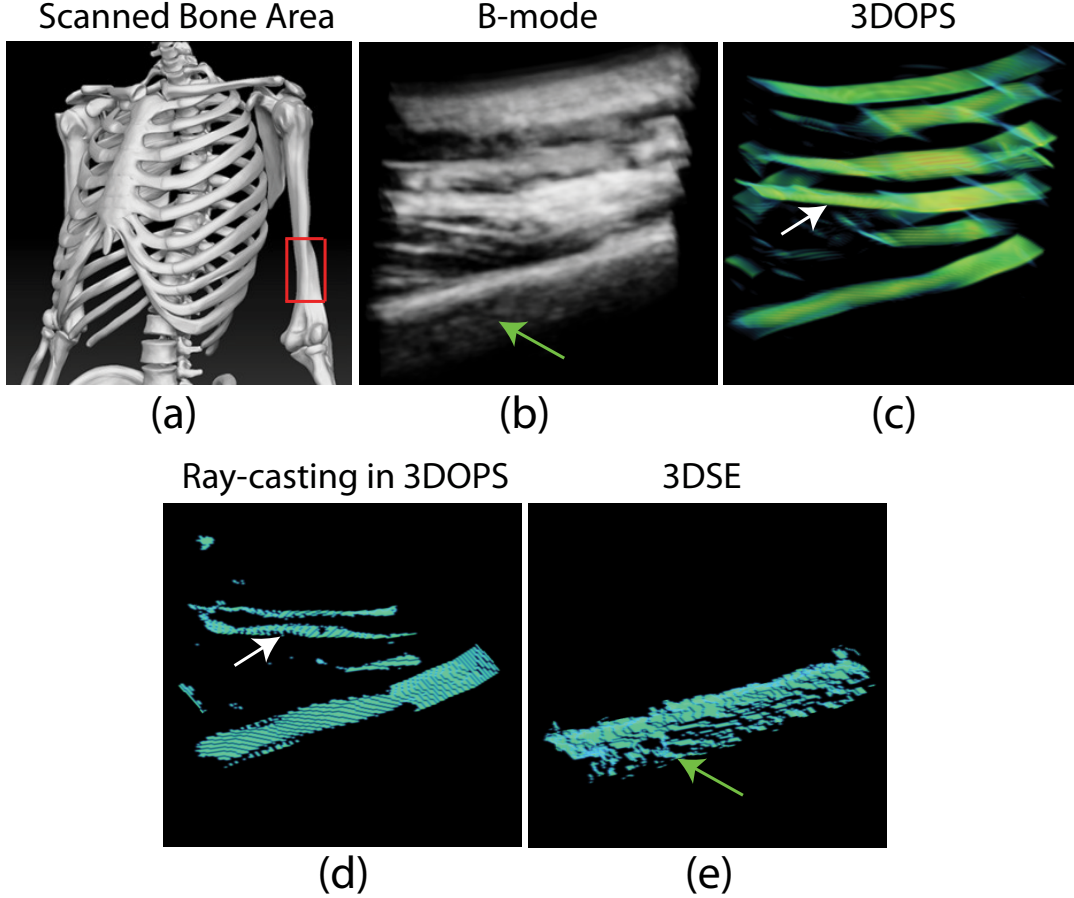


Figure 4.3: Illustration of the 3D bone surface detection using the *in vivo* volunteer-I data set. (a) shows bone region scanned on the volunteer (with red rectangle), (b) is the B-mode image, (c) shows the estimated 3D phase symmetry image by the 3DOPS method, (d) shows the bone surface after bottom up ray-casting in (c), and (e) shows the estimated bone surface by the 3DSE method.

We show the qualitative performance comparison of the 3DSE and 3DOPS methods using the volunteer-I data set in Fig. 4.3. The scanned region, B-mode image, 3D phase symmetry image, ray-casted version of the phase symmetry image, and bone surface produced by the 3DSE method are shown in Figs. 4.3(a), (b), (c), (d), and (e), respectively. We see in Fig. 4.3(c) that the 3DOPS method produces false positive responses in the soft tissue interfaces (shown with white

arrows). We also see in Figs. 4.3(d) that the ray-casting results in leaks through weak responses on the bone surface and instead detects false positive soft tissue interfaces (shown with corresponding white arrows in Figs. 4.3(c) and (d)). In contrast, the bone surfaces estimated by the 3DSE method better match the shapes visible in the corresponding B-mode images (see Figs. 4.3(b) and (e)). In addition, our method successfully extracts the bone surfaces that are not perpendicular to the US beam direction (shown with corresponding green arrows in Figs. 4.3(b) and (e)). In contrast, the 3DOPS method fails to extract these curved bone regions.

#### 4.4.3.2 Case 2

Figure 4.4 demonstrates the qualitative performance comparison of the 3DSE and 3DOPS methods using the volunteer-II data set. The scanned region, B-mode image, 3D phase symmetry image, ray-casted version of the phase symmetry image, and bone surface produced by the 3DSE method are shown in Figs. 4.4(a), (b), (c), (d), and (e), respectively. We see in Fig. 4.4(c) that the 3DOPS method produces false positive responses in the soft tissue interfaces (shown with white arrows). We also see in Figs. 4.4(d) that the ray-casting results in leaks through weak responses on the bone surface and instead detects false positive soft tissue interfaces (shown with corresponding white arrows in Figs. 4.4(c) and (d)). In contrast, the bone surfaces estimated by the 3DSE method better match the shapes visible in the corresponding B-mode images (see Figs. 4.4(b) and (e)).

#### 4.4.3.3 Case 3

Finally, in Fig. 4.5, we demonstrate the qualitative performance comparison of the 3DSE and 3DOPS methods using the volunteer-II data set. The scanned region, B-mode image, 3D phase symmetry image, ray-casted version of the phase symmetry image, and bone surface produced by the 3DSE method are shown in Figs. 4.5(a), (b), (c), (d), and (e), respectively. We see in Fig. 4.5(c) that the 3DOPS method produces false positive responses in the soft tissue interfaces (shown with white arrows). We also see in Figs. 4.5(d) that the ray-casting results in leaks through weak responses on the bone surface and instead detects

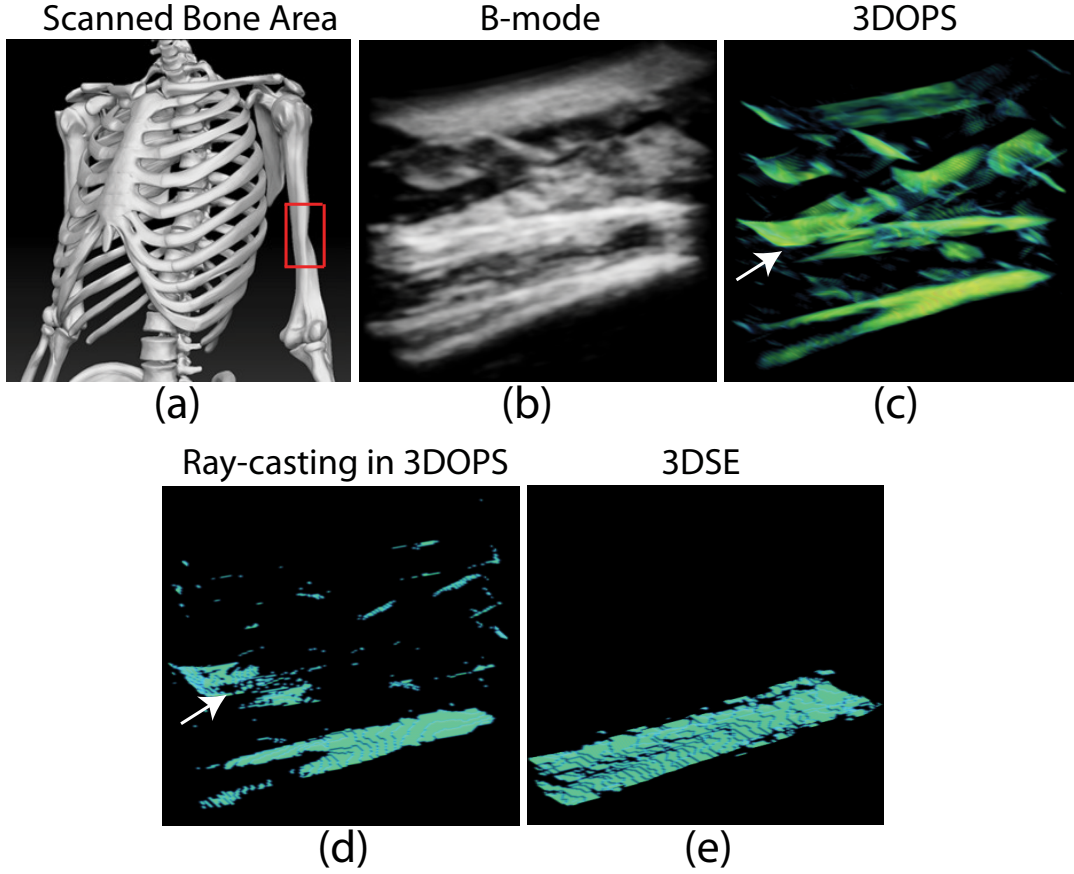


Figure 4.4: Illustration of the 3D bone surface detection using the *in vivo* volunteer-I data set. (a) shows bone region scanned on the volunteer (with red rectangle), (b) is the B-mode image, (c) shows the estimated 3D phase symmetry image by the 3DOPS method, (d) shows the bone surface after bottom up ray-casting in (c), and (e) shows the estimated bone surface by the 3DSE method.

false positive soft tissue interfaces (shown with corresponding white arrows in Figs. 4.5(c) and (d)). In contrast, the bone surfaces estimated by the 3DSE method better match the shapes visible in the corresponding B-mode images (see Figs. 4.5(b) and (e)). In addition, like case 1, our method successfully extracts the bone surfaces that are not perpendicular to the US beam direction (shown with corresponding green arrows in Figs. 4.5(b) and (e)). In contrast, the 3DOPS method fails to extract these curved bone regions. However, very few false positives are produced by the 3DSE method in this case as indicated with

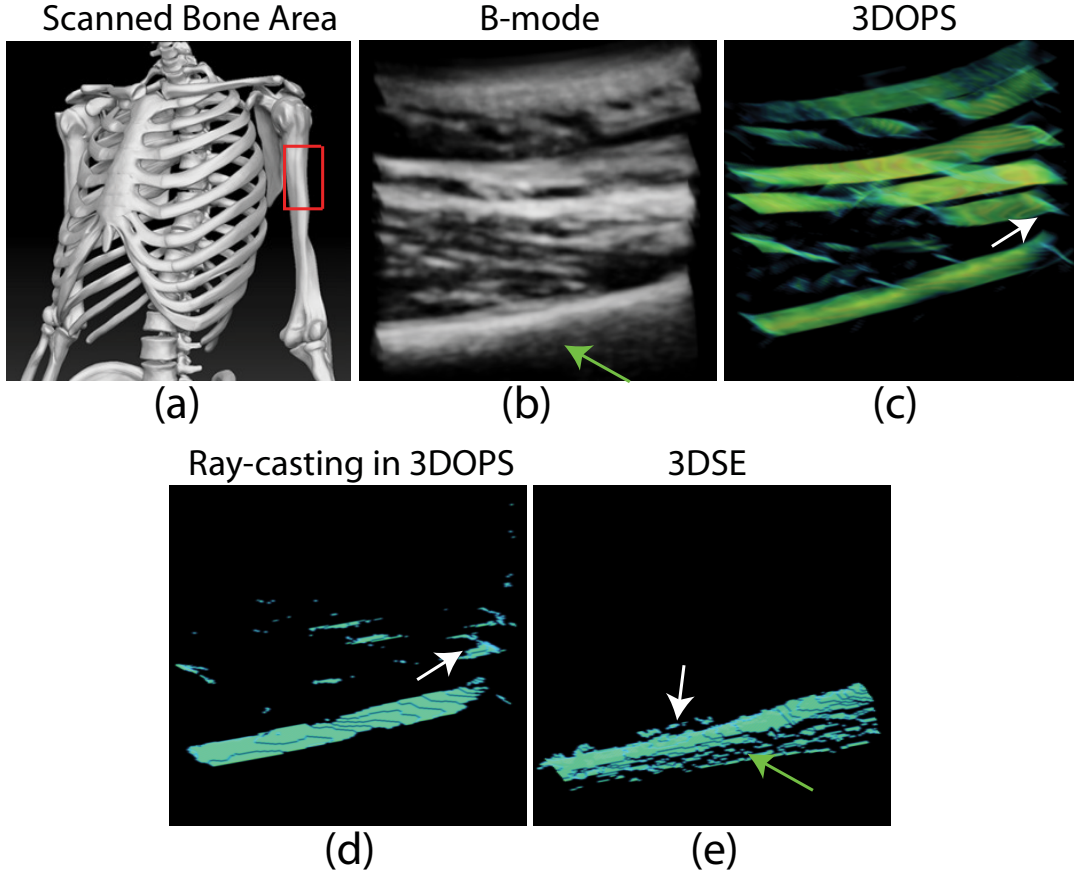


Figure 4.5: Illustration of the 3D bone surface detection using the *in vivo* volunteer-I data set. (a) shows bone region scanned on the volunteer (with red rectangle), (b) is the B-mode image, (c) shows the estimated 3D phase symmetry image by the 3DOPS method, (d) shows the bone surface after bottom up ray-casting in (c), and (e) shows the estimated bone surface by the 3DSE method.

the white arrow in Fig. 4.5(e).

#### 4.4.4 Quantitative Validation

We estimate the MAE for the FEM and experimental phantom with four different signal-to-noise ratio (SNR) simulations (40, 30, 20, and 10dB) with 100 realizations each. In real clinical settings, SNR of the RF data after beamforming is reported to be approximately 18~22dB [86]. We also estimate the Matlab(R) execution time for the *in vivo* data running in Intel(R) Xeon(R) CPU E3 @ 3.20GHz,



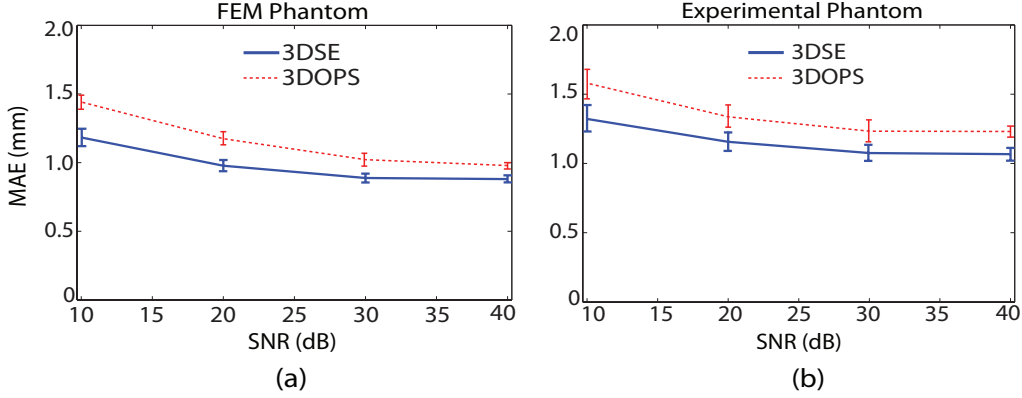


Figure 4.6: MAE analysis of the 3DSE and 3DOPS methods at different SNRs using (a) the FEM and (b) experimental phantom data.

Table 4.1: Computation time in second for a volume size of  $364 \times 110 \times 50$  voxels.

Volunteer	3DSE	3DOPS
I	5.5	103.0
II	5.9	105.6
III	6.0	108.7

Memory: 8GB in Table 4.1. Note that we use the bone surfaces produced by the 3DOPS method after ray-casting in the MAE analysis after manually excluding leakage regions. Nonetheless, we see in Figs. 4.6(a) and (b) that for all SNR values, the mean MAE for the our method is lower than that of the 3DOPS method. In addition, the Table 4.1 shows that the execution times for the 3DSE method are approximately 18 times smaller than those of the 3DOPS method for all three *in vivo* data sets.

We also show computation time diagrams in Fig. 4.7 that illustrate the run times of different components of the 3DOPS and 3DSE methods. Although a GPU-based implementation of a version of the 3DOPS method is reported which takes 0.8sec for its execution [79], this time refers solely to the core log-Gabor convolution and presumes that all parameters are already pre-selected. In the full 3DOPS method [59], all the parameters are automatically estimated using a process in which the core log-Gabor convolution, implemented in Mat-

lab(R), is performed iteratively over 50 times to select the optimum parameters. These repeated iterations are performed in the (a) filter scale selection, (b) filter orientation refinement, and (c) filter angular band-width selection blocks in Fig. 4.7(a). If the GPU-based implementation were incorporated in the current 3DOPS method, the overall run-time, including automatic optimization, would be approximately 1min, compared with  $\sim 5$ s for the 3DSE method. If both components of the proposed 3DSE method were implemented in GPU, we anticipate that we could reduce the run time to near real-time.

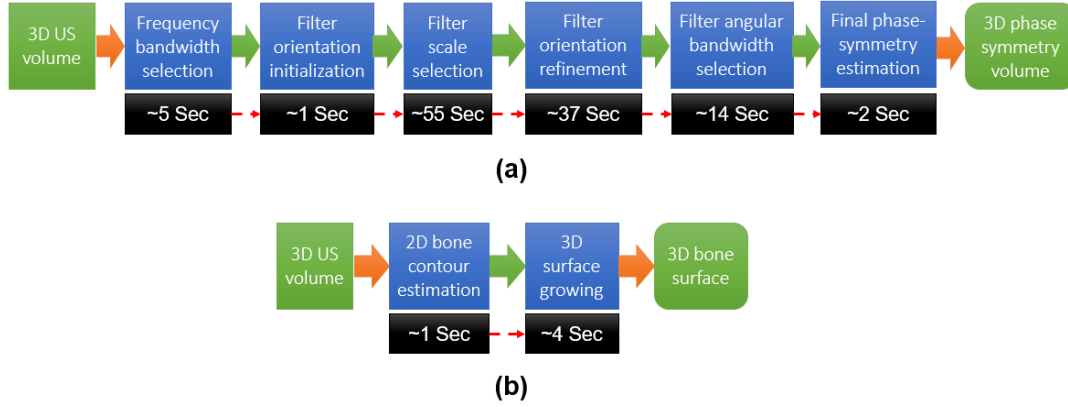


Figure 4.7: Diagrams showing the computation time breakdown for different components of the (a) 3DOPS and (b) 3DSE methods.

## 4.5 Advantages and Limitations

In this chapter, we extend our 2D bone contour into a 3D bone surface by using a surface-growing-based approach. We demonstrated our improved performance on a wide range of validation data including a FEM, an experimental phantom, and *in vivo* human data with reported improvements of approximately 20% and 23% in terms of MAE and 18 times in terms of computation time, respectively, when compared with current state-of-the-art.

However, we used some empirical parameters in our 3D implementation, i.e.,  $i_o - i_t$ ,  $L_y$  and  $\kappa$ . We plan to investigate this promising study further to make these parameters data driven so that this method becomes fully automatic.

# Chapter 5

## Conclusions

### 5.1 The Impact and Potential Clinical Application

We have proposed novel methods for robust bone boundary localizations based on the fusion of strain imaging and envelope signal power detection for 2D US images as well as surface-growing-based bone segmentation in 3D US volumes. We have combined real-time strain imaging based on an analytic minimization of regularized cost functions with an envelope power map of the pre-compression RF frame. Our results have demonstrated reduced bone localization error through a better elastogram resolution, adoption of an envelope power map of higher dynamic range, addressing the false positive bone response, and exploiting the smoothing feature of the AM method to better delineate the bone boundary in strain images. We have also developed an effective way to perform 3D bone surface extraction using a surface growing approach that is seeded from 2D bone contours estimated from combined ultrasound strain imaging and envelope power. We have demonstrated our improved performance on a wide range of validation data, including three sets of FEM data, an experimental phantom, and *in vivo* human data. We have achieved improvements of approximately 20% on both the 2D and 3D FEM, 18% on the 2D experimental phantom, and 23% on the 3D experimental phantom in terms of MAE when compared with current phase-features-based method [57]. In addition, we have achieved improvements of approximately 55% on the 2D *in*

*vivo* data in terms of mean absolute fitting error when compared with current phase-features-based state-of-the-art technique [57]. We have also performed 3D bone segmentation in *in vivo* data approximately 18 times faster than that of the current state-of-the-art method [59].

Our laboratory believes that 3D US has great potential to assist orthopaedic care, especially during surgeries, if the anatomical structures of interest can be localized and visualized with sufficient accuracy and clarity and in a highly automated and rapid manner [95]. Our laboratory has validated its 3D-local-phase-feature-based US segmentation technique on scans obtained from 29 trauma patients with distal radius and pelvic ring fractures, and achieved an average surface fitting error of  $0.62 \pm 0.42$  mm for pelvic patients and  $0.21 \pm 0.14$  mm for distal radius patients. As we have demonstrated in this thesis, our method has achieved better accuracy in bone localizations than the state-of-the-art image-phase-based method, and we hope that our method will likewise perform at a higher quality level than the former in more challenging situations. Since our method is based on the tissue stiffness estimation, it is expected to be robust in bone localization in a challenging situation when ligament/tendon appears in between the transducer face and bone surface. However, our method might produce false positives in a rare situation when ligament is ossified and low strain profiles are produced along the ligament-soft tissue layers similar to bone-soft tissue layers.

Accordingly, we believe that our proposed method may have numerous clinical applications. The method can be used to assess bone fractures, diagnose bone deformities, and guide computer-assisted orthopedic surgery. However, because it requires applying some pressure to the probe to generate the strain image, it would be difficult to apply in situations in which the patient is awake and unable to tolerate pressure to an injury site.

## 5.2 Thesis Contributions

The goal of our work was to contribute some effective methods for robust bone segmentation in ultrasound images that would ultimately address some of the challenging limitations of the previously reported bone segmentation methods. This research was intended to further advance the larger goal of developing a

novel 3D ultrasound-based CAOS system. To this end, we have contributed the following to this project:

1. We have shown the potential of combined US strain-imaging and envelope power signaling to delineate bone boundaries in US images. Our method uses real-time strain imaging [82] based on an analytic minimization of regularized cost functions to delineate bone from tissue stiffness maps and, thus, we have achieved a marked reduction in the number of false positive bone responses at the soft tissue interface.
2. We have introduced automatic parameter selection processes to make our 2D bone segmentation method more robust and self-tuning. We have introduced the depth-dependent cumulative power of the envelope into the pre- and post-compression data, which we reveal to reduce the number of soft tissue related artifacts in the resulting strain images.
3. We have incorporated a data-driven weight into our method, estimated from the echo de-correlation measurements as being between the pre- and post-compression RF frames, which controls the contribution of strain images in the resulting fused map. We have also employed local statistics-based bone discontinuity detection scheme.
4. We have introduced Gaussian mixture regression, a more flexible multivariate non-parametric regression model that better preserves the curvature features at the bone boundary than the parametric linear regression model.
5. We have developed a method for 3D bone surface extractions using a surface growing approach that is seeded from the 2D bone contours estimated from combined ultrasound strain imaging and envelope power. The 2D seed bone contour grows into the 3D surface by minimizing a combined intensity similarity and a voxel proximity-based cost function.

### **5.3 Remaining Challenges and Future Work**

The bone segmentation algorithm presented in this thesis is one of the components of an ultrasound guided CAOS system to assist surgeons during orthopedic

surgery. We have demonstrated in this thesis that the proposed segmentation methods are accurate, rapid and robust. However, the slowest portion of the method is, currently, the 3D segmentation runtime. Therefore, we plan to implement the 3D bone segmentation algorithm in C++ and run it on a graphics processing unit (GPU) to accelerate the runtime. The current runtime for 3D bone segmentation in MATLAB(R) is  $\sim 5$  seconds and we hope to achieve an improvement factor of at least 500x after the code is optimized. While we have demonstrated excellent robustness and accuracy in our initial phantom and short clinical study, there remains room for improvement to cope with the challenging clinical data sets.

Although all of the parameters in our 2D bone segmentation method are data-driven, our 3D bone segmentation method still has three free parameters: the search region  $i_o - i_t$ , the lateral regularization distance,  $L_y$ , and the weight of the fusing energy function,  $\kappa$ . In our future work, we plan to investigate the possible approaches to having these parameters become automatically selected.

Finally, we plan to perform two advanced validation tests of our proposed segmentation methods before they are considered to be fully capable of being incorporated into surgery environments. Thus,

1. We plan to perform a laboratory-based simple fracture realignment procedure, using a bovine long bone (e.g., femur) specimen, and assess the accuracy of the bone localization as well as its fracture realignment performance.
2. Latter, we plan to perform a surgical tool navigation performance procedure utilising a human/animal cadaver, and to assess the accuracy of the bone and surgical tool tip localization.

In the long run, we hope to see this work employed in the ultrasound guided CAOS system, with the goal of minimizing radiation time and the degree of possible surgical error during orthopedic surgeries.

# Bibliography

- [1] P. Marhofer and V. W. Chan, “Ultrasound-guided regional anesthesia: current concepts and future trends,” *Anesthesia & Analgesia*, vol. 104, no. 5, pp. 1265–1269, 2007.
- [2] “X-ray (wikipedia),” <http://en.wikipedia.org/wiki/X-ray>, accessed: 2015-05-15.
- [3] “Nutek medical centre,” <http://www.nutekmedicalcentremumbai.com/>, accessed: 2015-05-15.
- [4] “X-ray computed tomography (wikipedia),” [http://en.wikipedia.org/wiki/X-ray\\_computed\\_tomography](http://en.wikipedia.org/wiki/X-ray_computed_tomography), accessed: 2015-05-15.
- [5] “Computerised axial tomography (CAT or CT),” [http://www.schoolphysics.co.uk/age16-19/Atomic%20physics/X%20rays/text/CAT\\_scanning/index.html](http://www.schoolphysics.co.uk/age16-19/Atomic%20physics/X%20rays/text/CAT_scanning/index.html), accessed: 2015-05-15.
- [6] “New paradigm in GPU-based monte carlo simulations for X-ray CT imaging doses,” [http://www.rpi.edu/dept/radsafe/public\\_html/GPU\\_project/index\\_GPU.html](http://www.rpi.edu/dept/radsafe/public_html/GPU_project/index_GPU.html), accessed: 2015-05-15.
- [7] “Philips,” <http://www.healthcare.philips.com/main/products/mri/systems/achieva3t/>, accessed: 2015-05-15.
- [8] “Online image arcade,” <http://imgarcade.com/1/magnetic-resonance-imaging-diagram/>, accessed: 2015-05-15.
- [9] “Fluoroscopy & digital photospot,” <http://www.upstate.edu/radiology/education/rsna/fluoro/fluoro.php>, accessed: 2015-05-15.

- [10] “Fluoroscopy (wikipedia),” <http://en.wikipedia.org/wiki/Fluoroscopy>, accessed: 2015-05-15.
- [11] B. A. Schueler, “The AAPM/RSNA physics tutorial for residents general overview of fluoroscopic imaging,” *Radiographics*, vol. 20, no. 4, pp. 1115–1126, 2000.
- [12] “Color doppler ultrasound scanner,” <http://www.lhdz.org/vet/ultrasound-op480.htm>, accessed: 2015-05-15.
- [13] “MAB001 digital portable cheapest ultrasound scanner,” [http://www.mayamed.cn/product/1298666144-213160187/MAB001\\_Digital\\_portable\\_cheapest\\_ultrasound\\_scanner.html](http://www.mayamed.cn/product/1298666144-213160187/MAB001_Digital_portable_cheapest_ultrasound_scanner.html), accessed: 2015-05-15.
- [14] “How ultrasound imaging works explained simply,” [http://www.howequipmentworks.com/ultrasound\\_basics/](http://www.howequipmentworks.com/ultrasound_basics/), accessed: 2015-05-15.
- [15] C. Otto, “Principles of echocardiographic image acquisition and Doppler analysis,” *Otto CM: Textbook of clinical echocardiography*. WB Saunders, Philadelphia, pp. 1–3, 2000.
- [16] “Overview of the smart materials technology,” [http://resources.edb.gov.hk/physics/articleIE/smartmaterials/SmartMaterials\\_e.htm](http://resources.edb.gov.hk/physics/articleIE/smartmaterials/SmartMaterials_e.htm), accessed: 2015-05-15.
- [17] “Basic principle of medical ultrasonic probes (transducer),” <http://www.ndk.com/en/sensor/ultrasonic/basic02.html>, accessed: 2015-05-15.
- [18] J. E. Aldrich, “Basic physics of ultrasound imaging,” *Critical care medicine*, vol. 35, no. 5, pp. S131–S137, 2007.
- [19] S. N. Narouze, *Atlas of ultrasound-guided procedures in interventional pain management*. Springer Science & Business Media, 2010.
- [20] “Ultrasound physics,” <http://www.nysora.com/mobile/regional-anesthesia/foundations-of-us-guided-nerve-blocks-techniques/3084-ultrasound-physics.html>, accessed: 2015-05-15.



- [21] J. Bercoff, *Ultrafast ultrasound imaging*. INTECH Open Access Publisher, 2011.
- [22] “Studyblue,” <https://www.studyblue.com/notes/n/hubs/deck/7055337>, accessed: 2015-05-29.
- [23] “What does this image of the hip display?” <http://www.aium.org/soundwaves/article.aspx?aId=666&iId=20130912>, accessed: 2015-05-15.
- [24] “Clinical implications of the echo enhancement artifact in volume sonography of the uterus,” <http://www.jultrasoundmed.org/content/25/11/1431/F5.expansion>, accessed: 2015-05-15.
- [25] “Artefacts on musculoskeletal ultrasound,” <https://theultrasoundsite.co.uk/artefacts-musculoskeletal-ultrasound/>, accessed: 2015-05-15.
- [26] “Pathology of the shoulder,” <http://shoulderultrasound.com/973/1036.html>, accessed: 2015-05-15.
- [27] “Basic physics of digital radiography/the image receptor,” [http://en.wikibooks.org/wiki/Basic\\_Physics\\_of\\_Digital\\_Radiography/The\\_Image\\_Receptor](http://en.wikibooks.org/wiki/Basic_Physics_of_Digital_Radiography/The_Image_Receptor), accessed: 2015-05-15.
- [28] W. Xu and S. T. Salcudean, “Enhancement of bone surface visualization using ultrasound radio-frequency signals,” in *Ultrasonics Symposium, 2007. IEEE*. IEEE, 2007, pp. 2535–2538.
- [29] M. A. Hussain, A. Hodgson, and R. Abugharbieh, “Robust bone detection in ultrasound using combined strain imaging and envelope signal power detection,” in *Medical Image Computing and Computer-Assisted Intervention—MICCAI 2014*. Springer, 2014, pp. 356–363.
- [30] “How great is the burden of musculoskeletal disease?” <http://www.aaos.org/news/aaosnow/jan08/youraaos15.asp>, accessed: 2015-05-15.
- [31] K. Lefaivre, A. Starr, B. Barker, S. Overturf, and C. Reinert, “Early experience with reduction of displaced disruption of the pelvic ring using a pelvic

- reduction frame,” *Journal of Bone & Joint Surgery, British Volume*, vol. 91, no. 9, pp. 1201–1207, 2009.
- [32] L. P. Nolte and T. Beutler, “Basic principles of CAOS,” *Injury*, vol. 35, no. 1, pp. 6–16, 2004.
- [33] I. Hacihaliloglu, A. Brounstein, P. Guy, A. Hodgson, and R. Abugharbieh, “3D ultrasound-CT registration in orthopaedic trauma using GMM registration with optimized particle simulation-based data reduction,” in *Medical Image Computing and Computer-Assisted Intervention–MICCAI 2012*. Springer, 2012, pp. 82–89.
- [34] R. A. Novelline and L. F. Squire, *Squire’s fundamentals of radiology*. La Editorial, UPR, 2004.
- [35] G. T. Herman, *Fundamentals of computerized tomography: image reconstruction from projections*. Springer Science & Business Media, 2009.
- [36] K. A. Buckwalter, J. Rydberg, K. K. Kopecky, K. Crow, and E. L. Yang, “Musculoskeletal imaging with multislice CT,” *American Journal of Roentgenology*, vol. 176, no. 4, pp. 979–986, 2001.
- [37] S. E. Polo and S. P. Jackson, “Dynamics of DNA damage response proteins at DNA breaks: a focus on protein modifications,” *Genes & development*, vol. 25, no. 5, pp. 409–433, 2011.
- [38] J. M. Liebmann, “Ultrasound biomicroscopy of the eye,” *Journal of Glaucoma*, vol. 4, no. 4, p. 299, 1995.
- [39] I. Edler and K. Lindström, “The history of echocardiography,” *Ultrasound in medicine & biology*, vol. 30, no. 12, pp. 1565–1644, 2004.
- [40] M. K. Hasan, M. A. Hussain, S. R. Ara, S. Y. Lee, and S. K. Alam, “Using nearest neighbors for accurate estimation of ultrasonic attenuation in the spectral domain,” *Ultrasonics, Ferroelectrics, and Frequency Control, IEEE Transactions on*, vol. 60, no. 6, pp. 1098–1114, 2013.

- [41] A. Weyman, “Physical principles of ultrasound,” *Principles and practice of echocardiography*, pp. 3–25, 1994.
- [42] G. Kossoff, “Basic physics and imaging characteristics of ultrasound,” *World journal of surgery*, vol. 24, no. 2, pp. 134–142, 2000.
- [43] P. Kruizinga, F. Mastik, N. de Jong, A. F. van der Steen, and G. van Soest, “Plane-wave ultrasound beamforming using a nonuniform fast Fourier transform,” *Ultrasonics, Ferroelectrics, and Frequency Control, IEEE Transactions on*, vol. 59, no. 12, 2012.
- [44] R. S. Cobbold, *Foundations of biomedical ultrasound*. Oxford University Press on Demand, 2007.
- [45] M. A. Hussain, S. K. Alam, S. Y. Lee, and M. K. Hasan, “Robust strain-estimation algorithm using combined radiofrequency and envelope cross-correlation with diffusion filtering,” *Ultrasonic Imaging*, vol. 34, no. 2, pp. 93–109, 2012.
- [46] M. D. Kraus, G. Krischak, P. Keppler, F. T. Gebhard, and U. H. Schuetz, “Can computer-assisted surgery reduce the effective dose for spinal fusion and sacroiliac screw insertion?” *Clinical Orthopaedics and Related Research®*, vol. 468, no. 9, pp. 2419–2429, 2010.
- [47] U. Stöckle, B. König, A. Schäffler, T. Zschoernack, and N. Haas, “Clinical experience with the siremobil Iso-C (3D) imaging system in pelvic surgery,” *Der Unfallchirurg*, vol. 109, no. 1, pp. 30–40, 2006.
- [48] U. Linsenmaier, C. Rock, E. Euler, S. Wirth, R. Brandl, D. Kotsianos, W. Mutschler, and K. J. Pfeifer, “Three-dimensional CT with a modified C-arm image intensifier: feasibility 1,” *Radiology*, vol. 224, no. 1, pp. 286–292, 2002.
- [49] L. Nolte, H. Walti, H. Fujita, G. Zheng, W. Seissler, and J. Hey, “A novel mobile C-arm system for use in image-guided surgery: A feasibility study,” in *Proc of the International Conference on Computer Assisted Orthopaedic Surgery*, 2002.

- [50] J. S. Hott, V. R. Deshmukh, J. D. Klopfenstein, V. K. Sonntag, C. A. Dickman, R. F. Spetzler, and S. M. Papadopoulos, "Intraoperative Iso-C C-arm navigation in craniospinal surgery: the first 60 cases," *Neurosurgery*, vol. 54, no. 5, pp. 1131–1137, 2004.
- [51] I. D. Gelalis, N. K. Paschos, E. E. Pakos, A. N. Politis, C. M. Arnaoutoglou, A. C. Karageorgos, A. Ploumis, and T. A. Xenakis, "Accuracy of pedicle screw placement: a systematic review of prospective in vivo studies comparing free hand, fluoroscopy guidance and navigation techniques," *European Spine Journal*, vol. 21, no. 2, pp. 247–255, 2012.
- [52] L. Carrat, J. Tonetti, P. Merloz, and J. Troccaza, "Percutaneous computer assisted iliosacral screwing: clinical validation," in *Medical Image Computing and Computer-Assisted Intervention–MICCAI 2000*. Springer, 2000, pp. 1229–1237.
- [53] B. Brendel, S. Winter, A. Rick, M. Stockheim, and H. Ermert, "Registration of 3D CT and ultrasound datasets of the spine using bone structures," *Computer Aided Surgery*, vol. 7, no. 3, pp. 146–155, 2002.
- [54] D. V. Amin, T. Kanade, A. M. Digioia, and B. Jaramaz, "Ultrasound registration of the bone surface for surgical navigation," *Computer Aided Surgery*, vol. 8, no. 1, pp. 1–16, 2003.
- [55] T. K. Chen, P. Abolmaesumi, D. R. Pichora, and R. E. Ellis, "A system for ultrasound-guided computer-assisted orthopaedic surgery," *Computer Aided Surgery*, vol. 10, no. 5-6, pp. 281–292, 2005.
- [56] I. Hacıhaliloglu, R. Abugharbieh, A. Hodgson, and R. Rohling, "Bone segmentation and fracture detection in ultrasound using 3D local phase features," in *Medical Image Computing and Computer-Assisted Intervention–MICCAI 2008*. Springer, 2008, pp. 287–295.
- [57] I. Hacıhaliloglu, R. Abugharbieh, A. J. Hodgson, and R. N. Rohling, "Automatic adaptive parameterization in local phase feature-based bone segmentation in ultrasound," *Ultrasound in medicine & biology*, vol. 37, no. 10, pp. 1689–1703, 2011.

- [58] A. Brounstein, I. Hacihaliloglu, P. Guy, A. Hodgson, and R. Abugharbieh, "Towards real-time 3D US to CT bone image registration using phase and curvature feature based GMM matching," in *Medical Image Computing and Computer-Assisted Intervention–MICCAI 2011*. Springer, 2011, pp. 235–242.
- [59] I. Hacihaliloglu, P. Guy, A. J. Hodgson, and R. Abugharbieh, "Volume-specific parameter optimization of 3D local phase features for improved extraction of bone surfaces in ultrasound," *The International Journal of Medical Robotics and Computer Assisted Surgery*, vol. 10, no. 4, pp. 461–473, 2014.
- [60] J. Tonetti, L. Carrat, S. Blendea, P. Merloz, J. Troccaz, S. Lavallée, and J.-P. Chirossel, "Clinical results of percutaneous pelvic surgery: Computer assisted surgery using ultrasound compared to standard fluoroscopy," *Computer Aided Surgery*, vol. 6, no. 4, pp. 204–211, 2001.
- [61] D. C. Barratt, G. P. Penney, C. S. Chan, M. Slomczykowski, T. J. Carter, P. J. Edwards, and D. J. Hawkes, "Self-calibrating 3D-ultrasound-based bone registration for minimally invasive orthopedic surgery," *Medical Imaging, IEEE Transactions on*, vol. 25, no. 3, pp. 312–323, 2006.
- [62] M. Beek, P. Abolmaesumi, S. Luenam, R. W. Sellens, and D. R. Pichora, "Ultrasound-guided percutaneous scaphoid pinning: Operator variability and comparison with traditional fluoroscopic procedure," in *Medical Image Computing and Computer-Assisted Intervention–MICCAI 2006*. Springer, 2006, pp. 536–543.
- [63] M. Beek, P. Abolmaesumi, S. Luenam, R. E. Ellis, R. W. Sellens, and D. R. Pichora, "Validation of a new surgical procedure for percutaneous scaphoid fixation using intra-operative ultrasound," *Medical image analysis*, vol. 12, no. 2, pp. 152–162, 2008.
- [64] J. A. Noble and D. Boukerroui, "Ultrasound image segmentation: a survey," *Medical Imaging, IEEE Transactions on*, vol. 25, no. 8, pp. 987–1010, 2006.

- [65] V. Daanen, J. Tonetti, and J. Troccaz, “A fully automated method for the delineation of osseous interface in ultrasound images,” in *Medical Image Computing and Computer-Assisted Intervention–MICCAI 2004*. Springer, 2004, pp. 549–557.
- [66] J. Kowal, C. Amstutz, F. Langlotz, H. Talib, and M. G. Ballester, “Automated bone contour detection in ultrasound B-mode images for minimally invasive registration in computer-assisted surgery An in vitro evaluation,” *The International Journal of Medical Robotics and Computer Assisted Surgery*, vol. 3, no. 4, pp. 341–348, 2007.
- [67] A. Kryvanos, “Computer assisted surgery for fracture reduction and deformity correction of the pelvis and long bones,” 2003.
- [68] P. Foroughi, E. Boctor, M. J. Swartz, R. H. Taylor, and G. Fichtinger, “Ultrasound bone segmentation using dynamic programming,” in *Ultrasonics Symposium, 2007. IEEE*. IEEE, 2007, pp. 2523–2526.
- [69] K. A. Patwardhan, K. Cao, D. Mills, and R. Thiele, “Automated bone and joint-region segmentation in volumetric ultrasound,” in *Biomedical Imaging (ISBI), 2012 9th IEEE International Symposium on*. IEEE, 2012, pp. 1327–1330.
- [70] A. K. Jain and R. H. Taylor, “Understanding bone responses in B-mode ultrasound images and automatic bone surface extraction using a bayesian probabilistic framework,” in *Medical Imaging 2004*. International Society for Optics and Photonics, 2004, pp. 131–142.
- [71] P. He and J. Zheng, “Segmentation of tibia bone in ultrasound images using active shape models,” in *Engineering in Medicine and Biology Society, 2001. Proceedings of the 23rd Annual International Conference of the IEEE*, vol. 3. IEEE, 2001, pp. 2712–2715.
- [72] A. Alfiansyah, R. Streichenberger, P. Kilian, M. Bellemare, and O. Coulon, “Automatic segmentation of hip bone surface in ultrasound images using an active contour,” *International Journal of Computer Assisted Radiology and Surgery*, vol. 1, p. 496, 2006.

- [73] I. Hacihaliloglu, R. Abugharbieh, A. J. Hodgson, and P. Guy, “Automatic bone bontour detection in 3D B-mode ultrasound images using optimized phase symmetry features - A clinical evaluation evaluation for pelvic fracture,” *Journal of Bone & Joint Surgery, British Volume*, vol. 94, no. SUPP XLIV, pp. 64–64, 2012.
- [74] B. Brendel, S. Winter, A. Rick, M. Stockheim, and H. Ermert, “Bone registration with 3D CT and ultrasound data sets,” in *International Congress Series*, vol. 1256. Elsevier, 2003, pp. 426–432.
- [75] G. Ionescu, S. Lavallée, and J. Demongeot, “Automated registration of ultrasound with CT images: Application to computer assisted prostate radiotherapy and orthopedics,” in *Medical Image Computing and Computer-Assisted Intervention–MICCAI99*. Springer, 1999, pp. 768–777.
- [76] I. Hacihaliloglu, R. Abugharbieh, A. J. Hodgson, and R. N. Rohling, “Enhancement of bone surface visualization from 3D ultrasound based on local phase information,” in *Ultrasonics Symposium, 2006. IEEE*. IEEE, 2006, pp. 21–24.
- [77] I. Hacihaliloglu, R. Abugharbieh, A. Hodgson, and R. Rohling, “Automatic data-driven parameterization for phase-based bone localization in US using log-gabor filters,” in *Advances in Visual Computing*. Springer, 2009, pp. 944–954.
- [78] P. Kovesi, “Image features from phase congruency,” *Videre: Journal of computer vision research*, vol. 1, no. 3, pp. 1–26, 1999.
- [79] A. Amir-Khalili, R. Abugharbieh, and A. J. Hodgson, “Using graphics processing units to achieve real-time bone surface extraction from volumetric medical ultrasound image data using local phase features,” in *Computer Assisted Orthopaedic Surgery (CAOS)*, 2013, conference. [Online]. Available: <http://bisicl.ece.ubc.ca/papers/CAOS2013.pdf>
- [80] T. Varghese, J. Ophir, E. Konofagou, F. Kallel, and R. Righetti, “Tradeoffs in elastographic imaging,” *Ultrasonic Imaging*, vol. 23, no. 4, pp. 216–248, 2001.

- [81] G. M. Treece, J. E. Lindop, A. H. Gee, and R. W. Prager, “Freehand ultrasound elastography with a 3D probe,” *Ultrasound in medicine & biology*, vol. 34, no. 3, pp. 463–474, 2008.
- [82] H. Rivaz, E. M. Boctor, M. A. Choti, and G. D. Hager, “Real-time regularized ultrasound elastography,” *Medical Imaging, IEEE Transactions on*, vol. 30, no. 4, pp. 928–945, 2011.
- [83] M. A. Hussain, E. M. Abu Anas, S. K. Alam, S. Y. Lee, and M. K. Hasan, “Direct and gradient-based average strain estimation by using weighted nearest neighbor cross-correlation peaks,” *Ultrasonics, Ferroelectrics, and Frequency Control, IEEE Transactions on*, vol. 59, no. 8, pp. 1713–1728, 2012.
- [84] J. P. Spalazzi, J. Gallina, S. D. Fung-Kee-Fung, E. E. Konofagou, and H. H. Lu, “Elastographic imaging of strain distribution in the anterior cruciate ligament and at the ligament-bone insertions,” *Journal of orthopaedic research*, vol. 24, no. 10, pp. 2001–2010, 2006.
- [85] H. Rivaz, E. Boctor, P. Foroughi, R. Zellars, G. Fichtinger, and G. Hager, “Ultrasound elastography: a dynamic programming approach,” *Medical Imaging, IEEE Transactions on*, vol. 27, no. 10, pp. 1373–1377, 2008.
- [86] W. Boonleelakul, U. Techavipoo, D. Worasawate, R. Keinprasit, P. Pinunsottikul, N. Sugino, and P. Thajchayapong, “Compression of ultrasound RF data using quantization and decimation,” in *Biomedical Engineering International Conference (BMEiCON), 2013 6th*. IEEE, 2013, pp. 1–4.
- [87] J. A. Jensen, “Field: A program for simulating ultrasound systems,” in *10th Nordicbaltic conference on Biomedical Imaging, PART 1*, vol. 4. Citeseer, 1996, pp. 351–353.
- [88] W. Pistoia, B. Van Rietbergen, E.-M. Lochmüller, C. Lill, F. Eckstein, and P. Rüeggsegger, “Estimation of distal radius failure load with micro-finite element analysis models based on three-dimensional peripheral quantitative computed tomography images,” *Bone*, vol. 30, no. 6, pp. 842–848, 2002.



- [89] R. Zahiri-Azar and S. E. Salcudean, "Motion estimation in ultrasound images using time domain cross correlation with prior estimates," *Biomedical Engineering, IEEE Transactions on*, vol. 53, no. 10, pp. 1990–2000, 2006.
- [90] R. Nass, L. S. Farhy, J. Liu, S. S. Pezzoli, M. L. Johnson, B. D. Gaylinn, and M. O. Thorner, "Age-dependent decline in acyl-ghrelin concentrations and reduced association of acyl-ghrelin and growth hormone in healthy older adults," *The Journal of Clinical Endocrinology & Metabolism*, vol. 99, no. 2, pp. 602–608, 2013.
- [91] F. Kallel and J. Ophir, "A least-squares strain estimator for elastography," *Ultrasonic imaging*, vol. 19, no. 3, pp. 195–208, 1997.
- [92] H. G. Sung, "Gaussian mixture regression and classification," Ph.D. dissertation, Rice University, 2004.
- [93] L. Zelnik-Manor and P. Perona, "Self-tuning spectral clustering," in *Advances in neural information processing systems*, 2004, pp. 1601–1608.
- [94] D. A. Cohn, Z. Ghahramani, and M. I. Jordan, "Active learning with statistical models," *Journal of artificial intelligence research*, 1996.
- [95] I. Hacihaliloglu, P. Guy, A. J. Hodgson, and R. Abugharbieh, "Automatic extraction of bone surfaces from 3D ultrasound images in orthopaedic trauma cases," *International Journal of Computer Assisted Radiology and Surgery (IJCARS)*, 2015.

## **Appendix A**

### **Clinical Evaluation Protocol Form**

## **Bone Boundary Localization in Ultrasound Images Using Combined Ultrasound Elastography and Envelope Signal Power Detection**

**Principal Investigator:** Dr. Rafeef Abugharbieh,  
Associate Professor  
Department of Electrical and Computer Engineering  
University of British Columbia, Vancouver  
Ph: [REDACTED]  
Fax: [REDACTED]  
Email: [REDACTED]

**Co-Investigator:** Dr. Antony J. Hodgson,  
Professor  
Department of Mechanical Engineering  
University of British Columbia, Vancouver  
Ph: [REDACTED]  
Fax: [REDACTED]  
Email: [REDACTED]

**Co-Investigator:** Mohammad Arafat Hussain, MSc, Candidate  
Biomedical Engineering Program  
Department of Electrical and Computer Engineering  
University of British Columbia, Vancouver  
Ph: [REDACTED]  
Email: [REDACTED]

### **Study Protocol**

#### **1. Background**

In computer assisted orthopedic surgery (CAOS), fluoroscopy remains the primary intraoperative imaging modality for bone boundary visualization. However, the use of fluoroscopy leads to radiation exposure to surgical teams and patients [1]. It is also difficult to extract positions and shapes of bones from fluoroscopic images since it renders a 2-dimensional (2D) projection plane of a part of human body. Consequently, researches gave rise to recent interest in safer non-ionizing real-time intraoperative imaging alternatives [2]. As a potential alternative, relatively cheap and widely available medical-ultrasound (US) is recently showing great promise as an intraoperative surgical tool guide for safer orthopedic surgery system [3]-[14].

In CAOS, US bone segmentation is necessary to collect sample points on bone surface [4] or to visualize full bone surface in 3D [5] that to be registered to images of other imaging modalities (e.g., pre-operative computed tomography (CT)). Most of the US image segmentation algorithms

have been developed so far use the log-compressed envelop of the US radio-frequency (RF) data (i.e., B-mode data). In the past, US segmentation for bone localization is usually carried out manually or semi-automatically [6], [7]. Since manual and semi-automatic segmentations are extremely time consuming, a real time application of these methods are impossible. Several attempts to automate US image segmentation have been proposed in the literature [8]-[20]. Some automatic methods are based on image intensity and local gradient [8], [9], but have limitations of unpredictable results and high parameter sensitivity. To address these issues, some methods incorporate a priori bone appearance information into the segmentation framework in terms of active shape model that combine shape models along with the intensity and gradient information [8], [10], [11]. Other methods use dynamic programming [12] or morphological features [6] to delineate bone boundary in the traditional B-mode images. However, these intensity and gradient information-based methods face significant difficulties in the interpretation of US images due to high level of speckle noise, reverberation, anisotropy, signal dropout, and beam direction [1], [10]. Recent works by Hacıhaliloglu et al. [15]-[20] on local image phase feature-based bone segmentation address some of these limitations however remains prone to false positive bone responses at soft tissue interfaces that commonly exhibit similar intensity profiles as bone interfaces.

US-based elastography is an emerging medical diagnostic tool for capturing the mechanical properties (e.g. stiffness) of biological tissue [21]-[23]. Elastography has shown promise in the detection of breast and prostate tumors, liver cirrhosis, vascular plaques [22], and ligament-bone insertion. However, in the bone imaging literature, US elastography has been very limited. In [23], bone detection using US elastography was investigated. The reported strain images, however, showed low contrast between the hard bone and soft tissue regions. In addition, problems arose from signal windowing as window-based elastography (WBE) methods have limitations associated with the size of the window segments. A significant amount of noise in the strain image can be introduced with the choice of smaller window size and/or large overlap between successive windows [21]. Furthermore, WBE methods often produce distorted strain estimates due to the amplitude modulation effect even if there is no displacement estimation error [23].

## 2. Purpose

The purpose of this research proposal is to determine the effectiveness and demonstrate the clinical feasibility of using the US elastography in conjugation with the US envelope for computing bone boundary in the intraoperative orthopedic surgery environment. Our group is on the leading edge of work in this field, but our current state-of-the-art ultrasound analysis techniques [15]-[20] still produce a non-trivial number of false positive responses. Since elastography estimates tissue stiffness, we expect our new method will achieve a marked reduction of false positive bone responses at the soft tissue interfaces. Using a better algorithm of US elastography [24] that eliminates the previously reported errors associated with the WBE methods, and using the envelope power that has higher dynamic range than that of log-compressed envelope, we would ultimately aim to detect bone in US images more robustly and decrease the radiation exposure to patients and surgical teams.

### 3. Hypothesis

In the proposed dissertation work, we plan to do a feasibility study of a novel method for robust bone boundary localization based on combined US strain imaging and envelope power signal detection. Our method uses real-time strain imaging based on analytic minimization of regularized cost functions [24]. To better delineate the bone boundary, we combine the envelope power map with the strain image. We use the envelope power map rather than an envelope or log-compressed envelope map (i.e., B-mode) as it possesses a higher dynamic range. To ensure robustness and self-tuning capability of our proposed methodology, we come up with an idea of automatic weight selection process based on echo de-correlation measure between the pre- and post-compression RF frames; the weight is to be used to fuse the strain and envelope power map. We also come up with an idea of data driven bone discontinuity detection scheme if there is any bone fracture. In addition, we plan to use Gaussian mixture regression (GMR) over the bone indicating maximum intensity points. GMR is a more flexible multivariate nonparametric regression model that better preserves the curvature features in the bone boundary than a linear regression model typically used in data regularization.

### 4. Statistical Analysis

The performance of the proposed algorithm will be evaluated qualitatively and quantitatively using the finite-element-model (FEM) phantoms, artificial physical phantom as well as *in vivo* data, and will be compared with the state-of-the-art bone boundary estimation algorithms [15]-[20]. We will calculate the mean absolute error (MAE) between the estimated (by the proposed and state-of-the-art methods) and ground truth bone contours. We will extract ground truth bone contours (i) from the defined bone geometry in simulation for the FEM phantoms, (ii) from the CT images for the experimental phantom, and (iii) from the expert delineated bone boundaries on the B-mode images for the *in vivo* data. We will perform Student's *t*-test between the MAE produced by the proposed and state-of-the-art methods. Our ultimate aim is to achieve a significant reduction ( $p < 0.05$ ) of the MAE for the proposed algorithm with respect to that of the state-of-the-art methods.

### 5. Study Population

We will select up to 25 volunteer participants in our study who will be scanned with medical-grade ultrasound scanner. Different aspects related to the study participation are discussed below.

#### 5.1. Participant Inclusion Criteria

The criteria for selecting a participant for our study are:

1. Healthy Male/Female,
2. Aged more than 19 years,
3. Willing to come at the Centre for Hip Health and Mobility (CHHM), Vancouver, to be scanned with medical ultrasound, and
4. Have good competence in English to read and understand the contents of the consent form.

We do not have any plan to arrange any translator for participants. Therefore, a participant having English as a second language (ESL) must have a good command over English. If any participant feels uncomfortable understanding the wording of the consent form properly, he/she will be requested not to participate in the study.

### **5.2. Participant Exclusion Criteria**

Participant exclusion criteria are:

1. Participant with skin conditions or allergy which precludes the use of ultrasound gel, and
2. Participants unable/reluctant to provide informed consent.

### **5.3. Justifications**

To evaluate the effectiveness as well as robustness of our proposed research study, a collection of ultrasound data from 25 participants would be sufficient since enough variability in tissue properties would be present among those data. We will also select participants who are at least 19 years old since people with this age can be considered independent and intelligent enough to justify their willingness to participate in our study.

### **5.4. Time Required for Scanning**

We will perform scanning over the radius, the ulna, the humerus, the upper sternum, the iliac crest, and the tibia bones. A scan in each anatomical position will take approximately 5-15 seconds, though multiple scans may need to be acquired (i.e., for a single data-set) to ensure an optimal viewing angle. The time per anatomy-scan (one data-set) will be limited to 3 minutes. In total, we anticipate acquiring approximately 15 data-sets per participant. Allowing time for re-positioning between anatomical sites, the entire scanning period will likely take 30-45 minutes. Including time for the consent procedure, participants should allow approximately 1 hour for their visit to the lab.

### **5.5. Privacy During Scanning**

Since we will perform scanning over the radius, the ulna, the humerus, the upper sternum, the iliac crest, and the tibia bones, a participant will not need to disrobe but slightly removing clothing over the above stated anatomical regions. Also to note that during the scanning of the iliac crest, a participant will be asked to slightly lower their clothing from the waist line (i.e., the waist area where a belt is usually worn). However, he/she will not need to disrobe since iliac crest is easily accessible from the waist line. The principal investigator, Prof. Rafeef Abugharbieh would be present during the scanning of a female participant, so that the participant is ensured with full privacy and comfort. In addition, a female participant will have the option of being scanned by Prof. Rafeef Abugharbieh in private.

## **6. Ultrasound Procedure**

After obtaining the informed consent, a participant will be scanned using a standard medical-grade US machine. The ultrasound scanner we are going to use is Sonix RP (Ultrasonix Medical Corporation, Richmond, BC) which is integrated with an ultrasound probe operates between 5-14MHz. Due to the physics of ultrasound imaging, RF signals cannot penetrate the bone surface. Therefore, we need to place the ultrasound probe over the skin surface in a way so that the transducer face becomes approximately parallel or partially inclined to the bone surface.

Before starting the ultrasound scan, a special ultrasound gel (the amount equivalent to the tip of a thumb) will be spread onto the skin surface. The gel makes the probe movement much easier and effective. It also helps coupling the probe interface with the skin surface which makes the image



quality much better. The gel has no perfumes, no color, is hypoallergenic and is water-soluble. During the scanning no pain will be caused to the participant.

We will obtain scans from several sites on the arm, pelvis and leg (typical sites of fractures in orthopaedic trauma). More specifically, we anticipate obtaining scans from the radius, the ulna, the humerus, the upper sternum, the iliac crest, the proximal and distal femur and the tibia. To obtain each data-set, we will position the participant so as to be able to apply the probe to the relevant portion of the anatomy.

## 7. Recruitment Process

To recruit potential participants in our study, we will post an invitation flyer on physical and electronic notice boards in the Faculty of Applied Science at UBC and, with permission, on designated public notice boards at Vancouver General Hospital and within the various Vancouver Coastal Health Research Institutes. Potential participants will be invited to respond by email or telephone in order to arrange the details of participating in the study. Details relevant to the study (such as date, and time of the data collection) will be arranged by direct contact (either by email or telephone) by the principal investigator (PI) or co-investigators.

Once a participant fixes an appointment with us, we shall send the consent form to him/her in advance so that he/she can discuss about participation with his/her friends and family. We shall also discuss in person at CHHM once the participant arrives. Participants would have time as long as they wish to decide to participate in the study, and the data acquisition will begin immediately after the consent is given. We shall offer a 10CAD gift card to each participant (e.g., for Starbucks or similar) to offset his/her inconvenience.

## 8. References

- [1] B. Brendel, S. Winter, A. Rick, M. Stockheim, and H. Ermet, "Registration of 3D CT and Ultrasound Datasets of the Spine Using Bone Structures," *Journal of Computer Aided Surgery*, vol. 7, no. 3, pp. 146–155, 2002.
- [2] D. V. Amin, T. Kanade, A. M. Digioia, and B. Jaramaz, "Ultrasound Registration of the Bone Surface for Surgical Navigation," *Journal of Computer Aided Surgery*, vol. 8, no. 1, pp. 1–16, 2003.
- [3] C. X. Yan, B. Goulet, J. Pelletier, S. J. S. Chen, D. Tampieri, and D. L. Collins, "Towards Accurate, Robust and Practical Ultrasound-CT Registration of Vertebrae for Image-guided Spine Surgery," *International Journal of Computer Assisted Radiology and Surgery*, vol. 6, no. 4, pp. 523–537, 2011.
- [4] T. K. Chen, P. Abolmaesumi, D. R. Pichora, and R. E. Ellis, "A System for Ultrasound-guided Computer Assisted Orthopaedic Surgery," *Journal of Computer Aided Surgery*, vol. 10, no. 5–6, pp. 281–292, 2005.
- [5] M. Beek, P. Abolmaesumi, S. Luenam, R. Sellens, and D. Pichora, "Ultrasound-guided Percutaneous Scaphoid Pinning: Operator Variability and Comparison with Traditional Fluoroscopic Procedure," In: *Medical Image Computing and Computer Assisted Intervention—MICCAI 2006*, pp. 536–543, 2006.
- [6] Y. Zhang, R. N. Rohling, and D. K. Pai, "Direct Surface Extraction from 3D Freehand Ultrasound Images," In: *IEEE Visualization*, pp. 45–52, 2002.
- [7] J. Tonetti, L. Carrat, S. Blendea, P. Merloz, J. Troccaz, S. Lavalée, and J. P. Chirossel,

- "Clinical Results of Percutaneous Pelvic Surgery: Computer Assisted Surgery Using Ultrasound Compared to Standard Fluoroscopy," *Journal of Computer Aided Surgery*, vol. 6, no. 4, pp. 204–211, 2001.
- [8] D. C. Barratt, P. G. Penney, S. K. Chan, M. Slomczykowski, T. J. Carter, P. J. Edwards PJ, and D. J. Hawkes, "Self Calibrating 3D-Ultrasound based Bone Registration for Minimally Invasive Orthopaedic Surgery," *IEEE Transaction on Medical Imaging*, vol. 25, no. 3, pp. 312–323, 2006.
  - [9] V. Daanen, J. Tonetti, and J. Troccaz, "A Fully Automated Method for the Delineation of Osseous Interface in Ultrasound Images," In: *Medical Image Computing and Computer Assisted Intervention–MICCAI 2004*, pp. 549–557, 2004.
  - [10] J. Kowal, C. Amstutz, F. Langlotz, H. Talib, and M. G. Ballester, "Automated Bone Contour Detection in Ultrasound B-mode Images for Minimally Invasive Registration in Computer Assisted Surgery an In Vitro Evaluation," *International Journal of Medical Robotics and Computer Assisted Surgery*, vol. 3, no. 4, pp. 341–348, 2007.
  - [11] A. K. Jain and R. H. Taylor, "Understanding Bone Responses in B-mode Ultrasound Images and Automatic Bone Surface Extraction Using a Bayesian Probabilistic Framework," In: *Proc. SPIE Medical Imaging*, vol. 5373, pp. 131–142, 2004.
  - [12] A. Alfiansyah, R. Streichenberger, M. E. Bellemare, and O. Coulon, "Automatic Segmentation of Hip Bone Surface in Ultrasound Images Using an Active Contour," *International Journal of Computer Assisted Radiology and Surgery*, vol. 1, pp. 496, 2006.
  - [14] P. Foroughi, E. Boctor, M. J. Swartz, R. H. Taylor, and G. Fichtinger, "Ultrasound Bone Segmentation Using Dynamic Programming," In: *IEEE Ultrasonics Symposium*, vol. 1051, pp. 2523–2526, 2007.
  - [15] I. Hacıhaliloglu, R. Abugharbieh, A. J. Hodgson, R. N. Rohling, P. O'Brien, and P. Guy, "Surgical Tool Localization From 3D Ultrasound Volumes Using 3D Phase-based Features," In: *Proceedings of the 8th Annual Meeting of CAOS International*, Hong Kong-China, 2008.
  - [16] I. Hacıhaliloglu, R. Abugharbieh, A. J. Hodgson, R. N. Rohling, P. O'Brien, and P. Guy, "Distal Radius and K-wire Localization in 3D Ultrasound Using Local Phase Information," In: *Proceedings of the 7th Annual Meeting of CAOS International*, Heidelberg-Germany, pp. 572–575, 2007.
  - [17] I. Hacıhaliloglu, R. Abugharbieh, A. J. Hodgson, R. N. Rohling, "Enhancement of Bone Surface Visualization from 3D Ultrasound Based on Local Phase Information," In: *IEEE Ultrasonics Symposium*, Vancouver-Canada, pp. 21–24, 2006.
  - [18] I. Hacıhaliloglu, P. Guy, A. J. Hodgson, R. Abugharbieh, "Volume-Specific Parameter Optimization of 3D Local Phase Features for Improved Extraction of Bone Surfaces in Ultrasound Images," *International Journal of Medical Robotics and Computer Assisted Surgery*, Jan 2014.
  - [19] I. Hacıhaliloglu, R. Abugharbieh, A. J. Hodgson, and R. N. Rohling, "Bone Segmentation and Fracture Detection in Ultrasound Using 3D Local Phase Features," In: *Medical Image Computing and Computer Assisted Intervention–MICCAI 2008*, pp. 287–295, 2008.
  - [20] I. Hacıhaliloglu, R. Abugharbieh, A. J. Hodgson, and R. N. Rohling, "Automatic Adaptive Parameterization in Local Phase Feature-based Bone Segmentation in Ultrasound," *Ultrasound in Med. and Biol.*, vol. 37, no. 10, pp. 1689–1703, 2011.
  - [21] M. A. Hussain, E. M. A. Anas, S. K. Alam, S. Y. Lee, and M. K. Hasan, "Direct and Gradient Based Average Strain Estimation by Using Weighted Nearest Neighbor Cross-



- correlation Peaks", *IEEE Transactions on Ultrasonics, Ferroelectrics, and Frequency Control*, vol. 59, no. 8, pp. 1713–1728, 2012.
- [22] M. A. Hussain, S. K. Alam, S. Y. Lee, and M. K. Hasan, "A Robust Strain Estimation Algorithm Using Combined Radio-frequency and Envelope Cross-correlation with Diffusion Filtering", *Ultrasonic Imaging*, vol. 34, pp. 93–109, 2012.
  - [23] X. Wen, S. T. Salcudean, "Enhancement of Bone Surface Visualization Using Ultrasound Radio-frequency Signals," In: *IEEE Ultrasonics Symposium*, vol. 1051, pp. 2535–2538, 2007.
  - [24] J. E. Lindop, G. M. Treece, A. H. Gee, and R. W. Prager, "Estimation of Displacement Location for Enhanced Strain Imaging," *IEEE Transactions on Ultrasonics, Ferroelectrics, and Frequency Control*, vol. 54, no. 9, pp. 1751–1771, 2007.
  - [25] H. Rivaz, E. M. Boctor, M. A. Choti, and G. D. Hager, "Real-time Regularized Ultrasound Elastography," *IEEE Transaction on Medical Imaging*, vol. 30, no. 4, pp. 928–945, 2011.

## Appendix B

### Clinical Evaluation Patient Consent Form



University of British Columbia  
Departments of Electrical and Computer Engineering, and  
Mechanical Engineering

**Bone Boundary Localization in Ultrasound Images Using Combined  
Ultrasound Elastography and Envelope Signal Power Detection**

**STUDY PARTICIPANT CONSENT FORM**

**Principal Investigator:** Dr. Rafeef Abugharbieh,  
Associate Professor  
Department of Electrical and Computer Engineering  
University of British Columbia, Vancouver  
Ph: [REDACTED]  
Fax: [REDACTED]  
Email: [REDACTED]

**Co-Investigator:** Dr. Antony J. Hodgson,  
Professor  
Department of Mechanical Engineering  
University of British Columbia, Vancouver  
Ph: [REDACTED]  
Fax: [REDACTED]  
Email: [REDACTED]

**Co-Investigator:** Mohammad Arafat Hussain, MSc, Candidate  
Biomedical Engineering Program  
Department of Electrical and Computer Engineering  
University of British Columbia, Vancouver  
Ph: [REDACTED]  
Email: [REDACTED]

**Grant Information:**

UBC Number	Title	Sponsor
03-4813	Advanced tools for computer assisted orthopaedic surgery	Natural Sciences and Engineering Research Council of Canada (NSERC)

## Description

You have been invited to participate in this study because you have shown interest in our invitation flyer and offered to contribute in this study as a participant. However, before you decide, it is important for you to understand what the research involves. This consent form will tell you about the study, why the research is being done, what will happen to you during the study and the possible benefits, risks and discomforts.

If you wish to participate, you will be asked to sign this form. If you do decide to take part in this study, you are still free to withdraw at any time and without giving any reasons for your decision.

If you do not wish to participate, you do not have to provide any reason for your decision not to participate. Please take time to read the following information carefully and to discuss it with your family and friends before you decide.

This research is currently being carried out as an internal study by the investigators listed above and is conducted by the University of British Columbia (UBC), Department of Electrical and Computer Engineering, and Department of Mechanical Engineering.

## Background

In computer assisted orthopedic (bone related) surgery, a special type of X-ray called fluoroscopy is used as the primary intraoperative (during surgery) imaging system to see bones inside the human body. However, the use of fluoroscopy increases the radiation risk to surgical teams and patients. It is also difficult to see the positions and shapes of bones from fluoroscopic images since it shows a 2-dimensional image of a part of human body, just like a photo taken by a typical point-and-shoot camera. Therefore, researchers are trying to use different imaging system which is safe (non-ionizing) and can show real-time images (like a live game on television).

As a potential alternative, relatively cheap and widely available ultrasound has recently showed great promise as an intraoperative imaging system for safer orthopedic surgery. Medical ultrasound is utilized to image soft tissues inside the body but it can also show the outline of more solid structures such as bone. Many people would be familiar with the use of ultrasound to image a baby or fetus prior to birth. In this study, we will image bone with similar ultrasound technology.

To use ultrasound in computer assisted orthopedic surgery, we need to mark out the bone outlines automatically in the ultrasound images which is very challenging. In medical science, this marking out process is called "segmentation". A number of problems associated with the ultrasound imaging system have been making this segmentation work too hard.

Ultrasound *elastography* is an emerging medical diagnostic tool to measure the stiffness of different types of human tissues like muscles, bones, etc. Elastography has shown a

great success so far in the detection of breast and prostate tumors/cancers, liver cirrhosis, etc. As we already stated that the bone segmentation in ultrasound images are very challenging, in our current research project, we are trying to use ultrasound elastography to improve the performance of bone segmentation process in ultrasound images.

### **Purpose**

The purpose of this research study is to demonstrate the clinical feasibility of using ultrasound elastography in addition to another type of ultrasound data called *radio-frequency envelope* for automatic segmentation of bone in ultrasound images during an orthopedic surgery. We aim to segment (mark out) bone in ultrasound images better and to decrease the fluoroscopy related radiation risk to patients and clinicians.

### **Who can participate?**

Any healthy Male/Female, aged more than 19 years, willing to come to the Centre for Hip Health and Mobility (CHHM), Vancouver, to be scanned with a medical ultrasound device, and have good command in English to read and understand this consent form. If English is your second language and if you feel uncomfortable understanding the wording of this consent form properly, we like to request you not to participate in this study. We are unable to arrange any translator for you.

### **Who should not participate?**

Volunteers who have a skin condition or allergy which precludes the use of ultrasound gel over the skin surface, and/or unable/reluctant to provide informed consent should also not participate.

### **Study Procedure**

The study will take place in the Centre for Hip Health and Mobility, Vancouver, BC, Canada. Enrollment in this preliminary study will be limited to 25 participants who have given their consent.

The components of the proposed research involve a medical ultrasound scanner and an ultrasound probe. Before scanning the area on your body (exposed skin surface) an ultrasound gel will be spread onto the skin surface. The gel makes the probe movement much easier and effective, and also improves the image quality. The gel has no perfumes, no color, is hypoallergenic and is water-soluble.

The ultrasound probe will then be placed on the skin over the targeted bone to be scanned for about 15 seconds each (total scanning time for each anatomical place is 3 minutes). As a whole, you will need to stay in CHHM to be scanned for approximately 1 hour.

After the collection of data, we shall use our official portable hard disk to carry these data to the Department of Electrical and Computer Engineering (ECE), UBC, and put these in

secured ECE network drive which is password protected. Then the data in the portable hard drive will be erased immediately. Only designated people related to this research shall have access to this data. This consent form will be kept locked in our office and NO data will be made public or posted on the Web.

According to UBC Policy #85 on Scholarly Integrity, these data will be retained for at least 5 years within our research office. After that if required, these data will be erased from the ECE network drive.

### **Risks**

As this study does not influence treatment and uses technology which is commonly used in other fields of medicine we foresee no additional risks from participating in this study.

### **Cost and Payments**

You will incur no additional cost for participation in this study. Your participation is purely voluntary. However, we offer a 10CAD Starbucks gift card to you to offset your inconvenience.

### **Benefits**

There are no direct benefits to you for participating of this study. We hope that the information learned from this study will help in developing ultrasound imaging as a safer alternative for tool guidance in minimally invasive computer assisted orthopedic surgery system.

### **Discomforts**

As described, Ultrasound imaging involves the placement of a gel over the area to scan followed by the sliding and gentle compression of the probe on the gel and skin surface to visualize the area of interest. This procedure involves a very small amount of pressure over your skin surface. As ultrasound is often successfully used over affected tender areas of the body (for example to identify a fluid collection in a swollen area or on the infected skin overlying an abscess) we expect this test to be well tolerated.

You may request to have the procedure stopped at any time for discomfort or any other reason.

### **Privacy**

During the time of scanning the iliac crest, you will be asked to slightly lower your clothing from the waist line (i.e., the waist area where a belt is usually worn). However, you do not need to disrobe your clothing since iliac crest is easily accessible from the waist line. If you are a female, then the principal investigator of this study Prof. Rafeef Abugharbieh will be present during the scanning so that she can ensure your full privacy and comfort. In addition, you can take the opportunity of to be scanned by her in private.



### **Confidentiality**

Your confidentiality will be respected. However, research records and health or other source records identifying you may be inspected in the presence of the Principal Investigator or her designate by representatives of the Health Canada, and UBC Clinical Research Ethics Board for the purpose of monitoring the research. No information or records that disclose your identity will be published without your consent, nor will any information or records that disclose your identity be removed or released without your consent unless required by law.

You will be assigned a unique study number as a participant in this study. This number will not include any personal information that could identify you (e.g., it will not include your Personal Health Number, SIN, or your initials, etc.). Only this number will be used on any research-related information collected about you during the course of this study, so that your identity will be kept confidential. Information that contains your identity will remain only with the Principal Investigator and/or designate. The list that matches your name to the unique study number that is used on your research-related information will not be removed or released without your consent unless required by law.

Your rights to privacy are legally protected by federal and provincial laws that require safeguards to insure that your privacy is respected. You also have the legal right of access to the information about you that might be provided to the granting agency and, if need be, an opportunity to correct any errors in this information. Further details about these laws are available on request to your study doctor.

Your date of birth (month/year) will also be provided if requested by the granting agency or responsible regulatory agency.

### **Withdrawal**

You may withdraw from this study at any time without giving reasons. If you choose to enter the study and then decide to withdraw at a later time, you have the right to request the withdrawal of your information collected during the study. This request will be respected to the extent possible. Please note however that there may be exceptions where the data will not be able to be withdrawn for example where the data is no longer identifiable (meaning it cannot be linked in any way back to your identity) or where the data has been merged with other data. If you would like to request the withdrawal of your data, please let anyone of the investigators know.

### **What happens if something goes wrong?**

As we already mentioned that we foresee no additional risks from participating in this study however by signing this form, you do not give up any of your legal rights and you do not release the investigators, participating institutions, or anyone else from their legal and professional duties. If you become ill or physically injured as a result of participation in this study, medical treatment will be provided at no additional cost to you. The costs of

your medical treatment will be paid by your provincial medical plan and/or by the study granting agency, *natural sciences and engineering research council of Canada (NSERC)*.

In case of a serious medical event, please report to an emergency room and inform them that you are participating in a clinical study and that the following person can then be contacted for further information: Dr. Rafeef Abugharbieh at telephone number: [REDACTED]  
[REDACTED]

**Who do I contact if I have any questions or concerns about my rights as a participant?**

If you have any concerns or complaints about your rights as a research participant and/or your experiences while participating in this study, contact the Research Participant Complaint Line in the University of British Columbia Office of Research Ethics by e-mail at [REDACTED] or by phone at [REDACTED] (Toll Free: [REDACTED]).

**Contact**

If you have any questions about the procedures employed in this study, if you desire further information with respect to this study, or if you experience any adverse effects you should contact Dr. Rafeef Abugharbieh at [REDACTED] or Dr. Antony J. Hodgson at [REDACTED].

**Summary**

The proposed procedure requires your consent to proceed with ultrasound imaging of some easily approachable exposed skin surface over bones.



### Participant Consent

My signature on this consent form means:

- I have read and understood the information in this consent form.
- I have had enough time to think about the information provided.
- I have been able to ask for advice if needed.
- I have been able to ask questions and have had satisfactory responses to my questions.
- I understand that all of the information collected will be kept confidential and that the results will only be used for scientific purposes.
- I understand that my participation in this study is voluntary.
- I understand that I am completely free at any time to refuse to participate or to withdraw from this study at any time, and that this will not change the quality of care that I receive.
- I authorize access to my health records (i.e., date of birth) as described in this consent form.
- I understand that I am not waiving any of my legal rights as a result of signing this consent form.
- I understand that there is no guarantee that this study will provide any benefits to me.

I will receive a signed copy of this consent form for my own records.

I consent to participate in this study.

\_\_\_\_\_  
Participant's Signature

\_\_\_\_\_  
Printed Name

\_\_\_\_\_  
Date

\_\_\_\_\_  
Signature of Person  
Obtaining Consent

\_\_\_\_\_  
Printed Name

\_\_\_\_\_  
Study Role

\_\_\_\_\_  
Date

\_\_\_\_\_  
Investigator Signature

\_\_\_\_\_  
Printed Name

\_\_\_\_\_  
Date

My signature above signifies that the study has been reviewed with the study participant by me and/or by my delegated staff. My signature may have been added at a later date, as I may not have been present at the time the participant's signature was obtained.